DEVELOPMENT OF FLEXIBLE ELECTROMECHANICAL SENSORS FOR HUMAN MOTION MONITORING AND HUMAN MACHINE INTERFACE

MUJEEB YOUSUF



CENTRE FOR APPLIED RESEARCH IN ELECTRONICS

INDIAN INSTITUTE OF TECHNOLOGY DELHI

March 2026

© Indian Institute of Technology Delhi (IITD), New Delhi, 2026

DEVELOPMENT OF FLEXIBLE ELECTROMECHANICAL SENSORS FOR HUMAN MOTION MONITORING AND HUMAN MACHINE INTERFACE

by

MUJEEB YOUSUF

Centre for Applied Research in Electronics (CARE)

Submitted

in the fulfillment of the requirements of the degree of Doctor of Philosophy

to the



INDIAN INSTITUTE OF TECHNOLOGY DELHI

March 2026

Dedicated to

To my beloved Mom and Dad

Certificate

This is to certify that the thesis entitled **"Development of Flexible Electromechanical Sensors For Human Motion Monitoring and Human Machine Interface"**, submitted by **Mujeeb Yousuf** to the Indian Institute of Technology Delhi, for the award of the degree of **Doctor of Philosophy** in Central for Applied Research in Electronics (CARE), is a record of the original, bonafide research work carried out by him under my supervision and guidance. The thesis has reached the standards fulfilling the requirements of the regulations related to the award of the degree.

The results contained in this thesis have not been submitted in part or in full to any other University or Institute for the award of any degree or diploma to the best of our knowledge.

Prof. Pushpapraj Singh
Professor
Centre for Applied Research in Electronics,
Indian Institute of Technology Delhi.

Acknowledgements

"The best portion of a good man's life is his little, nameless, unremembered acts of kindness and of love." — William Wordsworth

Well, finally, I believe I am here, contemplating all the blessings I have received in this beautiful journey, marked by ups and downs, joys and sorrows. "Tashakur" to the Lord of the universe, the Almighty, who has woven each of us into the fabric of destiny. Countless blessings, infinite memories, diverse paths, and the passion of so many people behind this journey have enriched it. As I write these words, I am overwhelmed by the love of those who contributed to my experiences, guided me under their wings, and ignited within me a spark of passion.

Two important people, my supervisors, *Prof. Pushpapraj Singh* and *Prof. Muhammad Mustafa Hussain,* have been very patient with me throughout this journey. Prof. Singh guided me from the very beginning, offering every possible support through research discussions that shaped both my work and my capabilities. His patience, encouragement, and unwavering belief in me provided a strong foundation on which this thesis stands. Prof. Hussain gave me the opportunity to spend one and a half years at Purdue University. The privilege of pursuing my doctoral work under his mentorship brought out the best in me and constantly pushed me beyond my comfort zone. His warmth, care, and affection during these years greatly enriched my journey and contributed immensely to the quality and depth of this thesis.

I am grateful to the appointed members of my research assessment panel at the Indian Institute of Technology Delhi, *Prof. Anjana Basu*, and *Prof. Ankur Gupta*, for their valuable suggestions during the progress review meetings. I am equally grateful to the entire faculty of the Centre for Applied Research in Electronics (CARE), IIT Delhi. A special thanks to the faculty managing the facilities at the Nanoscale Research Facility (NRF) and the Central Research Facility (CRF) at IIT Delhi, as well as the Birck Nanotechnology Center at Purdue University, for providing access to world-class laboratory facilities during my research. I also extend my heartfelt thanks to the Anusandhan National Research Foundation (ANRF, formerly SERB) for supporting my Overseas Visiting Doctoral Fellowship (OVDF) at Purdue University.

This journey would have been incomplete without the wonderful colleagues at CARE. I found my mentors in *Dr. Dhairya*, *Dr. Sushil*, *Dr. Vaibhav*, and *Dr. Alka*. I found my friends in *Dr. Manu*, *Dr. John*, *Dr. Nitesh*, *Mr. Khanjan*, *Mr. Piyush*, *Mr. Sazid*, and *Mr. Sadat*. I am grateful for their support, insightful discussions, and the respect they have always shown. This journey was equally enriched by the wonderful colleagues and friends I met at Purdue University.

From the very beginning of this journey, I have been fortunate to meet many wonderful souls from the community at IIT Delhi that we proudly call the *"Kashmir Community"*. In moments of sadness, struggles, and frustration, they were the ones I could hold hands with. Together, we grew into a family whose bond will last long, and I will forever cherish the beautiful moments we shared.

To my parents, who made countless sacrifices while I was living this journey. My mother, *Nigeena Akhter*, with her endless prayers, tears, and love, gave wings to this journey. I would like to express my deepest gratitude to my father, *Mohammad Yousuf*, who always supported my decisions, gave me the freedom to pursue my dreams, and showered me with affection. I remain immensely thankful to my brother, *Muneeb Yousuf*, my sister, *Asiya Yousuf*, her husband, *Dr. Arsheed*, and my two wonderful nephews, *Azhaan* and *Zaid*, for their constant love and joy.

Lastly, I fondly remember my late grandfather, *Ghulam Mohiuddin Dar*, my first teacher and my first mentor, who taught me to be kind, affectionate, and responsible, and who always wished to see me flourish in life with success and good health. I am also grateful to my cousin, *Zubair*, who was my first comfort in the city of Delhi. He was there from the very beginning and provided every possible help.

Just as Wordsworth wrote of "little, nameless, unremembered acts of kindness," it is these acts that carried me through. May I carry them forward in all that I do.

Mujeeb Yousuf
19/03/2026

Abstract

This thesis presents the development of flexible electromechanical sensors tailored for next-generation applications in human motion monitoring and human–machine interfaces (HMIs). Conventional sensors are often fabricated on rigid substrates. As a result, these fail to conform to curved or dynamically moving surfaces. This makes them unsuitable for applications that require mechanical compliance.

Flexible sensors offer better form adaptability and skin conformity. However, those based on a single sensing mechanism often face a trade-off between sensitivity and sensing range. Devices with high sensitivity are typically limited to narrow sensing ranges, while those capable of operating over broader ranges tend to exhibit lower sensitivity. To address these limitations, hybrid and multimodal sensor architectures are introduced. These combine complementary transduction principles to achieve both high sensitivity and a broad dynamic range. Moreover, multimodal sensor systems support multi-stimulus detection. They can sense strain, pressure, and proximity in a single device. This enhances adaptability for complex and interactive environments.

To realize these capabilities, the thesis begins with a hybrid capacitive–resistive sensor that enables high sensitivity across a wide pressure range. The sensor switches between non-contact capacitive sensing and contact piezoresistive sensing depending on applied pressure. The capacitive response operates in the low-pressure regime (0.3–15 kPa) with a peak sensitivity of 0.013 kPa^{-1}, while the piezoresistive response covers 15–86 kPa with a sensitivity of 0.037 kPa^{-1}. The dual strategy of mechanical isolation via SU-8 spacers and electrical isolation via parallel readout architecture is also employed to suppress crosstalk below 0.3%. Building on this, a multifunctional capacitive sensor for human motion monitoring is developed that leverages two structural strategies. One design incorporates asymmetric electrodes and a μ-meshed PDMS dielectric to achieve direction-sensitive strain detection. The asymmetric electrode array provides a vectored strain response with a displacement sensitivity of $(1.341\hat{\imath}+2.007\hat{\jmath}+8.750\hat{k})$ pF/mm. Its reusable polymer mold facilitates batch fabrication and scalability. The other employs a magneto-dielectric-based bimodal capacitive device to enable both strain and contactless sensing through a single capacitive output readout. The device achieves a four-fold improvement in strain sensitivity and a 1.5-fold increase in proximity sensitivity compared to planar

structures. It can distinguish conducting from non-conducting approaching objects, showing nearly 23 times higher sensitivity for conducting materials and a detection range up to 21 mm.

Next, a piezoelectric–capacitive hybrid sensor is introduced to capture both static and dynamic pressure signals. By combining steady-state capacitive response with transient piezoelectric signals, the device extends pressure detection from 1 to 140 kPa, achieving sensitivities of 30 fF/kPa for low static pressures and 150 mV/kPa for dynamic pressures. This adds a temporal dimension to tactile sensing, useful for capturing dynamic impact and realistic touch patterns. Finally, a high-resolution 64×64 tactile array (4096 pixels) built using the same magneto-dielectric material is presented, achieving a device density of 846 sensors/ cm^2. The array features 100×100 m pixels and a wide pressure range (0.37–30.86 kPa). System validation includes multi-wafer repeatability tests and 2D mapping of complex contours. While operating in capacitive mode, this system demonstrates scalable sensor density, seamless integration with a flexible PCB-based analog readout for surface texture mapping.

For each platform, complete sensor-to-system functionality is achieved through integration with flexible PCB-based readout systems. These systems, built from commercial off-the-shelf ICs, enable real-time data acquisition, wireless transmission, and application demonstrations. Each platform is validated through finite element simulations (COMSOL Multiphysics) and experimental characterization. Demonstrations include human motion tracking, HMI, and surface texture recognition. These establish a foundation for scalable, biomimetic, and high-performance electromechanical sensors for HMIs and human motion monitoring.

सारांश

यह शोध-प्रबंध मानव गति निगरानी (Human Motion Monitoring) तथा मानव–मशीन इंटरफेस (Human–Machine Interfaces, HMIs) जैसे अगली पीढ़ी के अनुप्रयोगों के लिए लचीले विद्युत-यांत्रिक संवेदकों के विकास को प्रस्तुत करता है। पारंपरिक संवेदक प्रायः कठोर सब्सट्रेट पर निर्मित किए जाते हैं, जिसके परिणामस्वरूप वे घुमावदार या गतिशील सतहों के अनुरूप स्वयं को ढाल नहीं पाते। इस कारण वे उन अनुप्रयोगों के लिए उपयुक्त नहीं होते जिनमें यांत्रिक अनुकूलता (mechanical compliance) की आवश्यकता होती है।

लचीले संवेदक बेहतर आकार-अनुकूलन (form adaptability) और त्वचा-समान अनुकूलता (skin conformity) प्रदान करते हैं। तथापि, एकल संवेदन तंत्र (single sensing mechanism) पर आधारित संवेदक प्रायः संवेदनशीलता (sensitivity) और मापन सीमा (sensing range) के बीच समझौते का सामना करते हैं। उच्च संवेदनशीलता वाले उपकरण सामान्यतः सीमित मापन सीमा में कार्य करते हैं, जबकि व्यापक मापन सीमा वाले उपकरणों में संवेदनशीलता अपेक्षाकृत कम होती है। इन सीमाओं को दूर करने के लिए इस शोध में हाइब्रिड तथा मल्टीमोडल संवेदक संरचनाएँ प्रस्तुत की गई हैं, जो पूरक ट्रांसडक्शन सिद्धांतों (complementary transduction principles) को संयोजित करके उच्च संवेदनशीलता और विस्तृत डायनेमिक रेंज दोनों प्राप्त करती हैं। इसके अतिरिक्त, मल्टीमोडल संवेदक प्रणालियाँ एक ही उपकरण में बहु-उत्तेजना (multi-stimulus) — जैसे तनाव (strain), दबाव (pressure) और निकटता (proximity) — का पता लगाने में सक्षम होती हैं, जिससे वे जटिल और इंटरैक्टिव वातावरणों के लिए अधिक अनुकूल बनती हैं।

इन क्षमताओं को साकार करने के लिए शोध-प्रबंध की शुरुआत एक हाइब्रिड कैपेसिटिव–रेजिस्टिव संवेदक से की गई है, जो व्यापक दबाव सीमा में उच्च संवेदनशीलता प्रदान करता है। यह संवेदक लगाए गए दबाव के आधार पर गैर-संपर्क कैपेसिटिव संवेदन और संपर्क पायज़ोरिज़िस्टिव संवेदन के बीच स्विच करता है। कैपेसिटिव प्रतिक्रिया निम्न दबाव क्षेत्र (0.3–15 kPa) में कार्य करती है और 0.013 kPa^{-1} की अधिकतम संवेदनशीलता प्रदर्शित करती है, जबकि पायज़ोरिज़िस्टिव प्रतिक्रिया 15–86 kPa तक विस्तृत होती है और 0.037 kPa^{-1} की संवेदनशीलता प्रदान करती है। SU-8 स्पेसरों द्वारा यांत्रिक पृथक्करण तथा समानांतर रीडआउट आर्किटेक्चर द्वारा विद्युत पृथक्करण की संयुक्त रणनीति का उपयोग करके क्रॉस-टॉक को 0.3% से कम रखा गया है।

इसके आधार पर मानव गति निगरानी के लिए एक बहु-कार्यात्मक कैपेसिटिव संवेदक विकसित किया गया है, जिसमें दो संरचनात्मक रणनीतियाँ अपनाई गई हैं। प्रथम डिज़ाइन में असममित इलेक्ट्रोड और μ-मेश PDMS डाइलेक्ट्रिक का उपयोग किया गया है, जिससे दिशा-संवेदी तनाव पहचान संभव होती है। यह असममित इलेक्ट्रोड सरणी $(1.341\hat{i} + 2.007\hat{j} + 8.750\hat{k})$ pF/mm

की विस्थापन संवेदनशीलता के साथ वेक्टर-आधारित स्ट्रेन प्रतिक्रिया प्रदान करती है। इसका पुनःप्रयोग योग्य पॉलिमर मोल्ड बैच निर्माण और स्केलेबिलिटी को सक्षम बनाता है। दूसरा डिज़ाइन मैग्नेटो-डाइलेक्ट्रिक आधारित बायमोडल कैपेसिटिव उपकरण पर आधारित है, जो एक ही कैपेसिटिव आउटपुट रीडआउट के माध्यम से तनाव और संपर्क-रहित संवेदन दोनों को संभव बनाता है। यह उपकरण समतल संरचनाओं की तुलना में तनाव संवेदनशीलता में चार गुना तथा निकटता संवेदनशीलता में 1.5 गुना वृद्धि प्रदर्शित करता है। साथ ही यह चालक और अचालक निकट आती वस्तुओं के बीच अंतर कर सकता है, जहाँ चालक पदार्थों के लिए लगभग 23 गुना अधिक संवेदनशीलता तथा 21 mm तक की पहचान सीमा प्राप्त होती है।

इसके पश्चात् एक पायज़ोइलेक्ट्रिक–कैपेसिटिव हाइब्रिड संवेदक प्रस्तुत किया गया है, जो स्थिर तथा गतिशील दोनों प्रकार के दबाव संकेतों को दर्ज कर सकता है। स्थिर-अवस्था कैपेसिटिव प्रतिक्रिया और क्षणिक पायज़ोइलेक्ट्रिक संकेतों के संयोजन द्वारा यह उपकरण 1–140 kPa के दबाव क्षेत्र में कार्य करता है, जिसमें स्थिर दबाव के लिए 30 fF/kPa तथा गतिशील दबाव के लिए 150 mV/kPa की संवेदनशीलता प्राप्त होती है। इससे स्पर्श संवेदन में एक कालिक (temporal) आयाम जुड़ता है, जो गतिशील प्रभावों तथा वास्तविक स्पर्श पैटर्न को रिकॉर्ड करने में सहायक है।

अंततः उसी मैग्नेटो-डाइलेक्ट्रिक सामग्री का उपयोग करते हुए 64×64 (4096 पिक्सेल) की उच्च-रिज़ॉल्यूशन स्पर्श सरणी विकसित की गई है, जिसकी संवेदक घनत्व 846 सेंसर/cm^2 है। इस सरणी का पिक्सेल आकार 100×100 μm है और यह 0.37–30.86 kPa के दबाव क्षेत्र में कार्य करती है। प्रणाली सत्यापन में बहु-वेफर पुनरावृत्ति परीक्षण तथा जटिल आकृतियों की द्वि-आयामी मैपिंग शामिल है। कैपेसिटिव संचालन के दौरान यह प्रणाली उच्च सेंसर घनत्व, लचीले PCB-आधारित एनालॉग रीडआउट के साथ सुगम एकीकरण तथा सतह बनावट मैपिंग प्रदर्शित करती है।

प्रत्येक प्लेटफॉर्म में सेंसर-से-सिस्टम स्तर की पूर्ण कार्यक्षमता लचीले PCB-आधारित रीडआउट प्रणालियों के साथ एकीकरण द्वारा प्राप्त की गई है। ये प्रणालियाँ वाणिज्यिक ऑफ-द-शेल्फ ICs से निर्मित हैं और वास्तविक-समय डेटा अधिग्रहण, वायरलेस ट्रांसमिशन तथा अनुप्रयोग प्रदर्शन को सक्षम बनाती हैं। प्रत्येक प्लेटफॉर्म का सत्यापन सीमित तत्त्व सिमुलेशन (COMSOL Multiphysics) तथा प्रायोगिक विश्लेषण द्वारा किया गया है। प्रदर्शनों में मानव गति ट्रैकिंग, मानव–मशीन इंटरफेस (HMI) नियंत्रण और सतह बनावट पहचान शामिल हैं।

ये परिणाम मानव–मशीन इंटरफेस तथा मानव गति निगरानी के लिए स्केलेबल, बायोमिमेटिक और उच्च-प्रदर्शन विद्युत-यांत्रिक संवेदकों के विकास के लिए एक सुदृढ़ आधार स्थापित करते हैं।

Contents

Certificate i

Acknowledgements iii

Abstract v

सारांश vii

Contents ix

List of Figures xiii

List of Tables xxiii

Abbreviations xxv

Symbols xxvii

1 Introduction 1

1.1 Overview of Flexible Electronics 1
1.2 Transduction Mechanism 5
1.2.1 Capacitive 6
1.2.2 Piezoresistive 7
1.2.3 Piezoelectric 7
1.2.4 Triboelectric 9
1.3 Structural and Material Innovation 9
1.3.1 Structural Micro-engineering 10
1.3.2 Material Innovations 15
1.4 System Level Integration 19
1.5 Rationale and Objective 23
1.6 Thesis Organization 24

2 Flexible Suspended Hybrid Tactile Sensor with Crosstalk-Free Design for Human–Machine Interfaces **27**
2.1 Introduction . . . 28
2.2 Device Concept and Design . . . 29
2.3 Fabrication Process Flow . . . 33
2.4 Results and Discussions . . . 36
2.4.1 Morphological Characterization . . . 36
2.4.2 Electromechanical Characterization . . . 38
2.4.3 Readout Electronic Circuitry . . . 44
2.4.4 Cross-talk and Multitouch . . . 48
2.5 Application . . . 52
2.6 Conclusion . . . 54

3 Direction-Sensitive and Bimodal Capacitive Sensors for Human Motion Monitoring **57**
3.1 Asymmetric Capacitive Pixel Array for Mapping Epidermal Vectored Movement . . . 58
3.1.1 Introduction . . . 58
3.1.2 Device Concept and Design . . . 60
3.1.2.1 Working Mechanism . . . 60
3.1.2.2 Analytical Model . . . 61
3.1.3 Fabrication Process Flow . . . 64
3.1.4 Results and Discussion . . . 67
3.1.5 Conclusion . . . 72
3.2 Bimodal E-Skin for Human Motion Monitoring . . . 73
3.2.1 Introduction . . . 73
3.2.2 Device Concept and Design . . . 75
3.2.3 Finite Element Modeling . . . 77
3.2.4 Fabrication Process Flow . . . 78
3.2.5 Results and Discussion . . . 80
3.2.5.1 Strain Sensing Performance . . . 80
3.2.5.2 Proximity Sensing Performance . . . 83
3.2.5.3 Electronic Readout Circuitry . . . 85
3.2.6 Application to Real-time Limb Movement Tracking . . . 87
3.2.7 Conclusion . . . 88

4 Multimodal Sensors for Static and Dynamic Pressure Sensing **89**
4.1 Poroelastic $BaTiO_3$/PDMS for Dynamic Pressure Sensing . . . 90
4.1.1 Introduction . . . 90
4.1.2 Device Concept and Design . . . 92
4.1.3 Finite Element Modelling . . . 93
4.1.4 Fabrication Process Flow . . . 95

4.1.5 Electromechanical Characterization . . . 97
4.1.6 Conclusion . . . 100
4.2 Multimodal Integrated Device for Static and Dynamic Sensing . . . 101
4.2.1 Introduction . . . 101
4.2.2 Device Concept and Design . . . 103
4.2.2.1 Working Mechanism . . . 104
4.2.3 Fabrication Process Flow . . . 105
4.2.4 Results and Discussion . . . 106
4.2.5 Conclusion . . . 109

5 Sub-mm High-Resolution Flexible Capacitive Sensor Array for Surface Texture Mapping 111
5.1 Introduction . . . 112
5.2 Device Concept and Design . . . 114
5.2.1 Sensing Method . . . 114
5.3 Finite Element Modelling (FEM) . . . 116
5.4 Fabrication Process Flow . . . 118
5.5 Readout Circuit Design . . . 120
5.6 Results and Discussion . . . 122
5.7 Conclusion . . . 128

6 Conclusion and Future Outlook 131
6.1 Summary of the Research . . . 131
6.2 Scope for Future Work . . . 134
6.2.1 Multi-functional and Multi-modal Devices . . . 134
6.2.2 Standalone Truly Flexible Electronic Systems: From FHE to Transformational Electronics . . . 135
6.2.3 Flexible Electronics for Neural Interfaces . . . 136

Scope for Future Work 137

A Experimental Setup 137

B Analytical Derivation of Filling Factors 139

C Schematic of Parallel Readout Circuitry 145

Bibliography 147

List of Publications **175**

Curriculum Vitae **181**

List of Figures

1.1 Evolution of sensor technologies across four generations from mechanical responses (dials, color changes) to electrical outputs, miniaturized devices, and intelligent Sensors 4.0 systems. The shift toward Sensors 4.0 highlights the need for flexible sensors [1]. 2

1.2 The marketing prediction of the flexible electronics up to the year 2032 with electromechanical sensors dominating the market [2] 3

1.3 Structure of human skin showing mechanoreceptors: Merkel (MD) and Ruffini (RE) for static stimuli, Meissner (MC) and Pacinian (PC) for dynamic stimuli, and its capabilities. [3]. 4

1.4 Transduction mechanisms in flexible electromechanical sensors: (a) Triboelectric, (b) Capacitive, (c) Piezoelectric, and (d) Piezoresistive [4]. 5

1.5 a) Schematic of a double-sided μ-pyramidal structure, consisting of a PDMS/Zn dielectric layer sandwiched between graphene nanowire (GNW)-based electrodes [5]. (b) 3D schematic of the device with its equivalent circuit, where C_{es} is the inter-electrode capacitance and C_{top} and C_{bottom} are the electrical double-layer (EDL) capacitances of the top and bottom interfaces [6]. 12

1.6 (a) Schematic illustrating the double-sided micro-pyramidal structure. The device consists of a PDMS/Zn dielectric layer sandwiched between graphene nanowire (GNWs)-based electrodes [5]. (b) Schematic illustrating a fully packaged device with μ-spherical micro-engineered dielectric layer and its SEM image [7]. 13

1.7 (a) Device concept of the graphene oxide (GO) foam-based pressure sensor. (b) SEM images showing the porous network structure. (c) Relative capacitance change as a function of pressure [8]. 13

1.8 (a) Schematic illustrations of the micropillar-based capacitive electromechanical sensor. (b) Fabrication process of the device. (c) Optical image and the SEM image of the fabricated device [9] 14

1.9 Fabrication steps of the sandwich-like pressure sensor based on low-cost nylon netting with numerous microsized square holes [10]. 16

1.10 a) Schematic of the fabrication process for a metal nanofiller-based pressure sensor. (b) Cross-sectional view showing nanogratings filled with metal nanofillers. (c) Exploded schematic highlighting the two coplanar electrodes that enable pressure sensing [11]. 18
1.11 Schematic illustrating the different components of the integrated system. The sensors collect the data, AFE filters and converts the signals into MCU-readable signals, MCU processes the data, controls the flow of data and sends it for transmission via BLE/WiFi/NFC. . 19
1.12 Integrated system schematic of a skin-interfaced wearable biosensor for monitoring sweat biomarkers, including CRP, pH, temperature, and ionic strength [12]. 22

2.1 (a) Schematic of the hybrid tactile sensor consisting of a suspended PEDOT:PSS/LIG/PDMS membrane positioned above interdigitated electrodes (IDEs), separated by an SU-8-defined air gap. The electrodes appear as parallel strips due to the sectional representation of the spiral geometry. (b–d) Sensing mechanism under different pressure regimes: (b) Initial state with no pressure; (c) Capacitive mode under subtle pressure, where membrane deflection alters the capacitance; (d) Resistive mode under high pressure, where the sensing layer contacts the IDE. 30
2.2 Partial capacitance model showing decomposition of effective permittivity across the multilayer dielectric stack: environment, PDMS, LIG, PEDOT:PSS, and air gap. 32
2.3 Schematic of the fabrication process flow: (1) Electrode patterning with SU-8 cavity formation, (2) Tri-layer membrane fabrication (PEDOT:PSS/LIG/PDMS), and (3) Final device integration using plasma-assisted bonding. 34
2.4 Morphological evolution and structural integration of LIG. (a–c) Surface-view SEM images showing under-lased (15%), optimized (22%), and over-lased (28%) LIG morphologies. (d) Cross-sectional SEM image of bilayer LIG/PDMS structure. (e) Cross-sectional SEM image of trilayer PEDOT:PSS/LIG/PDMS after polymer infiltration. 36
2.5 Top SEM images: (a) LIG showing the mesopores in the range of 3-6 μm (b) LIG-coated PEDOT:PSS showing filling up of the pores to increase the conductivity. 37

2.6 (a) Capacitive response of the device in the non-contact regime (1.2–14.1 kPa), demonstrating increasing capacitance with applied pressure. The inset highlights the proximity effect as the force gauge approaches the membrane. (b) Enlarged view of the low-pressure region (1.2–3.2 kPa), showing fine-scale capacitive changes. (c) Comparative capacitive response of bi-layer (LIG/PDMS) and tri-layer PEDOT:PSS/LIG/PDMS) membranes, illustrating enhanced performance with the tri-layer design. (d) (i) Electromechanical response across different modes. At 15 kPa, the device shows the transition from capacitive to resistive mode. 39

2.7 (a) I–V characteristics of the device in the contact regime, showing a linear relationship and confirming ohmic conduction. The inset provides a zoomed-in view of the first quadrant. (b) Resistance variation as a function of applied pressure (15–86 kPa), with an inset showing the dynamic response across multiple loading cycles. 40

2.8 Sensitivity analysis of the suspended PEDOT:PSS/LIG/PDMS hybrid tactile sensor. (a) Capacitive mode: relative capacitance change ($\Delta C/C_0$) vs. pressure (0–14.1 kPa); linear fit yields $S_C \approx 0.013\,\mathrm{kPa}^{-1}$ ($R^2 = 0.97$). (b) Resistive mode: normalized resistance change ($\Delta R/R$) vs. pressure (15–86 kPa), revealing three sub-regimes: $S_R \approx 0.037\,\mathrm{kPa}^{-1}$ ($R^2 = 0.97$) from 15–31 kPa, $S_R \approx 0.008\,\mathrm{kPa}^{-1}$ ($R^2 = 0.94$) from 31–55 kPa, and $S_R \approx 0.001\,\mathrm{kPa}^{-1}$ ($R^2 = 0.98$) above 55 kPa. 41

2.9 (a) Transient response of the device in capacitive mode, exhibiting a rise time of 160 ms. (b) Time-domain response of the device in resistive mode, exhibiting a rise time of 71 ms. 42

2.10 (a) Combined electromechanical response in hybrid capacitive–resistive mode, covering the full pressure range (0–86 kPa) 43

2.11 Stability test result of the device in 2400 cycles. (a) In capacitive mode for 1200 cycles. (b) In resistive mode for 1200 cycles. 44

2.12 (a) Circuit diagram of the modular readout system with a 20 ms refresh rate. (b) Implementation of the circuit on a flexible PCB interfaced with ESP32 for wireless data transmission. 45

2.13 System characterization of the 24-pixel tactile tile. (A) Current consumption profile during the staged activation of system components, from the MSP-only baseline to the full data pipeline, measured with a Nordic PPK2. (B) The corresponding decomposed power budget for each operational state, highlighting the incremental contributions of the ESP32, Wi-Fi, TCP, and UART subsystems. (c) Power scaling projection for larger arrays, comparing the total system power for a 512-pixel array using the current ESP32-per-tile architecture versus alternative low-power bridge solutions with fixed overheads. 47

2.14 Crosstalk suppression strategies in the device architecture: (a) Exploded view showing the layered structure of the sensor. (b) Each IDE is routed to a dedicated analog-to-digital converter (ADC) to prevent electrical crosstalk or signal bleeding. (c) The patterned functional layer confines conduction paths, minimizing electrical crosstalk across adjacent pixels. (d) SU-8 cavities act as mechanical isolation barriers to suppress deformation-induced coupling. 50
2.15 Cross-talk-free and multi-touch sensing demonstration: (a-b) Sensor schematics showing measurement points, (c-d) Heatmap responses demonstrating pixel isolation, (e-f) Selective actuation of specific pixels (e.g., S3, S5, S23) showing independent, localized responses with no signal overlap, confirming channel separation integrity. 51
2.16 (a) Schematic of the pressure-based multi-parameter authentication system (MPAS) for secure digital lock applications. (b) Photograph of the tactile sensing array integrated into the lock interface. (c) Waveform plot of a verified password attempt ("7722") showing correct digit–pressure mapping. (d) Waveform plot of a failed attempt with mismatched pressure levels despite correct digits. (e) Schematic of the tactile device used as a Human–Machine Interface (HMI) for a Mario-style platformer game, highlighting the closed-loop feedback between player input and game display. (f) Gameplay screenshots demonstrating tactile control of Mario for forward, backward, jump, and stop actions. 53

3.1 Schematic of the 3-D prototype of E-CaP in the relaxed state showing key components. 60
3.2 2-D schematic of the unit pixel of E-CaP. (a) Initial position. (b) Displacement of the top electrode with respect to the bottom electrode in the x-direction. (c) Displacement of the top electrode with respect to the bottom electrode in the y-direction 61

3.3 Fabrication process. (a) Spin coating of SU-8 (500 μm) on Si substrate followed by pre-exposure bake (at 100 °C for 2.5 min). (b) Exposure (E = 25 mJ/cm^2) of SU-8 using photomask. (c) Development of SU-8 after post-exposure bake (at 105 °C for 5 min) for the formation of μ-mold. Thereafter, spin coating of the thin layer of liquid paraffin is used to facilitate the release of PDMS μ-mesh in the subsequent step. (d) Pouring of the known volume of PDMS at the edge of the substrate to fill to a certain height of SU-8 micropillars. (e) Peeling-off PDMS μ-mesh from SU-8 μ-mold. The SU-8 μ-mold can be reused for batch fabrication of PDMS μ-mesh. (f) Deposition of aluminum (∼100 nm) on two different thicknesses of PET sheet using thermal evaporation. (g) Exposure and patterning of a 3 × 3 asymmetric capacitive electrode array. (h) Coating of the thin layer of PDMS (5 μm at 8 k r/min) to facilitate proper adhesion in the next step. Prior to spin coating of a thin layer of PDMS, the PET sheet is treated with the diluted amine-PDMS linker. The amine linker forms a urethane linkage on the PET sheet, which facilitates the bond formation with the PDMS. (i) Assembling of PDMS μ-mesh and 3 × 3 asymmetric capacitive electrode array followed by curing (at 95 °C for 90 min) to form E-CaP. 65

3.4 SEM image of the μm-mold of SU-8. The inset shows the gap and height of the hexagonal μm-pillar. The μm-mold can be reused for a batch fabrication 66

3.5 (a) Stress distribution in the PDMS μ-mesh at a gap of 0.2 mm between adjacent hexagons. (b) Stress distribution in the PDMS mesh when the gap is less than 0.2 mm. The stress generated is uneven throughout the PDMS μ-mesh. 68

3.6 Shear displacement generated in the PDMS μ-mesh at different dimensions of hexagons due to shear force. The decrease in volume of the hexagon reduces the porosity, which in turn reduces the sensitivity of the device. 68

3.7 Experimental setup for the measurement of the vectored response of fabricated E-CaP 69

3.8 Real-time vectored capacitive response of E-CaP in global Cartesian coordinates. The inset shows the transition noise during the relative displacement of asymmetrical electrodes. 70

3.9 (a) Mapping of the simulated capacitive response of E-CaP in the xy spatial domain, defining the region of operation. (b) Mapping of the capacitive response of E-CaP in Z spatial domain, defining the region of operation. 71

3.10 Concept of the bimodal M-IDE sensor. (a–b) Strain-sensing mechanism: bending alters inter-particle separation ($g \rightarrow g'$) within the MDL, reducing the effective dielectric constant and capacitance. (c–d) Proximity-sensing mechanism: approaching objects perturb fringing fields, generating additional capacitance (C_{prox}). Together, these effects enable simultaneous strain and proximity detection with a single capacitive readout. 76
3.11 (a) Schematic of the M-IDE device showing different layers. A thin flexible PET sheet (150 μm) is used as the substrate, with interdigitated electrodes (IDEs) fabricated on top. The sensing layer consists of magnetic nanoparticles (MNPs) blended in PDMS. (b) Simulation results showing the capacitance change as a function of separation, correlated with the effective dielectric constant. 77
3.12 Fabrication process of P-IDE and M-IDE devices. (a–b) Lithographic patterning of IDEs on Al-coated PET substrates. (c) P-IDE prepared by spin-coating PDMS. (d) M-IDE is fabricated by spin-coating MDL (PDMS + magnetic nanoparticles). (e–f) Optical images of M-IDE in relaxed and bent states. 79
3.13 Comparison of strain sensing between P-IDE and M-IDE. (a) M-IDE shows enhanced sensitivity and a greater working range (6–20 mm) compared to P-IDE. M-IDE working range is divided into three distinct sensitivity regimes: two linear regions and a nonlinear transition region with the highest sensitivity of 27.8 m^{-1} (b) Step response at different radii of curvature (ROCs) that correspond to varying separation within MDL. 81
3.14 Dynamic response of M-IDE. (a) Strain response at ROC = 8 mm for one cycle. (b–c) Response and relaxation times measured as 200 ms and 250 ms, respectively. (d) Repeatability over 1000 bending cycles at ROC = 8 mm, showing highly stable and durable performance with consistent amplitude. Insets show magnified start and end cycles, confirming excellent reliability. 82
3.15 Proximity-sensing performance of M-IDE. (a) Sensitivity (S_{Prox})) to non-conducting objects is 1.5× higher than P-IDE. (b) Response of the M-IDE to conducting objects at varying proximity distances. (c) Universal proximity response of M-IDE for both conducting and non-conducting objects. Sensitivity for conducting objects is found to be ∼23× higher, highlighting the M-IDE's strong metal-detection capability. The inset shows the experimental setup with 0.0 mm defined as the point of contact. (d) Short-range proximity sensitivity in M-IDE for conducting objects is 93.23 fF/mm, significantly higher than 4.30 fF/mm for non-conducting objects. 84

3.16 Electronic readout circuitry for M-IDE integration. (a) Block diagram showing sensor interfacing with AD7746 capacitance-to-digital converter, ESP32-S3 microcontroller, USB–serial interface, and Wi-Fi transmission. (b) Power profiles comparing continuous mode (132 mA, 7.55 h lifetime) and delay mode (78 mA, 12.77 h), demonstrating effective firmware-based power optimization for portable applications. 86
3.17 Real-time motion tracking with M-IDEs attached to the elbow, wrist, hand, and knee. A goniometer was used to calibrate bending angles (e.g., 45° and 90°). The device reliably distinguishes non-bending (N-BS) and bending states (BS). 87

4.1 The stress analysis of a simulated model of a flexible piezoelectric pressure sensor. (a) Cross-sectional view of a model with no porosity. (b) Top view of a model with no porosity. (c) Cross-sectional view of a model with porosity. (d) Top view of a model with porosity. The stress analysis shows that for the same applied pressure (100 kPa), the porous model deforms more, giving a higher stress generation as well as a higher probability of nanoparticle cross-linking compared to the non-porous model. 93
4.2 2-D plots for optimizing the weight % of BTO in PDMS and % porosity in the substrate. (a) Voltage generated at different % porosity and weight ratios of BTO nanoparticles in PDMS. (b) Average stress generated at different weight ratios of BTO in PDMS and % porosity. The plots indicate that the maximum voltage is generated at a 15% weight ratio and 16% substrate porosity. 94
4.3 Fabrication process of the PBM sensor. (a) PDMS base and curing agent are thoroughly mixed in a ratio of 10:1 for about 20 min. (b) 15% by weight of BTO is added to the PDMS solution. (c) Sugar template is placed in the BTO/PDMS nanocomposite, and the nanocomposite is allowed to soak in it. (d) Poroelastic matrix of the nanocomposite-soaked sugar cube. (e) A thin nanocomposite layer is sliced and sandwiched between the copper electrodes. (f) Device prototype of a fabricated PBM sensor. 96
4.4 SEM image. (a) Nonporous composite in which BTO NPs are homogeneously blended with PDMS. (b) PBM flexible sensor showing the porous network. 97
4.5 (a) Sensor response at different % weight ratios of BTO in PDMS. (b) Frequency response of the PBM sensor. The generated voltage remains constant over a frequency range (0–5 Hz). 98

4.6 (a) Compressive stress–strain curve of the non-porous BTO/PDMS sample. The calculated elastic modulus (E_c) of the sample is 12 MPa. (b) Compressive stress–strain curve of the PBM sensor. The calculated E_c of the sample is 83 kPa. The introduction of porosity results in a lower compressive modulus of the PBM sensor, indicating that smaller forces generate larger deformation and, hence, account for higher sensitivity. 98
4.7 Voltage response at different pressures. (a) Voltage generated in nonporous BTO/PDMS composite at a weight ratio of 15%. (b) Voltage generated in the PBM sensor at 15%. weight ratio of BTO in PDMS. The results show that the PBM generates a voltage two times greater than nonporous sensor. The inset shows the switching polarity test of the PBM sensor. 99
4.8 (a) Comparison of responses for nonporous and PBM sensors at 50 kPa. (b) Sensitivity (S) curve of the sensors for different pressures. . 100
4.9 Conceptual Image of the multi-mode device. The device integrates the capacitive-piezoelectric sensors for the static and dynamic mechano-response. This synergetic effect allows detection of pressure stimuli over a broad sensing range (1-140 kPa). 103
4.10 Schematic of the fabrication process of the multimode device. The process is divided into three main steps: fabrication of the capacitive sensor, fabrication of the piezoelectric sensor, and integration of both components. (a) Fabrication of the silicon mold via standard photolithography followed by wet etching of silicon using KOH. (b) Spin coating of PDMS onto the silicon mold. (c) Peeling off the cured PDMS to obtain the μ-pyramidal structure. (d) Sandwiching the μ-pyramidal PDMS between two electrodes to form the capacitive sensor. (e) Deposition of a gold electrode on a PET sheet using e-beam evaporation to serve as the bottom electrode. (f) Spin coating of the piezoelectric layer onto the bottom electrode. (g) Fabrication of the top electrode. (h) Final integration of the capacitive and piezoelectric layers to form the multimode device. 105
4.11 (a) SEM image of the μ-pyramidal PDMS layer. (b) Magnified view showing a single μ-pyramid. 106
4.12 Capacitive response of the multi-mode mechanoreceptor. The device can detect the minimum pressure of 1 kPa (b) Dynamic electromechanical characterization of piezoelectric device. The device has a working range of 20-140 kPa with peak-to-peak voltage generation of 16V. 107
4.13 Sensing range of the multi-mode mechanoreceptor. The capacitive device detects minimum pressure of 1 kPa while piezoelectric device has working range of 20-140 kPa. 108

4.14 The voltage response of Fast adapting (piezoelectric device) and Slow adapting (capacitive device) mechano-receptor from holding to releasing of the object. 109

5.1 (a) Conceptual schematic of the tactile sensing array and a single pixel showing different layers of the pixel. (b) Schematic describing the sensing mechanism of the device. One device has PDMS as a dielectric, while another has MDL as a dielectric. The capacitance in the former device is a function of the gap between the electrodes, while the latter device capacitance is a function of both the gap and the volume fraction of NPs. 115
5.2 Comparison of an FEM simulation of a capacitance change of the single pixel with PDMS-only dielectrics and magnetodielectric layer (MDL). 117
5.3 Schematic illustrating the fabrication process for the flexible high-density sensor array. The process begins with (a) silicon as a temporary carrier. (b) Spin-coating of the polyimide (PI) substrate. (c) Sputtering and patterning of the bottom electrode. (d) Spin-coating of the magnetodielectric layer (MDL). (e) Sputtering and patterning of the top electrode. (f) Spin-coating of PDMS as the encapsulation layer. (g) Finally, peeling off the completed flexible sensor array. (h) Optical image of the fabricated sensor array demonstrating mechanical flexibility. 119
5.4 (a) Schematic of the readout electronics for the 64×64 capacitive tactile array, showing multiplexers, CDC, and control circuitry. (b) Flexible two-layer PCB integrating analog front-end, control, and communication modules. 121
5.5 Experimental setup for electromechanical characterization of the tactile array, including the Mark-10 force gauge (1 mN resolution) mounted on the ESM303 motorized tester. 122
5.6 Individual (single) pixel characterization. (a) Response of the applied pressure on a single pixel (b) Capacitance change following the dynamic applied force, showing better electromechanical coupling. . . 123
5.7 (a) Dynamic time response of a single pixel, showing a response time of 150 ms. (b) Capacitive response of pixels located at different corners of the device. 124
5.8 Capacitance response of the sensor array across the full force range (0–2.7 N), showing a minimum detectable load of 0.03 N and saturation at 2.5 N. 126
5.9 2D pressure mapping using the high-resolution tactile array. Heatmaps correspond to (a) 3D-printed letters “INL”. (b) A circular ring profile. 127

A.1 Experimental setup for electromechanical characterization. 137

C.1 Schematic of MSP430-ESP32 parallel readout architecture. 145

List of Tables

2.1 Geometrical Parameters of the Tactile Sensor Array 35
2.2 Benchmark Comparison with Previously Reported Flexible Pressure Sensors. 52

3.1 Simulation Parameters 71
3.2 Comparison of Previously Reported Directional Tactile Sensing Approaches with the Proposed E-CaP Sensor. 72

5.1 Dimensions and Material Properties 117
5.2 Comparison with Previously Reported Works 129

Abbreviations

ADC	**A**nalog-to-**D**igital **C**onverter
AFE	**A**nalog **F**ront-**E**nd
BTO	**B**arium **T**itanate
BLE	**B**luetooth **L**ow **E**nergy
CDC	**C**apacitance-to-**D**igital **C**onverter
E-CaP	**E**pidermal **Ca**pacitive **P**ixel
FEM	**F**inite **E**lement **M**odelling
HMI	**H**uman–**M**achine **I**nterface
IDE	**I**nterdigitated **E**lectrodes
LIG	**L**aser-**I**nduced **G**raphene
MDL	**M**agneto**d**ielectric **L**ayer
MEMS	**M**icro**e**lectromechanical **S**ystems
MPAS	**M**ulti-**P**ressure **A**uthentication **S**ystem
PCB	**P**rinted **C**ircuit **B**oard
PDMS	**P**olydimethyl**s**iloxane
PEDOT:PSS	**P**oly(3,4-ethylenedioxythiophene): **P**olystyrene **S**ulfonate
PI	**P**oly**i**mide
PVDF	**P**oly**v**inylidene **f**luoride
RIE	**R**eactive **I**on **E**tching
SEM	**S**canning **E**lectron **M**icroscopy

Symbols

S	Sensitivity of the sensor
P	Applied pressure (kPa)
σ	Stress
ρ	Specific resistivity
ε_0	Permittivity of free space
ε_r	Relative permittivity
d	Displacement
E	Young's modulus
V	Voltage
I	Current

Chapter 1

Introduction

This chapter gives a brief overview of flexible electronics as well as introduces some basic concepts and working principles of the electromechanical sensors. Existing bottlenecks limiting the full-scale dynamic range and sensitivity are also discussed. A literature review of different types of configurations and implementations, along with a summary of the state-of-the-art, is presented.

1.1 Overview of Flexible Electronics

Sensor technologies have developed in successive generations. Each generation demonstrates a new way to capture and interpret physical stimuli (Figure 1.1)[13]. The earliest Sensors 1.0 converted physical phenomena into visible mechanical responses such as dial movements or colour changes [14]. Sensors 2.0 introduced electrical outputs and basic control capabilities, enabling integration into analog and early digital systems [15]. Sensors 3.0 advanced further with miniaturization, embedding sensors into portable electronics like smartphones and wearables, and making pervasive sensing a reality [16]. Today, Sensors 4.0 represent a paradigm shift in sensor technology.

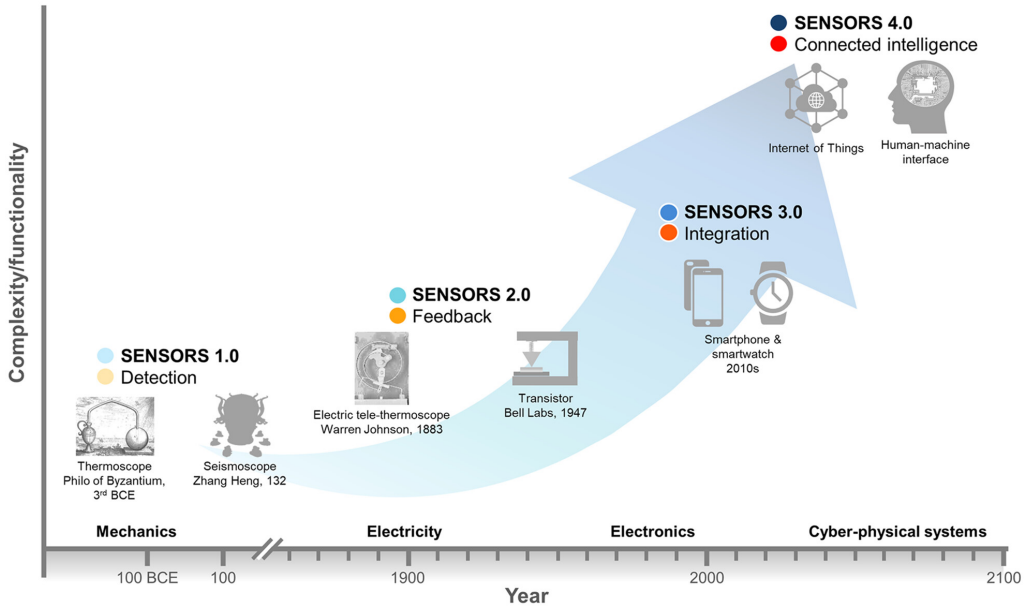


FIGURE 1.1: Evolution of sensor technologies across four generations from mechanical responses (dials, color changes) to electrical outputs, miniaturized devices, and intelligent Sensors 4.0 systems. The shift toward Sensors 4.0 highlights the need for flexible sensors [1].

Sensors function as intelligent, interconnected nodes inside cyber-physical systems. They leverage IoT, AI, and big data analytics to deliver real-time monitoring, predictive diagnostics, and adaptive control [17].

While these digital capabilities are transformative, their practical success depends on reliable physical integration with real environments [18]. Traditional rigid sensors often excel in sensitivity and related performance metrics. They fail to maintain conformal contact, leading to unstable signals and poor long-term reliability [19]. This mismatch between advanced digital systems and limited mechanical adaptability has accelerated the rise of flexible electronics as a solution.

Flexible electronics are devices built on substrates such as polymers or elastomers. These substrates allow devices to bend, stretch, fold, or twist without losing their functionality [20]. Unlike conventional rigid silicon-based electronics, flexible electronic systems adapt to non-planar or moving surfaces. Their mechanical compliance, combined with emerging materials and MEMS-based fabrication techniques,

also offers advantages in lightweight construction, scalability, and cost-effective manufacturing. This makes them ideal for applications in wearables, electronic skin (e-skin), continuous health monitoring, and human–machine interfaces.

In contrast, rigid substrates lose stable contact with non-planar surfaces under repeated deformation. This results in signal drift, user discomfort, or even sensor failure. Flexible sensors fabricated on stretchable, bendable, or foldable substrates overcome these limitations through inherent softness and dynamic form adaptation [19].

The promise of flexible sensors has sparked intense global research and development. This technological momentum is also reflected in market trends. According to Figure 1.2, the flexible sensor market is expected to reach $11.2 billions by 2032, growing at a compound annual growth rate of 7.7 [2]. Among various flexible sensor types, electromechanical sensors occupy a central role. By enabling real-time

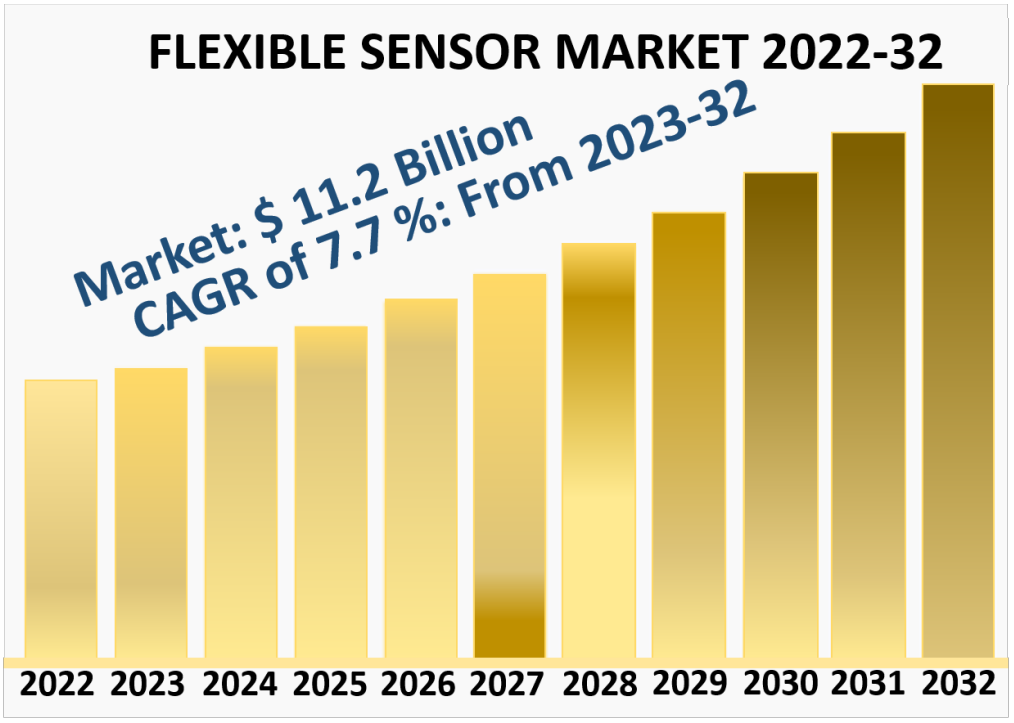


FIGURE 1.2: The marketing prediction of the flexible electronics up to the year 2032 with electromechanical sensors dominating the market [2]

detection of force, touch, and mechanical deformation, they act as building blocks for health monitoring systems, intelligent prosthetics, soft robotics, and interactive platforms. Their combination of adaptability and functionality positions them at the core of Sensors 4.0 [21]. The biological benchmark for such a system is human skin, which is naturally flexible, stretchable, and multi-functional. As illustrated in Figure 1.3, human skin integrates various mechanoreceptors, Merkel cells, Meissner corpuscles, Pacinian corpuscles, and Ruffini endings. Each is specialized for detecting different mechanical stimuli such as static pressure, dynamic pressure, direction, and strain [3]. Additionally, microstructural features like interlocked ridges and fingerprint textures enhance tactile resolution and directional sensitivity. The skin's multimodal and hierarchical functionality inspires the design of flexible electromechanical sensors. These sensors aim to capture both static and dynamic stimuli,

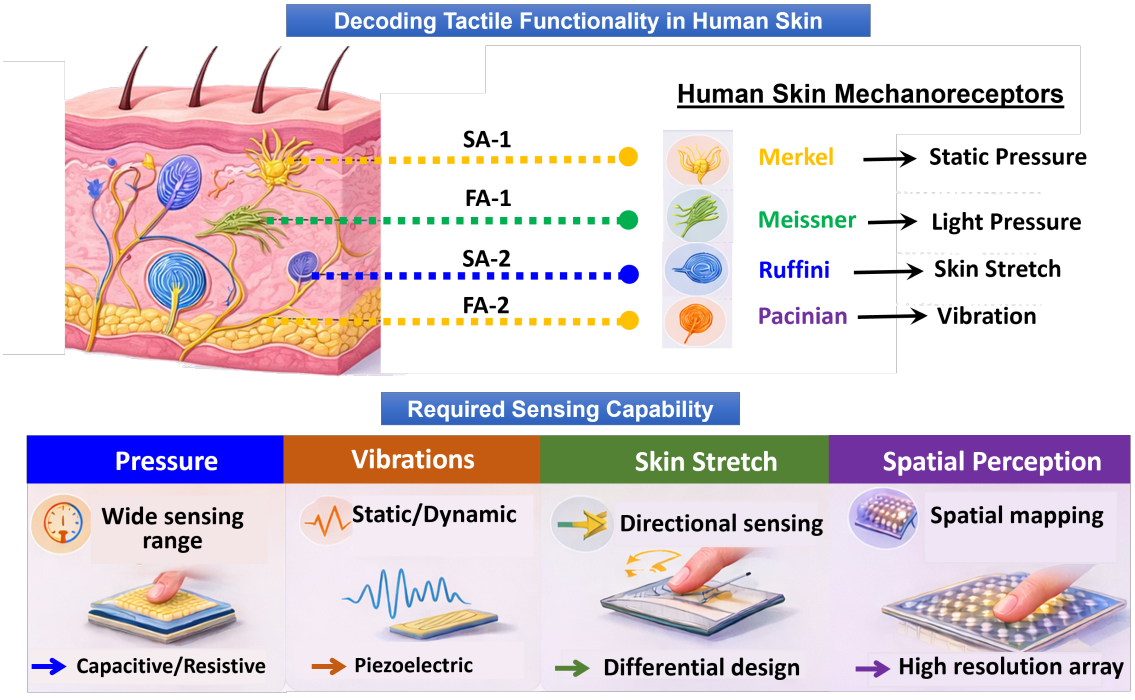


FIGURE 1.3: Structure of human skin showing mechanoreceptors: Merkel (MD) and Ruffini (RE) for static stimuli, Meissner (MC) and Pacinian (PC) for dynamic stimuli, and its capabilities. [3].

resolve directional strains, and cover a wide dynamic range. To translate these skin-inspired functions into practical devices, flexible electromechanical sensors rely on four principal transduction mechanisms: capacitive, piezoresistive, piezoelectric, and triboelectric.

1.2 Transduction Mechanism

Building on the biological inspiration of human skin, flexible electromechanical sensors achieve their functionality through four principal transduction mechanisms: capacitive [22], piezoresistive [23], piezoelectric [24], and triboelectric [25] (Figure 1.4). Every mechanism translates external mechanical stimuli into measurable electrical signals. Each category employs distinct design strategies and functional materials tailored to its specific mode of operation. Additionally, each mode offers particular advantages and faces unique limitations in the context of design.

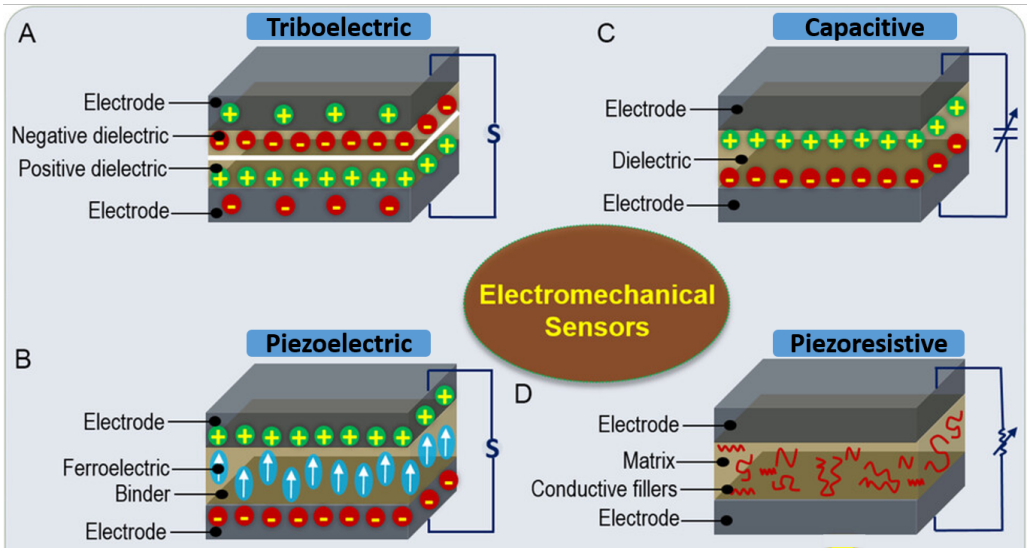


FIGURE 1.4: Transduction mechanisms in flexible electromechanical sensors: (a) Triboelectric, (b) Capacitive, (c) Piezoelectric, and (d) Piezoresistive [4].

1.2.1 Capacitive

Capacitive flexible electromechanical sensors operate by utilizing changes in the dielectric layer or electrodes under applied pressure. The resulting capacitance variation forms the basis for obtaining the capacitance–pressure calibration curve. The sensing mechanism mainly employs two geometries: (i) parallel-plate electrodes with a sandwiched dielectric layer (Figure 1.4 (c)), and (ii) planar interdigitated electrodes with an overlaid dielectric layer. In the parallel-plate configuration, deformation of the dielectric layer alters the distance between the electrodes. This change alters the capacitance, which can be calculated using the following equation:

$$C = \varepsilon_r \varepsilon_0 \left(\frac{A}{d} \right) \tag{1.1}$$

where ε_r is the relative permittivity of the dielectric material, ε_0 is the permittivity of free space, A is the area of the electrodes, and d is the separation distance between the two electrodes [26].

In the interdigitated electrode (IDE) configuration, the capacitance originates from the fringing electric fields between adjacent fingers, and changes in the effective dielectric constant under applied pressure modulate the capacitance. This geometry is particularly advantageous for planar integration. Capacitance depends on electrode design, separation, and the dielectric constant. Researchers have introduced various structural and material innovations. For instance, Luo et al. proposed structural innovations in the dielectric layer [9], while Guo et al. employed a ferroelectric material, P(VDF-TrFE), as the dielectric layer to enhance performance [26]. Capacitive sensors offer advantages such as low power consumption, fast response, and simple design [27]. However, these are susceptible to parasitic capacitance effects and electromagnetic interference, which can impact measurement accuracy [28].

1.2.2 Piezoresistive

Piezoresistive sensors function by changing resistance under applied pressure. This resistance change forms the basis for pressure calibration. These kinds of devices mainly consist of a conductive functional layer positioned between the electrodes or placed on an interdigitated electrode (IDE). The main mechanisms that dominate the resistive response are: (1) the change in resistance between the face-to-face conductive layers or between the electrode and conducting layer, and (2) the conductive layer's own variation in resistance [29]. The resistance of the functional layer follows:

$$R = \rho \frac{L}{A} \tag{1.2}$$

where ρ, L, and A are the specific resistivity, the length, and the cross-sectional area of the material, respectively. This means that resistance changes depend on the material type, its length, and its effective area.

Various strategies have been employed to optimize these geometrical dimensions and improve the performance parameters of flexible electromechanical sensors. For example, Chen et al. increased the length of the functional layer by employing a wavy microfluidic structure [30], while He et al. enhanced the contact area between the electrodes and the functional layer [31]. The piezoresistive mechanism offers a simple readout and a wide dynamic range. However, the response is prone to temperature variations, and signal drift may occur over time.

1.2.3 Piezoelectric

The piezoelectric mechanism is based on the piezoelectric effect to achieve pressure-sensing capabilities. Certain materials with asymmetric crystal structures generate

an electrical charge or voltage when subjected to mechanical stress [32]. When force is applied to the device, it induces polarization within the material. This results in an uneven charge distribution and the accumulation of charges on its surfaces. This charge separation produces an electric potential difference (voltage) across the material. This voltage output is used to establish the voltage–pressure calibration curve. The effect is described by the constitutive equations [33]:

$$S = s^E T + d^t E \tag{1.3}$$

$$D = d\,T + \varepsilon^T E \tag{1.4}$$

where D is the electric displacement (flux density), d is the matrix for the direct piezoelectric effect, T is the stress, ε^T is the permittivity of the medium at constant stress, and E is the electric field strength. The surface charge generated due to the piezoelectric effect can be expressed as [34]:

$$Q = d_{mn}\,F \tag{1.5}$$

where Q is generated charge, d_{mn} is piezoelectric strain coefficient, and F is force. Piezoelectric materials are mainly described by the d_{33} and d_{31} coefficients. The d_{33} coefficient represents forces and charge collection along the same axis as polarization. The d_{31} coefficient describes cases where force is applied along the polarization axis, but charge is collected along a perpendicular axis. Owing to these properties, new opportunities for fabricating piezoelectric-based devices have emerged. For example, Hu et al. used a $BaTiO_3$ /P(VDF-TrFE) composite [35], while Yang et al. modified the previous material by using PDA@BTO/PVDF composite as the piezoelectric material in their device [36]. Although piezoelectric sensors include self-powered operation, they are generally limited to detecting dynamic stimuli only.

1.2.4 Triboelectric

A triboelectric flexible electromechanical sensor measures pressure by exploiting the triboelectric effect. It uses two layers of triboelectric materials with different electronegativities or positions in the triboelectric series, placed in the sensing area. Each layer is connected to separate electrodes [37]. When these layers contact each other, electrons transfer between surfaces due to their differing tendencies to gain or lose electrons. Under applied pressure, the contact area between the two layers changes, leading to the generation and accumulation of triboelectric charges [38]. This charge transfer produces a voltage signal, which quantifies and monitors the applied pressure. Triboelectric nanogenerators (TENGs) utilize this principle in combination with electrostatic induction, enabling self-powered electromechanical sensing [39]. Triboelectric pressure sensors offer several advantages, including a simple device structure, low fabrication cost, and high energy conversion efficiency at low frequencies. However, they face limitations such as performance degradation under long-term cyclic operation, and measure only dynamic pressure signals [25]. While the choice of transduction mechanism defines the fundamental sensing pathway, overall device performance can be further tuned through structural and material innovations. Such design strategies complement mechanical deformation and electrical coupling, enabling enhanced sensitivity, extended range, and application-specific adaptability.

1.3 Structural and Material Innovation

In applications such as human motion monitoring and human-machine interfaces, electromechanical sensing devices are required to combine a wide sensing range, high sensitivity, and crosstalk-free operation [40]. Achieving these performance targets

often requires a combination of material optimization and structural design at the micro and nanoscale [41]. One effective strategy is the micro-engineering of active materials or electrodes. This approach tailors their mechanical and electrical responses to external stimuli [42].

Reported micro-engineering approaches include the formation of micro-pyramids [43], micro-hemispheres [44], micro-pillars [45], micro-porous structures [46], and other patterns like microcracks and random surface roughness [47]. These engineered active materials enhance sensitivity by concentrating stress, improving contact area modulation, and broadening the sensing range. By leveraging such structural innovations, researchers have been able to significantly advance the performance parameters of these flexible electromechanical sensors [4]. Depending on the design, micro-engineering can be implemented directly on the active sensing layers. In terms of material innovations, various strategies complement micro-engineering techniques. These include the use of diverse dielectric materials, functional fillers, multi-material architectures, and tailored composite structures. Such combinations synergistically enhance sensor performance [48].

1.3.1 Structural Micro-engineering

Micro-engineering of the active layer is a widely adopted strategy to improve sensitivity, detection limit, and sensing range. While transduction defines the fundamental sensing pathway, micro-engineering strategies refine the response by tuning deformation and electromechanical coupling. Introducing micro-structured features into the active layer reduces its effective Young's modulus. It also localizes stress concentration and increases the degree of contact area change under load [49]. These effects collectively enhance sensitivity and broaden the sensing range. Furthermore, micro-structuring can reduce the viscoelastic response of the material, improve the

detection limit, and enable faster response times [50]. In resistive-based sensing mechanisms, micro-structuring induces greater changes in the contact area between conductive elements. This results in more pronounced resistance variations [51]. In capacitive-based mechanisms, incorporating air gaps or porous features into the dielectric layer allows greater deformation under applied force, thereby producing larger capacitance changes [52]. These enhancements are achieved through a variety of micro-engineering strategies, each tailored to manipulate mechanical deformation and optimize the resulting electrical response.

Bao *et al.* pioneered the use of micro-engineered structures in capacitive sensors by introducing a micropyramidal dielectric layer [53]. Since then, numerous micro-engineered configurations have been explored, among which the micro-pyramidal geometry has been widely used [54] (Figure 1.5). Following this, Tang *et al.* proposed a design using carbon nanotube (CNT) electrodes combined with a microstructured Ecoflex dielectric layer. This device achieved a sensitivity of 2.51 kPa^{-1}, a response time of 84 ms, and a sensing range below 15 kPa [45]. Similarly, Zhang *et al.* reported an ultra-sensitive piezoresistive device with a sensitivity of 3.26 kPa^{-1} over a detection range of 3 kPa [55]. Pyramidal microstructures offer high sensitivity at low pressures due to localized stress concentration and rapid contact-area expansion. However, they tend to saturate under moderate to high pressures as the contact area is fully engaged. This saturation narrows the usable pressure range.

In addition to pyramidal geometries, micro-hemispherical structures represent another widely used microengineering approach (Figure 1.6). Their geometry allows responsiveness to diverse pressure stimuli, enabling the detection of pressure, shear, bending, and torsional forces. Yang *et al.* [7] developed a hemispherical microstructured capacitive sensor with a sensing range of 10 kPa, high sensitivity (0.382 kPa^{-1}), and a minimum detectable pressure of 4 Pa. In another study [56], hemispherical

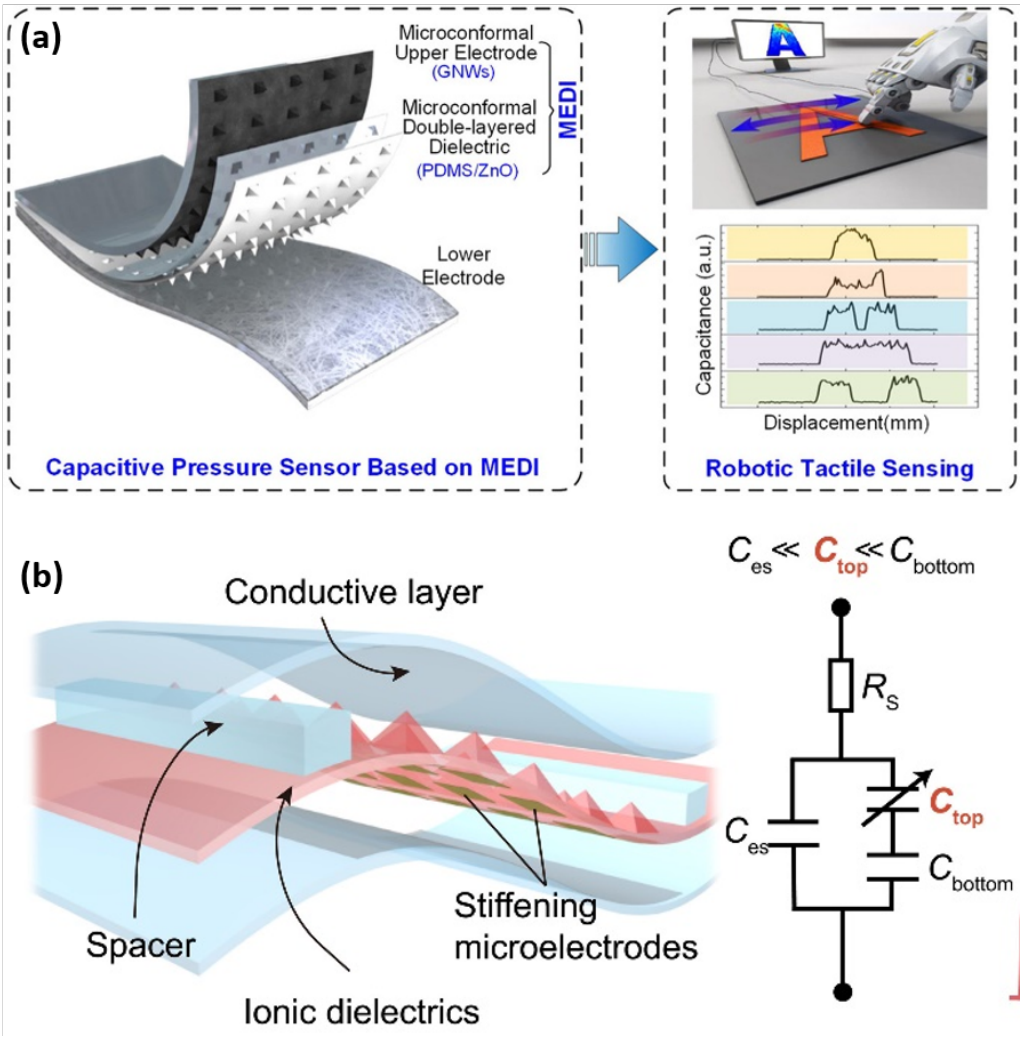


FIGURE 1.5: a) Schematic of a double-sided μ-pyramidal structure, consisting of a PDMS/Zn dielectric layer sandwiched between graphene nanowire (GNW)-based electrodes [5]. (b) 3D schematic of the device with its equivalent circuit, where C_{es} is the inter-electrode capacitance and C_{top} and C_{bottom} are the electrical double-layer (EDL) capacitances of the top and bottom interfaces [6].

shell microstructures in modified nano-ZnO/RTV composites achieved high sensitivity (1.03 kPa^{-1}) and a detection range of 6 kPa. Hemispherical geometries provide smoother contact evolution compared to pyramids, enabling responsiveness across a broader range of stimuli. Nevertheless, their higher fabrication complexity and smaller initial contact area may limit low-pressure sensitivity compared to pyramidal structures.

Porous micro-structured functional layers provide an alternative strategy. They

provide a wide linear sensing range by concentrating stress within the structural framework (Figure 1.7). The microporous design permits significant elastic deformation under pressure and supports a rapid fabrication process [52]. However, high porosity can compromise mechanical durability and make the device more susceptible to environmental factors such as moisture and dust. Wan et al. introduced the graphene foam (GO) as a porous dielectric between the graphene-based electrodes. The device showed a sensitivity of 0.8 kPa^{-1} and a time response of 100 ms, but a sensing range of up to 4 kPa [8]. In another study, a sponge-like PDMS-based

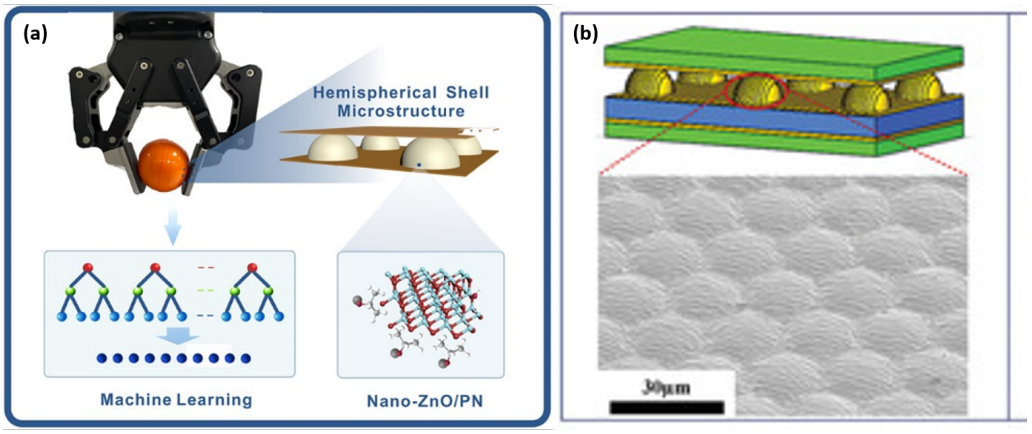


FIGURE 1.6: (a) Schematic illustrating the double-sided micro-pyramidal structure. The device consists of a PDMS/Zn dielectric layer sandwiched between graphene nanowire (GNWs)-based electrodes [5]. (b) Schematic illustrating a fully packaged device with μ-spherical micro-engineered dielectric layer and its SEM image [7].

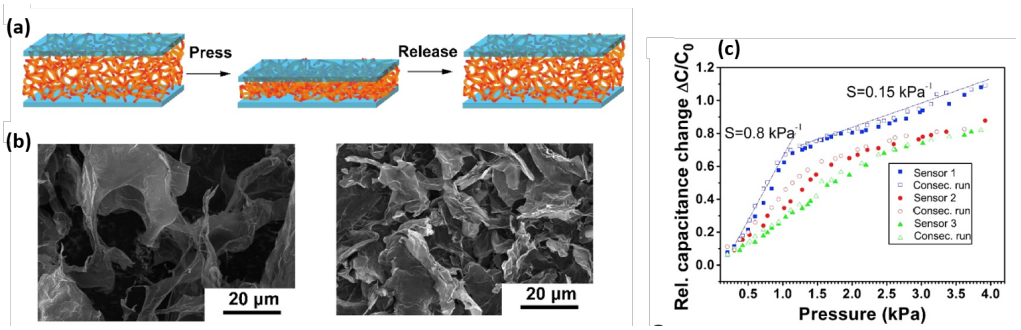


FIGURE 1.7: (a) Device concept of the graphene oxide (GO) foam-based pressure sensor. (b) SEM images showing the porous network structure. (c) Relative capacitance change as a function of pressure [8].

sensor demonstrated a sensitivity (0.078 Pa $^{-1}$) and a limited sensing range, making it best suited for applications requiring small, precise pressure detection.

Other micro-engineering strategies include micro-pillar-based, microcrack-based, and diverse micro-patterned architectures. For example, Liao *et al.* demonstrated an interlocked micro-pillar structure of PDMS with secondary nano-protrusions, achieving a wide linear range (0-32 kPa), high piezoresistive sensitivity (26.08 Ω/kPa), and a fast relaxation time of 140 ms [57] (Figure 1.8). Collectively, these examples highlight the versatility of micro-engineering approaches in tailoring the mechanical and electrical response of flexible tactile sensors. At the same time, they expose inherent trade-offs between sensitivity and sensing range that cannot be fully resolved through structural design alone.

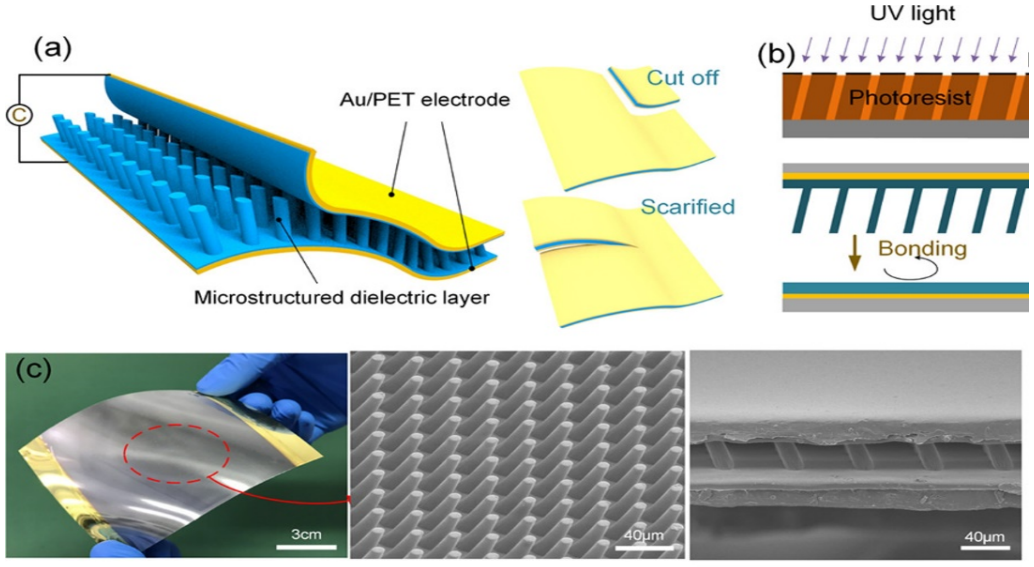


FIGURE 1.8: (a) Schematic illustrations of the micropillar-based capacitive electromechanical sensor. (b) Fabrication process of the device. (c) Optical image and the SEM image of the fabricated device [9]

1.3.2 Material Innovations

Micro-engineering alone is not sufficient to improve the overall performance parameters for flexible electromechanical sensors. Therefore, the optimal strategy often involves a co-engineered approach. In this approach, structural features and tailored material systems work synergistically to overcome limitations of each individual component [58]. Material innovations complement micro-engineered designs by providing enhanced dielectric, conductive, or piezoelectric properties. Although micro-engineering can enhance device sensitivity, early saturation of the contact area or dielectric layer often limits the sensing range [28]. Therefore, selecting an appropriate material configuration for both the functional materials and the substrates is essential.

In flexible electromechanical sensors, the materials typically consist of two main components: the substrate and the functional material [59]. Flexible substrates provide the necessary flexibility and stretchability. The functional materials are responsible for converting mechanical stimuli into electrical signals. Both components must exhibit good chemical stability, appropriate conductivity, desirable mechanical properties, and compatibility with MEMS-based fabrication of high-resolution and high-density sensing arrays [60].

Commonly used flexible substrates include polydimethylsiloxane (PDMS), polyethylene terephthalate (PET), polyimide (PI), polyurethane (PU), and certain hydrogels. PDMS offers optical transparency, high thermal stability, biocompatibility, and excellent flexibility. It also serves as an ideal polymer matrix for incorporating functional fillers such as magnetic nanoparticles, piezoelectric nanoparticles, or metallic nanoparticles [61]. PDMS is generally not ideal as a substrate for electrode fabrication, especially with metals like gold, because it exhibits loose and weak adhesion to metallic films, leading to poor mechanical reliability and cracking under stress or

after repeated use. PET and PI, in contrast, are particularly suitable for fabricating electrodes due to their compatibility with MEMS-based processes. Polyethylene terephthalate (PET) is a polyester with high tensile strength, stiffness, and excellent chemical resistance, along with transparency and ease of processing into flexible films [62]. PET sheets, however, cannot sustain high temperatures due to their low glass transition threshold and softening behavior, making them unsuitable for high thermal fabrication processes. In contrast, Polyimide (PI) is a high-performance polymer with outstanding thermal stability, mechanical strength and is ideal for MEMS fabrication [63].

While substrates provide the structural foundation, functional materials govern the sensing principle and strongly influence the sensitivity, range, and long-term stability [40]. Material engineering explores the use of different materials like carbon-based [64], conductive polymers [65], piezoelectric nanoparticles [32], and nanofillers [66]. Carbon nanomaterials, including graphene, carbon nanotubes (CNTs), and carbon nanocoils (CNCs), offer exceptional chemical stability, conductivity, and mechanical flexibility, making them suitable for flexible pressure sensor applications [67] (Figure 1.9). Laser-induced graphene (LIG) is particularly promising due to its

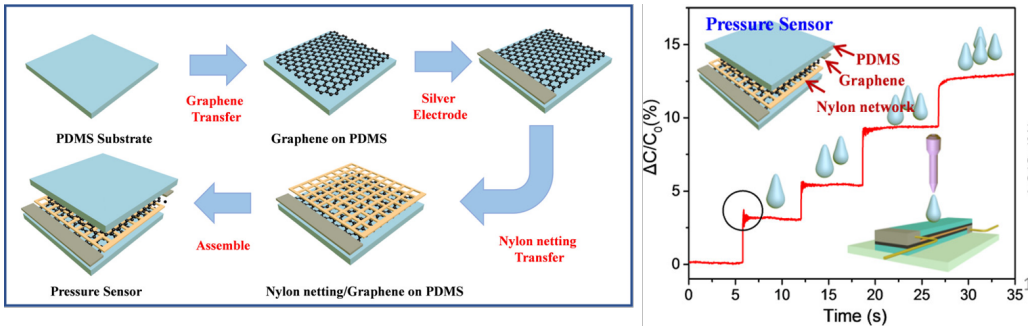


FIGURE 1.9: Fabrication steps of the sandwich-like pressure sensor based on low-cost nylon netting with numerous microsized square holes [10].

single-step patternability, interconnected porous network with meso- and macropores, and excellent adhesion to PDMS substrates. It also enables direct coating of

other materials on PDMS without any surface modification [68]. This makes LIG an excellent 3D scaffold for multilayer architectures often combined with conductive polymers to boost sensing performance [69].

Conductive polymers such as polyaniline (PANI), poly(3,4-ethylenedioxythiophene) (PEDOT), and polypyrrole (PPy) are widely investigated for their high electrical conductivity and mechanical compliance with elastomeric substrates [70]. PEDOT: PSS, notably,offers high stability, good optical transmittance, and conductivities exceeding 3100 S cm^{-1} at 0% strain [71]. Another important class of functional materials is piezoelectric nanoparticles, which offer direct electromechanical conversion capabilities. Piezoelectric fillers such as lead zirconate titanate (PZT), zinc oxide (ZnO), and barium titanate ($BaTiO_3$) have been widely embedded in PDMS matrices to develop flexible piezoelectric electromechanical sensors [72]. Although PZT offers high piezoelectric constants and thermal stability, its lack of biocompatibility due to lead content has accelerated the adoption of lead-free ceramics. $BaTiO_3$ stands out with a d_{33} coefficient exceeding 200 pC/N, a high dielectric constant (100–11,000), and biocompatibility, making it an excellent candidate for integration into soft polymer matrices to fabricate wearable piezoelectric sensors [73].

Nanofillers are also incorporated into polymer matrices to enhance the electromechanical response of sensors [74]. Metallic nanofillers such as silver, gold, copper, and nickel nanoparticles or nanowires provide high electrical conductivity and mechanical compliance [66] (Figure 1.10). However, dielectric nanofillers like Fe_3O_4 nanoparticles stand out due to their high permittivity, low toxicity, and environmental safety [75]. These advantages allow Fe_3O_4-based nanocomposites to achieve superior dielectric performance. While these material and structural innovations have significantly improved sensitivity and tailored sensor responses, many reported designs still face trade-offs between sensitivity, sensing range, and stability. Unimodal devices combined with tailored materials find it hard to achieve high sensitivity, a

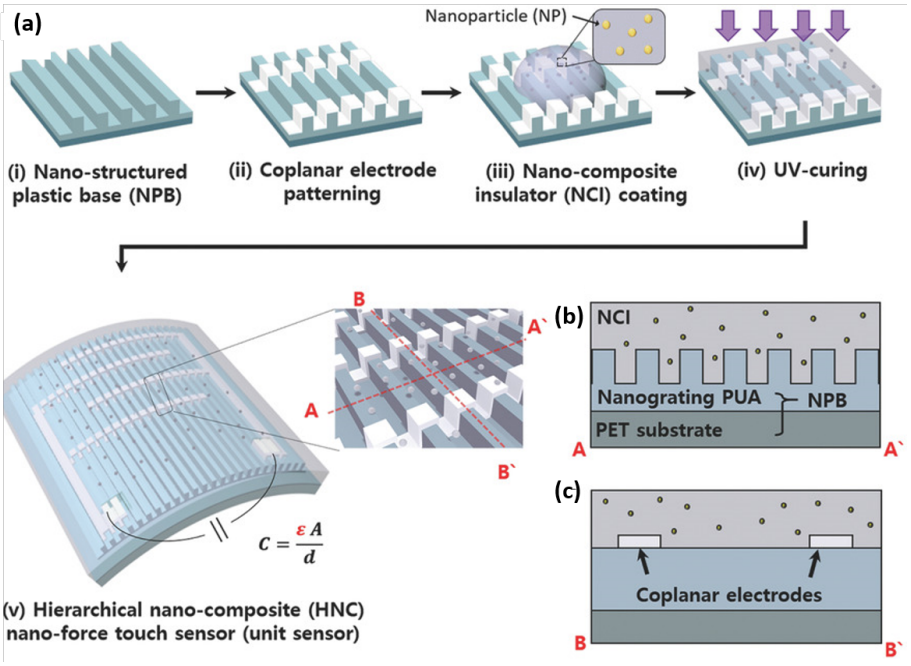


FIGURE 1.10: a) Schematic of the fabrication process for a metal nanofiller-based pressure sensor. (b) Cross-sectional view showing nanogratings filled with metal nanofillers. (c) Exploded schematic highlighting the two coplanar electrodes that enable pressure sensing [11].

wide pressure range, and complete crosstalk suppression. Multi-material layered and hybrid architectures, especially those combining multiple transduction mechanisms, promise to overcome these limitations. These systems integrate micro-engineered dielectric and functional layers to extend the sensing range and enable multimodal signal detection. Additionally, they enhance sensitivity across both low- and high-pressure regimes. In addition, when devices are scaled into arrays, mechanical and electrical crosstalk between adjacent pixels degrades resolution and compromises reliable signal acquisition This observation motivates a focus on integrating different transduction principles within unified architectures to address persistent limitations in next-generation electromechanical sensors. However, even with optimized structures and materials, practical deployment also depends on system-level integration of circuits, power, and communication.

1.4 System Level Integration

For sensors to operate in real-world scenarios, integration into complete systems that manage signal conditioning, processing, transmission, and power is essential. Without such integration, even high-performance devices cannot transition from laboratory demonstrations to practical applications. A complete sensing system typically consists of electromechanical sensors, analog front-end (AFE) circuitry, data processing, transmission, and power management, as shown in Figure 1.11. The integration of these components ensures dependable data acquisition, processing, and communication. Beyond sensor fabrication, system design must address efficient data handling, low-power operation, and seamless wireless integration. The development of optimized algorithms is equally important, contributing to power savings and effective control of the sensing and communication process [76]. While materials and structures define the intrinsic sensing performance, system-level integration

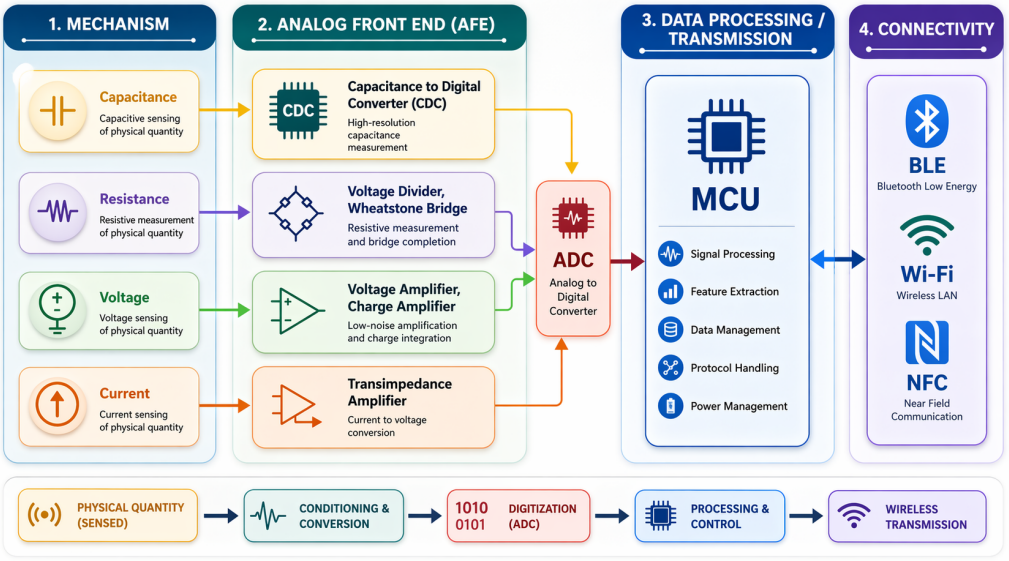


FIGURE 1.11: Schematic illustrating the different components of the integrated system. The sensors collect the data, AFE filters and converts the signals into MCU-readable signals, MCU processes the data, controls the flow of data and sends it for transmission via BLE/WiFi/NFC.

determines whether a device can operate reliably in real-world, continuous-use scenarios.

The AFE plays a critical role in conditioning the raw output of the sensor (voltage spikes, resistance changes, or capacitance variations) into signals readable by the microcontroller unit (MCU). The design of the AFE depends on the sensing mechanism. For resistive sensors, the change in resistance is typically converted to voltage using methods such as voltage dividers, wheatstone bridges [77], time-domain readout [78], or direct resistor-to-MCU interfaces [79]. Voltage dividers are the simplest and most compact solution, while Wheatstone bridges improve measurement accuracy for small resistance changes. In some cases, low-power MCUs with built-in ADCs can directly read these voltages.

Capacitive sensors require capacitance-to-digital converters (CDCs), because most MCUs cannot measure capacitance directly. Commercial Off-The-Shelf (COTS) CDCs like AD7746 (Analog Devices) and FDC1004 (Texas Instruments) provide high resolution (down to 1 fF), I²C communication, and strong noise immunity. These features make them practical for system integration [80]. For piezoelectric sensors, AFEs are essential for signal amplification and conditioning, impedance matching, and noise filtering. COTS solutions such as the PGA309 and OPA145 (Texas Instruments), AD8221 (Analog Devices), and MCP6V01 (Microchip) are widely used for these purposes.

The MCU acts as the system's brain, acquiring data from the AFE, performing calibration, managing data flow, and controlling communication. In addition to basic signal processing, the MCU can implement edge computing techniques such as TinyML to perform on-device inference, reducing latency and enabling autonomous decision-making When processing demands exceed the MCU's capabilities, raw or pre-processed data can be transmitted to an external device (e.g., smartphone or server) for analysis. For wireless data transfer, Bluetooth Low Energy (BLE) is

a common choice due to its favorable balance between power efficiency and data rate (1–2 Mbps) [81]. Many BLE modules integrate MCUs, ADCs, and memory in a single package, reducing system footprint and simplifying design. In applications demanding higher data throughput or longer communication range, Wi-Fi provides greater data rates (tens to hundreds of Mbps) and seamless integration with local networks or cloud systems. However, Wi-Fi's higher power consumption demands careful duty cycle or event-driven transmission to remain feasible for battery-operated devices [82].

The last important component for these systems is the power management module. Power management module guarantees reliable working and extended runtime for the whole system. The most common power source is the lithium-polymer (Li-Po) battery [83, 84]. These batteries are favored for their lightweight design, high specific energy, and compact form factor compared to lithium-ion [85] or coin-cell batteries [86]. Regardless of the battery type, a voltage regulator, typically a low-dropout regulator (LDO), is employed to maintain a stable supply to sensors, readout circuits, MCUs, and communication modules. LDOs are advantageous due to their low voltage drop, minimal quiescent current, and reduced component count compared to switching regulators. In cases where the battery voltage is lower than the system's requirements, a boost converter is used. Alternative power sources include NFC and energy harvesters, but these often supply low average currents (nanoamperes), necessitating energy storage elements like supercapacitors or rechargeable microbatteries for sustained operation [87].

Once power and communication strategies are defined, the next critical consideration is how to physically integrate all components into a mechanically robust and flexible form factor. One approach is the development of fully organic systems, where organic semiconductors (e.g., pentacene, DNTT, PBTI, etc.) are fabricated directly on flexible substrates [88, 89, 90]. However, these devices currently suffer

from lower charge carrier mobility and larger feature sizes compared to silicon, limiting integration density and increasing power consumption [91, 76]. Consequently, silicon-based ICs dominate modern flexible sensor systems due to their superior performance and scalability. This has given rise to flexible hybrid electronics (FHE), where surface-mount devices (SMDs) such as AFEs, MCUs, antennas, and power management chips are mounted on flexible polyimide (PI) substrates with copper interconnects.

Traditional rigid PCBs, which are made from FR4 and copper interconnects, are being replaced by flexible printed circuit boards (fPCBs) that use PI and copper. fPCBs provide superior conformability, reduced weight, thin profiles, and better mechanical durability, especially important in wearable systems (Figure 1.12). PI films

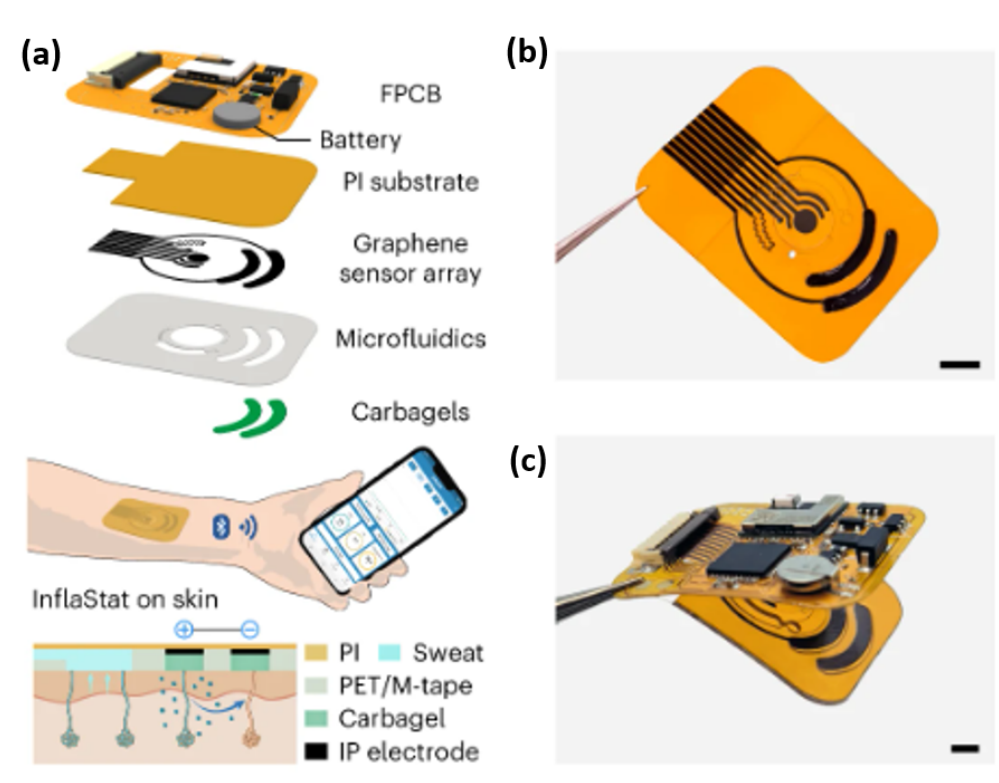


FIGURE 1.12: Integrated system schematic of a skin-interfaced wearable biosensor for monitoring sweat biomarkers, including CRP, pH, temperature, and ionic strength [12].

of varying thicknesses are commercially available or can be customized by processing

methods like spin coating [92]. FHE enables conformal contact with target surfaces (e.g., human skin), improving mechanical coupling and signal fidelity. Leveraging mature CMOS technology, these systems deliver high-precision analog-to-digital conversion, fast data processing, and robust wireless connectivity.

Advances in transduction mechanisms, structural designs, and material innovations have expanded the performance of flexible tactile sensors. Yet, current devices still struggle to combine multilayer integration, hybrid transduction, and multimodal sensing in a deployable form. System-level barriers such as readout electronics, wireless communication, and power management also remain unresolved. The next generation of flexible electromechanical platforms will therefore depend on coupling these device-level innovations with flexible PCB-based integration, enabling scalable and reliable systems.

1.5 Rationale and Objective

The review of the current state-of-the-art reveals several persistent challenges that motivate the present work. Despite significant progress in flexible electromechanical sensors, many devices face a fundamental trade-off between high sensitivity and a wide sensing range. Furthermore, the ability to detect multiple types of mechanical stimuli, such as both static and dynamic pressure, or to discern the direction of strain, remains a challenge for conventional unimodal sensors. In addition, when devices are scaled into arrays, mechanical and electrical crosstalk between adjacent pixels degrades resolution and compromises reliable signal acquisition. Finally, the transition from high-performing discrete sensing elements to fully integrated, application-ready systems with robust readout circuitry remains a critical yet non-trivial step.

To address these challenges, the present thesis develops flexible electromechanical sensor platforms that integrate hybrid, multimodal, and direction-sensitive mechanisms. In addition, system-level circuit integration is implemented to enable application-ready devices suited for human motion monitoring, robotic gripping, and human–machine interaction. The objectives in the broader sense are as follows:

- Design and fabrication of a hybrid capacitive-resistive tactile sensor, enabling dual-mode force detection across low and high-pressure regimes.
- Development of asymmetric and magneto-dielectric strain sensors, capable of detecting directional strain sensing.
- Realization of a multimodal tactile sensor for capturing both static and dynamic pressures using capacitive and piezoelectric sensing modes.
- Implementation of a high-resolution sub-mm capacitive sensor array for surface texture detection.
- Development of interfacing circuits using flexible PCBs for integrated and standalone sensing systems.
- Validation of integrated sensor systems in practical scenarios, including human motion monitoring and HMIs.

1.6 Thesis Organization

The thesis is organized into six chapters. Chapter 1 provides an introduction to the evolution of sensor technologies and the motivation for flexible electromechanical sensors in the context of Sensors 4.0. Thereafter, the fundamentals of electromechanical transduction principles are outlined, followed by a review of state-of-the-art

devices categorized according to their underlying mechanisms and structural design strategies. Different approaches for system-level integration are also introduced. Finally, the objectives and scope of the present research are presented at the end of this chapter.

Chapter 2 addresses the challenge of achieving both a wide sensing range and high sensitivity, which is difficult with conventional single-mode devices. To overcome this, a hybrid capacitive–resistive electromechanical sensor is developed, combining two transduction mechanisms within a multilayered design. This architecture achieves an extended dynamic range while enhancing sensitivity, with a key novelty being the crosstalk-free pixel layout that ensures reliable operation in array configurations. The sensor is integrated with flexible PCB electronics, and its performance is validated in real-time applications, including a Mario-style human–machine interface and a multipressure authentication system.

Chapter 3 tackles the limitations of conventional strain sensors that can only measure deformation magnitude. The first device introduced here is an asymmetric strain sensor, which leverages structural anisotropy to resolve strain direction. The second device, a magneto-dielectric-based sensor, incorporates magnetic nanoparticles in a polymer matrix to realize bimodal functionality, enabling both strain and proximity sensing. This dual capability adds new modalities to sensor platforms by distinguishing contact and non-contact interactions. The electromechanical behavior of both devices is analyzed, and their unique capabilities are demonstrated through human motion monitoring experiments.

Up to this point, the thesis has focused on hybrid and asymmetric designs to broaden sensing functionality. Chapter 4 extends this direction by presenting two devices that address the need for simultaneous detection of static and dynamic pressures. The first is a poroelastic piezoelectric sensor based on a BTO/PDMS composite, fabricated through an eco-friendly, acid-free process that departs from conventional

microfabrication routes. This sustainable approach aligns with the growing demand for environmentally responsible electronics, while the porous architecture enhances compressibility and sensitivity. The second device combines capacitive and piezoelectric transduction in a single platform, overcoming the narrow sensing ranges of microstructured devices. In addition, the combined transduction mechanism enables devices to perceive both static and dynamic signals. The working principles, fabrication, and characterization of both devices are presented, and their performance is validated in robotic gripping experiments, where multimodal response enables adaptive and intelligent control.

Chapter 5 addresses the challenge of scaling from individual devices to high-density integrated platforms. It presents the design and realization of a capacitive tactile array consisting of 64 $\times$ 64 pixels with sub-mm pitch. The fabrication process and flexible circuit strategies for large-scale pixel addressing are discussed, along with methods for minimizing parasitic coupling and measurement noise. This transition from device-level sensing to high-resolution, application-ready arrays enables fine surface texture mapping and high-density tactile imaging. Experimental validation demonstrates the potential of this approach for next-generation robotic and human–machine interface systems.

Finally, Chapter 6 summarizes the key contributions of the thesis, emphasizing the novelty of combining hybrid, asymmetric, multimodal, and high-resolution tactile devices into a unified framework. The chapter concludes with perspectives on future research directions in flexible hybrid electronics and their applications in intelligent sensing platforms.

Chapter 2

Flexible Suspended Hybrid Tactile Sensor with Crosstalk-Free Design for Human–Machine Interfaces

This chapter presents a suspended hybrid tactile sensor for broad-range pressure sensing. The design combines capacitive and piezoresistive mechanisms to leverage their complementary sensing ranges, thereby enhancing overall sensitivity. To suppress crosstalk, a dual-isolation strategy is introduced, utilizing SU-8 pixel spacers for mechanical isolation and a fully parallel, per-channel ADC readout for electrical isolation. The sensor's performance is quantitatively evaluated in terms of sensitivity and sensing range. Finally, system-level validation is demonstrated through its integration with a flexible PCB for wireless data acquisition in Human-Machine Interfaces (HMIs).

2.1 Introduction

Over the last decade, flexible electromechanical sensors garnered significant attention due to their applications in human health monitoring, human–machine interfaces, and intelligent prosthetics [93, 94]. To meet these requirements, devices must exhibit high sensitivity over a broad sensing range [1],[95], and low crosstalk when in an array for reliable operation. However, most devices face a trade-off between sensitivity and sensing range [96].

Structural microengineering approaches such as micro-pyramids, porous architectures, and other geometries significantly improved sensitivity by amplifying deformation. However, these often exhibit a limited sensing range due to early saturation of the contact area [97]. In addition, weak interfacial adhesion between the sensing layer and the electrode leads to delamination [98]. On the material side, conductive nanomaterials, including graphene [99],carbon nanotubes [100], silver nanowires [101], and conductive polymers like poly(3,4-ethylenedioxythiophene) (PEDOT), have been integrated into polymer matrices to enhance conductivity and compliance. Yet these approaches remain confined to narrow operating windows. To overcome these limitations, hybrid devices that combine multiple transduction mechanisms have recently emerged. By integrating capacitive and resistive responses in a single platform, hybrid designs offer the potential to unify high sensitivity with a wide sensing range. Nevertheless, reported hybrid devices have not fully addressed critical system-level issues, particularly crosstalk, which arises from both mechanical coupling between pixels and electrical interference in shared row–column circuits [102]. Prior strategies for crosstalk suppression have typically been partial, relying either on rigid spacers to reduce mechanical coupling or on patterned functional layers to confine electrical pathways [96]. However, none have employed a combined approach

that integrates spacers, patterned functional materials, and dedicated ADC channels. As a result, residual crosstalk continues to degrade resolution and accuracy in large-area arrays, limiting their practical utility.

In this chapter, we introduce a suspended hybrid tactile sensor designed to overcome key limitations in existing designs. The novelty lies first in the hybrid architecture itself, which integrates capacitive and resistive mechanisms within a single device to overcome the inherent sensitivity–range trade-off. In addition, the device employs a multilayer structure based on laser-induced graphene (LIG) and PEDOT:PSS, enabling robust transduction and facile integration. Finally, a crosstalk suppression strategy is implemented through mechanical isolation using SU-8 spacers and electrical isolation via a fully parallel, per-channel ADC readout. Together, these innovations establish a scalable and reliable tactile platform. The proposed architecture is validated through detailed electrical and mechanical characterization. Furthermore, its practical utility is demonstrated in application-level interfaces, including a Mario-style interactive game and a secure multi-level pressure authentication system. Consequently, this chapter presents the first hybrid, multilayer, and crosstalk-free tactile platform for high-resolution and scalable human–machine interfaces.

2.2 Device Concept and Design

Figure 2.1(a–d) illustrates the schematic concept and sensing mechanism of the hybrid device. The device primarily consists of three parts: (i) a spiral interdigitated electrode (IDE) fabricated on a polyimide substrate, (ii) a circular-patterned SU-8 cavity that defines the air gap, and (iii) the suspended membrane. The suspended membrane is a tri-layer structure comprising PEDOT:PSS coated over laser-induced graphene (LIG), which is in turn supported on a PDMS substrate. To estimate

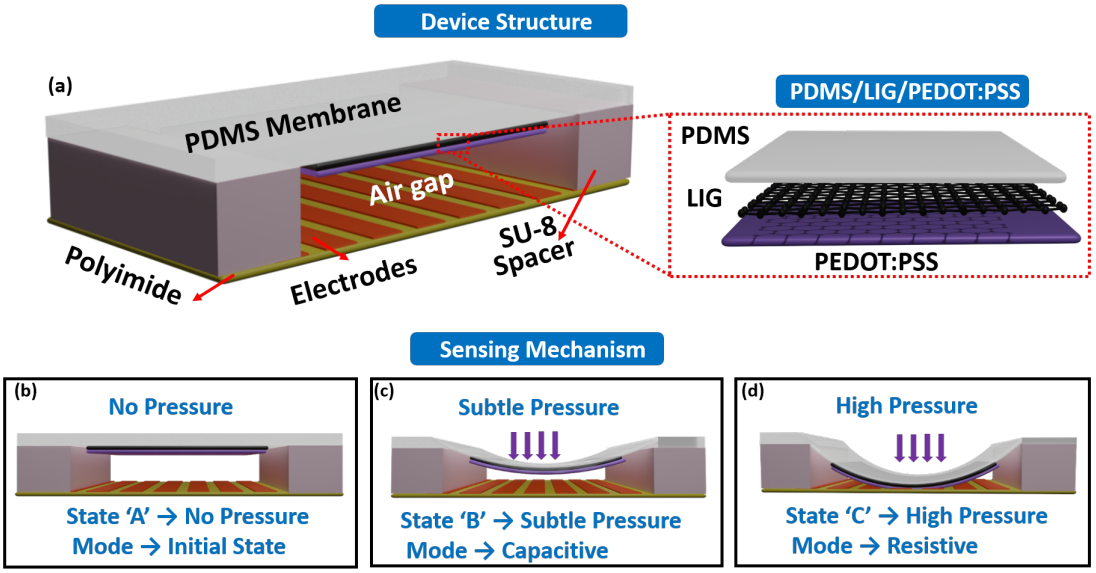


FIGURE 2.1: (a) Schematic of the hybrid tactile sensor consisting of a suspended PEDOT:PSS/LIG/PDMS membrane positioned above interdigitated electrodes (IDEs), separated by an SU-8-defined air gap. The electrodes appear as parallel strips due to the sectional representation of the spiral geometry. (b–d) Sensing mechanism under different pressure regimes: (b) Initial state with no pressure; (c) Capacitive mode under subtle pressure, where membrane deflection alters the capacitance; (d) Resistive mode under high pressure, where the sensing layer contacts the IDE.

the capacitance of the spiral IDE with the suspended membrane, the geometry is approximated as a pair of concentric ring electrodes with alternating polarity [103]. This approximation captures the radial symmetry and dominant fringe field distribution between adjacent spiral turns. The fringe capacitance between a single inner and outer ring electrode is given by the following expression [103]:

$$C_f = 4R_1\varepsilon_0\varepsilon_{\text{eff}}(\rho_1+\rho_g)\sum_{n=1}^{\infty}\frac{I_1(n\rho_1)}{I_1(n\rho_2)}\Big\{I_1(n\rho_2)K_1[n(\rho_1+\rho_g)-I_1[n(\rho_1+\rho_g)]K_1(n\rho_2)\Big\} \tag{2.1}$$

where the dimensionless parameters are defined as:

$$\rho_1 = \frac{\pi R_1}{d}, \quad \rho_2 = \frac{\pi R_2}{d}, \quad \rho_g = \frac{\pi g}{d} \tag{2.2}$$

Here, R_1 and R_2 denote the inner and outer radii of the spiral loop, respectively, g is the inter-electrode spacing, and d is the vertical separation between the electrode plane and the opposing surface. I_1 and K_1 are the modified Bessel functions of the first and second kind. ε_0 is the vacuum permittivity, and ε_{eff} is the effective relative permittivity accounting for the tri-layer dielectric stack. From the equation, the capacitance is defined by geometric parameters R_1 and R_2, g, effective electrode length $\pi(R_1 + R_2)$, and the effective relative permittivity ε_{eff}. The rationale for using a spiral IDE is its significantly greater effective electrode length compared to a planar IDE occupying the same footprint, which results in enhanced sensitivity [103]. Since the electric field lines emerging from the spiral IDE extend vertically into a multilayered dielectric stack composed of air, PEDOT:PSS, LIG, and PDMS, the total fringe capacitance is influenced not only by geometry but also by the permittivity and thickness of each dielectric layer. To incorporate this effect analytically, the partial capacitance method is employed. The detailed analytical formulation and derivation of the effective permittivity using this method are provided in Appendix B. This approach, originally formulated for coplanar waveguides, decomposes the multilayer dielectric region into a series of equivalent single-layer structures [104] (Figure 2.2). Since the device has the fixed geometrical parameters like R_1 and R_2, the capacitance is dominated by the ε_{eff} which is modulated by the air gap according to the following equation:

$$\begin{aligned} \varepsilon_{\text{eff}} &= \varepsilon_0 + \varepsilon_1 q_1 + \varepsilon_2 q_2 + \varepsilon_3 q_3 + \varepsilon_4 q_4 \\ &= \varepsilon_{\text{env}} + (\varepsilon_1 - \varepsilon_{\text{env}}) q_1 + (\varepsilon_2 - \varepsilon_1) q_2 + \\ &(\varepsilon_3 - \varepsilon_2) q_3 + (\varepsilon_4 - \varepsilon_3) q_4 \end{aligned} \tag{2.3}$$

The detailed analysis In the initial state, when no external force is applied, the electric field lines are symmetrically distributed between the electrodes (State A). This

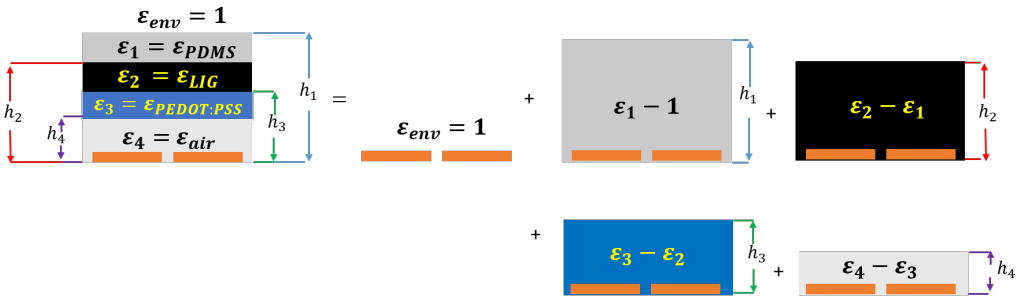


FIGURE 2.2: Partial capacitance model showing decomposition of effective permittivity across the multilayer dielectric stack: environment, PDMS, LIG, PEDOT:PSS, and air gap.

results in a baseline capacitance 'C_0'. Upon application of some force, the suspended PEDOT:PSS/LIG/PDMS membrane deforms, reducing the gap between the sensing layer and the electrodes. This deformation alters the effective dielectric constant (ε_{eff}) around the IDEs, thereby changing the capacitance. At this stage (State B), there is no direct contact with the IDEs, and the device operates in capacitive mode. As the applied force increases further, the tri-stack sensing layer comes into contact with the electrodes, leading to a transition into resistive mode due to the formation of conductive pathways (State D). This transition is marked by a simultaneous increase in conductance and a fall in measured capacitance. The conductive bridges partially short the fringing electric fields, reducing the apparent capacitive contribution, while creating low-resistance pathways for charge transport. Independent I–V characterization confirms the transition, exhibiting a linear current–voltage relationship (–2 V to +2 V) that evidences the formation of an ohmic conduction path. With increasing pressure, the current magnitude rises steadily, consistent with progressive expansion of the contact area and the development of multiple conductive bridges. In this regime, the device operates as a pressure-dependent resistor, with its resistance following a power-law relationship:

$$R(P) \propto P^{-m} \tag{2.4}$$

This synergistic dual-mode mechanism enables the detection of both light and heavy pressures.

The materials used in the present device are selected based on electrical performance, mechanical compliance, and fabrication scalability. Laser-induced graphene (LIG) serves as a mechanically flexible conductive scaffold that can be directly patterned on polyimide using CO laser irradiation through a single-step mask-free process. This approach eliminates vacuum deposition or multistep lithography, enabling rapid and scalable fabrication. The porous morphology of LIG provides a large surface area that facilitates strong mechanical interlocking with PDMS and serves as an effective anchoring scaffold for conductive coatings. PEDOT:PSS is incorporated to enhance electrical conductivity and interfacial charge transport, thereby improving the capacitive modulation when the membrane approaches the electrodes. PDMS is used as the elastomeric support layer due to its flexibility, chemical stability, and compatibility with flexible electronics. Together, the PEDOT:PSS/LIG/PDMS multilayer structure provides a mechanically robust and highly sensitive tactile sensor.

2.3 Fabrication Process Flow

Figure 2.3 shows the fabrication process flow of the device. It involves three major steps: electrode patterning and cavity formation, tri-layer membrane fabrication, and final device integration. First, interdigitated electrodes (IDEs) are patterned on a flexible polyimide (PI) substrate (Figure 2.3(1a-c)). A thin layer of Cr/Au (10 nm/60 nm) is deposited using an e-beam evaporator (EBE ATS-500), followed by photolithographic patterning to define the electrode layout (Figure 2.3(1c)). A uniform SU-8 3010 layer is then spin-coated and patterned to form microcavities. SU-8 3010 is prepared by diluting SU-8 3050 (MicroChem) with SU-8 3000 thinner

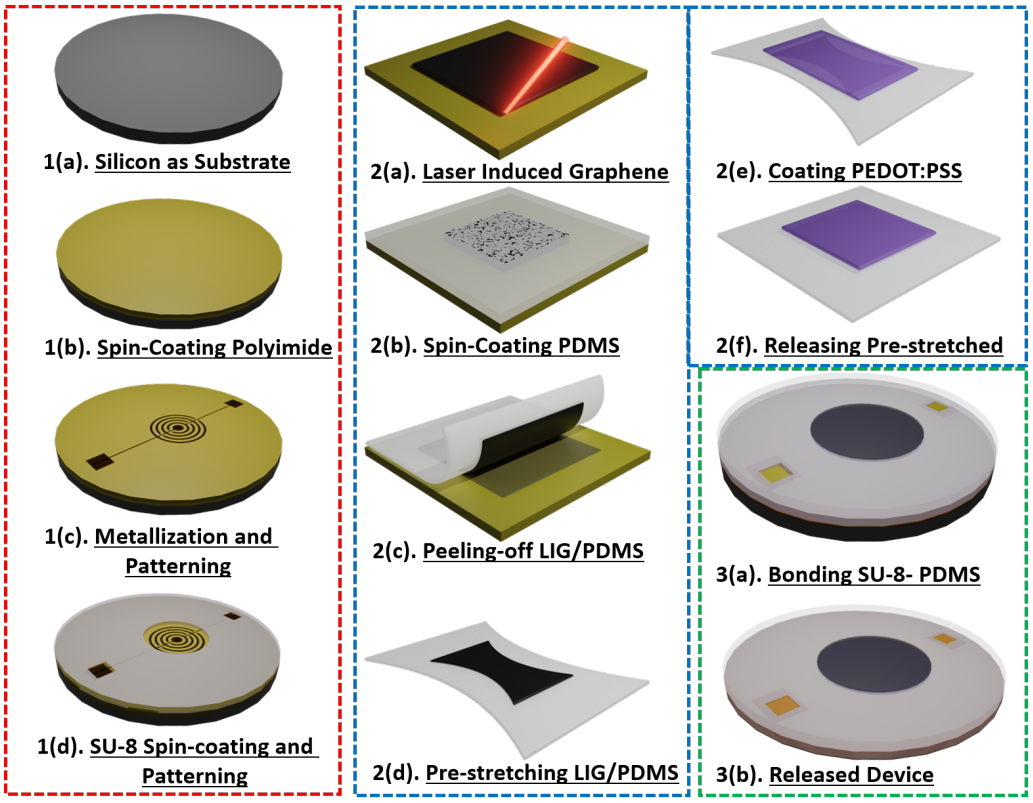


FIGURE 2.3: Schematic of the fabrication process flow: (1) Electrode patterning with SU-8 cavity formation, (2) Tri-layer membrane fabrication (PEDOT:PSS/LIG/PDMS), and (3) Final device integration using plasma-assisted bonding.

(MicroChem). The required volume of thinner V_T to prepare any SU-8 30XX (where $XX < 50$) from SU-8 3050 is calculated using the following relation:

$$V_T = V_{\text{SU8}} \cdot \frac{\rho_{\text{SU8}}}{\rho_T} \left(\frac{SR_i}{SR_n} - 1 \right) \tag{2.5}$$

Here, V_{SU8} is the initial volume of SU-8 3050, ρ_{SU8} and ρ_T are the densities of SU-8 3050 and the thinner, respectively. Here, SR_i is the initial solids content of SU-8 3050, and SR_n is the target solids content for the desired SU-8 formulation. The spin coating process involves a 200 rpm spread cycle for 10 seconds, followed by a 30-second spin at 2000 rpm to achieve uniform thickness. The film is prebaked using a hot plate at 95 °C for 5 minutes, exposed using the mask aligner, and then

post-baked at 95 °C for 2 minutes. Finally, the substrate is developed to form an SU-8 cavity with thickness of 48 μm over the IDEs (Figure 2.3(1d)). In the second step, laser-induced graphene (LIG) is fabricated on a separate PI sheet using a CO_2 laser (22% power, 110 mm/s speed) (Figure 2.3(2a)). A PDMS (10:1 base-to-curing-agent ratio) layer is spin-coated over the LIG surface and thermally cured (80 °C for 5 hours) (Figure 2.3(2b)). The resulting cured PDMS/LIG composite is peeled off from the PI (Fig.2.3(2c)). Now, the trilayer stack is fabricated by pre-stretching the LIG/PDMS by 50% and fixing it using the clips (Figure 2.3(2d)). The layer of PEDOT:PSS is allowed to infiltrate into the porous LIG/PDMS structure and subsequently dried at 35 degrees for 20 minutes (Figure 2.3(2e)). Upon release of the pre-strain, the PEDOT:PSS formed a layer on the PDMS surface, conformally integrating with the porous graphene foam (Figure 2.3(2f)). In the final step, the PEDOT:PSS/LIG/PDMS membrane is aligned and bonded to the SU-8-patterned substrate using O_2 plasma treatment (5 minutes) to ensure strong adhesion [105]. This results in a suspended membrane structure over the electrode cavity, enabling hybrid capacitive-resistive sensing (Figure 2.3(3b)). This hybrid design integrates both capacitive and piezoresistive transduction mechanisms within a single sensing element. The device operates in a mode-adaptive sequential manner: capacitive sensing dominates at low pressures (0–15 kPa), while piezoresistive sensing activates at higher pressures (>15 kPa). The primary advantage is an extended sensing range

Table 2.1: Geometrical Parameters of the Tactile Sensor Array

Parameter	**Value**
Pixel pitch	6 mm (H), 7.5 mm (V)
Inter-electrode finger width	100 μm
Inter-electrode gap	100 μm
SU-8 cavity height	$\approx$ 48 μm
Total number of pixels	48

(0–86 kPa) within a single device. The key geometrical parameters of the sensing unit and array layout are summarized in Table 2.1. The sensing behaviour is governed by the SU-8 cavity height, interdigitated electrode separation, and pixel pitch. These parameters collectively define a trade-off between sensitivity, operating range, and inter-pixel crosstalk.

2.4 Results and Discussions

2.4.1 Morphological Characterization

Figure 2.4 illustrates the morphological evolution and structural integration of the laser-induced graphene (LIG) layer within the device architecture. The surface-view SEM images in Figure 2.4(a–c) demonstrate the influence of laser processing condi-

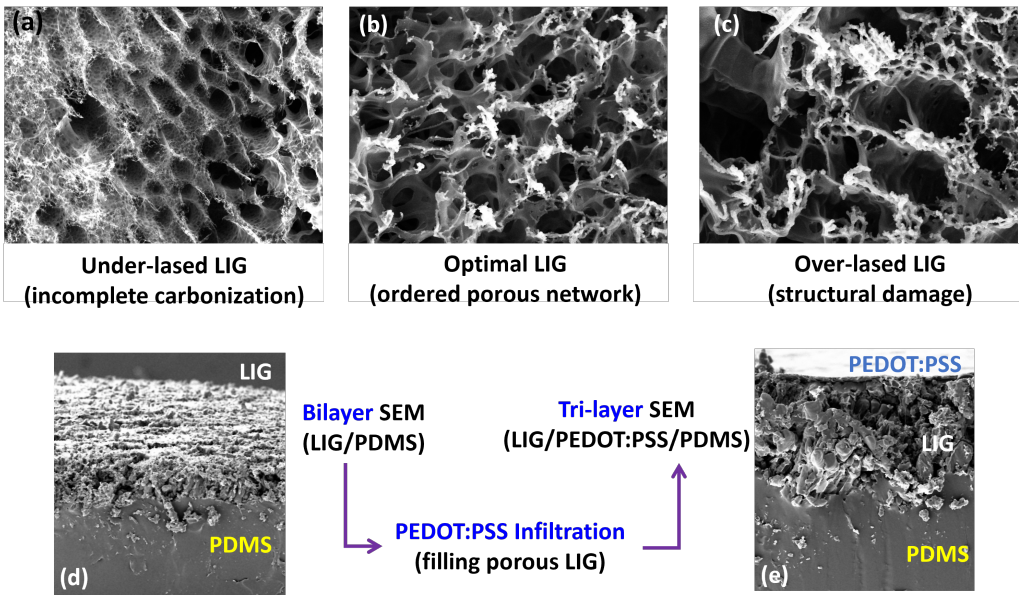
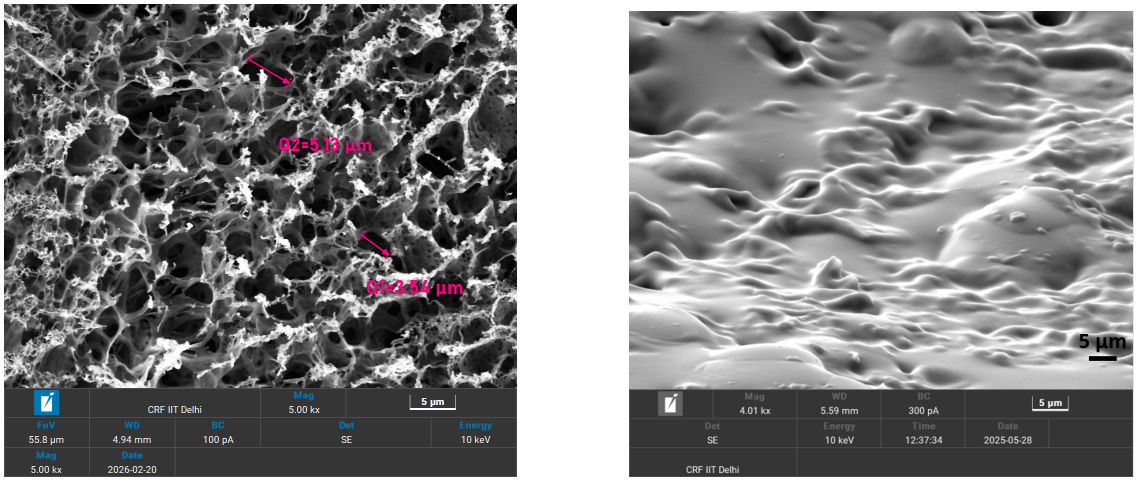


FIGURE 2.4: Morphological evolution and structural integration of LIG. (a–c) Surface-view SEM images showing under-lased (15%), optimized (22%), and over-lased (28%) LIG morphologies. (d) Cross-sectional SEM image of bilayer LIG/PDMS structure. (e) Cross-sectional SEM image of trilayer PEDOT:PSS/LIG/PDMS after polymer infiltration.

tions on the morphology of LIG.

At lower laser power (15%), the polyimide substrate undergoes incomplete carbonization, resulting in an under-lased structure with poorly developed porosity. Increasing the laser power to 22% produces an optimized LIG morphology consisting of a highly interconnected porous graphene network. This porous scaffold is desirable for device fabrication because it provides continuous conductive pathways and facilitates subsequent material infiltration. However, further increasing the laser power to 28% leads to over-lasing, where excessive thermal energy causes structural damage and partial collapse of the graphene framework.

The cross-sectional SEM image in Figure 2.4(d) shows the bilayer structure formed by LIG transferred onto the PDMS substrate. The porous graphene layer serves as a compliant interlayer that accommodates mechanical deformation while maintaining electrical conductivity. During fabrication, PDMS partially infiltrates the porous LIG scaffold, enhancing interfacial adhesion and mechanical compliance. Subsequently, a PEDOT:PSS coating is applied using a pre-strain-assisted process, allowing the conductive polymer to penetrate the porous graphene network and form



(a) (b)

FIGURE 2.5: Top SEM images: (a) LIG showing the mesopores in the range of 3-6 μm (b) LIG-coated PEDOT:PSS showing filling up of the pores to increase the conductivity.

a continuous film across its surface, as shown in Figure 2.4(e). This infiltration bridges microcracks within the LIG structure, improves inter-domain connectivity, and enhances electrical conductivity. The resulting trilayer architecture consisting of PEDOT:PSS/LIG/PDMS provides a mechanically robust and electrically continuous structure suitable for hybrid tactile sensing.

2.4.2 Electromechanical Characterization

The electromechanical characterization setup of a device consists of a force gauge (Mark-10) that has a resolution of 1 mN. The force gauge is fixed on the motorized force tester (ESM303) with a vertical displacement resolution of 2 μm (Figure A.1 (appendix)). Each device is tested by applying the force using an ESM303 motorized force tester, and the capacitance-resistance measurements are performed using a semiconductor parameter analyzer (Keithley 4200A-SCS). The applied force on the device induces the deflection in the suspended tri-layer, which is separated from the IDE by the SU-8 spacer. This deflection reduces the gap between the electrodes and the suspended conductive layer. As a consequence, the effective permittivity ε_{eff} in the vicinity of the IDE fringe field is altered, leading to a change in capacitance (Equation 2.1 and 2.3). This mechanism is illustrated in Figure 1(a-d) and is analytically described using the partial capacitance model introduced in Equation 2.3 (Figure 2.2). However, the device exhibits only a slight change in capacitance within the low-pressure range of 0–3.2 kPa (Figure 2.6(a)). As the applied force exceeds 3.2 kPa, a more significant increase in capacitance occurs. Between 3.2 kPa and 14.1 kPa, the device shows a sharp rise in capacitance, reaching up to 10.5 pF. Additionally, we compared the capacitance change between a bilayer (LIG/PDMS) and a trilayer (PEDOT:PSS/LIG/PDMS) structure. The tri-layer demonstrates a

sixfold higher capacitance change than the bi-layer structure (Figure 2.6(c)). A secondary observation within this regime is proximity sensing, as shown in the inset of Figure 2.6(a). As the indenter approaches the membrane without touching, fringing field lines terminate on the conductive surface, producing a transient dip in measured capacitance. Upon contact, the capacitance resumes its pressure-induced rise, consistent with the partial capacitance model. This demonstrates the device's dual

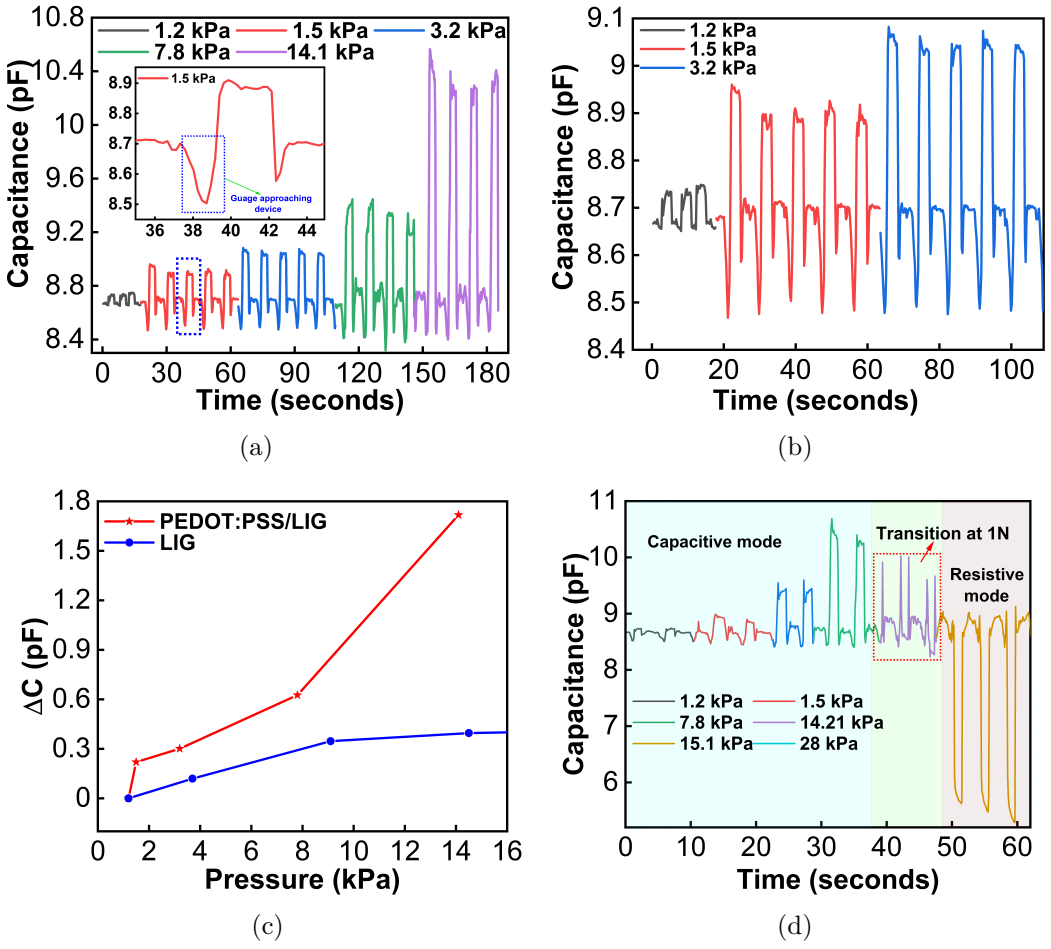
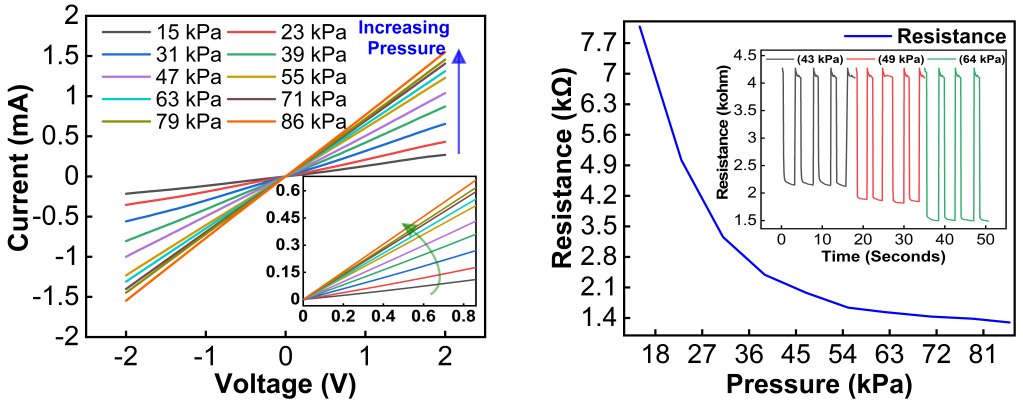


FIGURE 2.6: (a) Capacitive response of the device in the non-contact regime (1.2–14.1 kPa), demonstrating increasing capacitance with applied pressure. The inset highlights the proximity effect as the force gauge approaches the membrane. (b) Enlarged view of the low-pressure region (1.2–3.2 kPa), showing fine-scale capacitive changes. (c) Comparative capacitive response of bi-layer (LIG/PDMS) and tri-layer PEDOT:PSS/LIG/PDMS) membranes, illustrating enhanced performance with the tri-layer design. (d) (i) Electromechanical response across different modes. At 15 kPa, the device shows the transition from capacitive to resistive mode.

sensitivity to both mechanical deformation and approaching conductive objects. At 15 kPa, the tri-layer suspended membrane touches the IDE. The transition is confirmed using two independent approaches. First, from capacitance measurements, a decline in measured capacitance is observed even though the applied force continues to increase (Figure 2.6 (d)). Second, the transition is confirmed through current–voltage (I–V) characterization. Once contact occurs, the device shows a linear I–V response. This indicates the formation of a resistive conduction path across the electrodes. Figure 2.7(a) illustrates the transition of the device into resistive mode within the higher force range (15–86 kPa). When the voltage is swept from –2 V to 2 V, the output current exhibits a linear response. This behaviour confirms the formation of an ohmic contact between the PEDOT:PSS layer and the Au-based interdigitated electrodes (IDEs). As the applied pressure increases, the magnitude of the current also rises. This indicates the development of additional conductive pathways due to the expansion of the contact area between the sensing film and the electrode surface. The inset of Figure 2.7(b) presents the dynamic force–resistance response of the device. A preload of 27 kPa is first applied to initi-

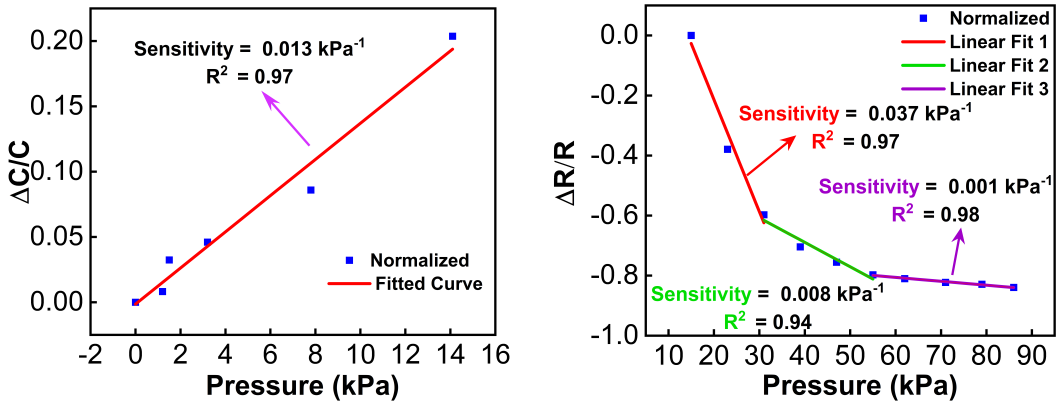


(a) (b)

FIGURE 2.7: (a) I–V characteristics of the device in the contact regime, showing a linear relationship and confirming ohmic conduction. The inset provides a zoomed-in view of the first quadrant. (b) Resistance variation as a function of applied pressure (15–86 kPa), with an inset showing the dynamic response across multiple loading cycles.

ate contact between the suspended sensing layer and the IDE, ensuring the device operates in resistive mode. Subsequent resistance values are measured with respect to this baseline contact condition. As the applied pressure increases beyond 27 kPa, the resistance decreases, indicating enhanced electrical contact and the formation of additional conductive pathways across the interface. To assess the mechanical reversibility of the device, cyclic loading–unloading tests are performed at pressures of 43, 49, and 64 kPa. Upon removal of the applied force, the suspended membrane retracted to its original position, breaking contact with the IDE. This return to a high-resistance, non-contact state confirms that the membrane does not adhere to the electrodes after unloading. The sharp increase in resistance after each unloading cycle further validates the complete mechanical recovery of the device.

Furthermore, the sensitivity S of the device, defined as $S = \frac{\partial(\Delta C/C_0)}{\partial P}$ or $\frac{\partial(\Delta R/R_0)}{\partial P}$, is derived from the capacitance-resistance-pressure characteristics. Figure 2.8 reveals distinct sensitivity behavior across the 0–86 kPa range. Capacitive operation

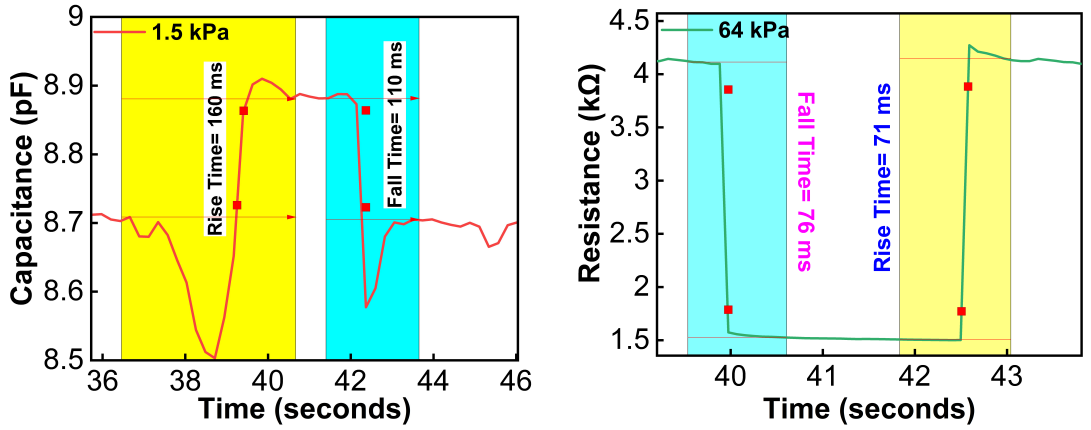


(a) (b)

FIGURE 2.8: Sensitivity analysis of the suspended PEDOT:PSS/LIG/PDMS hybrid tactile sensor. (a) Capacitive mode: relative capacitance change ($\Delta C/C_0$) vs. pressure (0–14.1 kPa); linear fit yields $S_C \approx 0.013\,\text{kPa}^{-1}$ ($R^2 = 0.97$). (b) Resistive mode: normalized resistance change ($\Delta R/R$) vs. pressure (15–86 kPa), revealing three sub-regimes: $S_R \approx 0.037\,\text{kPa}^{-1}$ ($R^2 = 0.97$) from 15–31 kPa, $S_R \approx 0.008\,\text{kPa}^{-1}$ ($R^2 = 0.94$) from 31–55 kPa, and $S_R \approx 0.001\,\text{kPa}^{-1}$ ($R^2 = 0.98$) above 55 kPa.

achieves a sensitivity of $S_c \approx 0.013\,\mathrm{kPa}^{-1}$ ($R^2 = 0.97$) across 0–14.1 kPa. In the resistive mode, three distinct sub-regimes are identified: $S_R \approx 0.037\,\mathrm{kPa}^{-1}$ ($R^2 = 0.97$) in 15–31 kPa, $S_R \approx 0.008\,\mathrm{kPa}^{-1}$ ($R^2 = 0.94$) in 31–55 kPa, and $S_R \approx 0.001\,\mathrm{kPa}^{-1}$ ($R^2 = 0.98$) above 55 kPa, reflecting progressive saturation of the contact area at higher pressures. The initial high sensitivity stems from the newly formed contact in the tri-layer structure, where PEDOT:PSS/LIG contact with electrodes abruptly increases the contact area, dramatically reducing resistance. The further increase in force causes the mechanical saturation, resulting in a decrease in resistance change.

To evaluate transient performance, the device is tested under pulsed pressures of 1.5 kPa and 64 kPa for the capacitive and resistive modes, respectively. The capacitive device demonstrated response and recovery times of approximately 160 ms and 110 ms (Figure 2.9(a)), while the resistive mode showed slightly lesser times of 76 ms and 71 ms (Figure 2.9(b)). The faster response observed in the resistive mode is attributed to the rapid formation of conductive contact pathways upon membrane–electrode contact. In contrast, the capacitive response is governed by dielectric deformation and viscoelastic relaxation of the PDMS layer. The hybrid device exhibits



(a) (b)

FIGURE 2.9: (a) Transient response of the device in capacitive mode, exhibiting a rise time of 160 ms. (b) Time-domain response of the device in resistive mode, exhibiting a rise time of 71 ms.

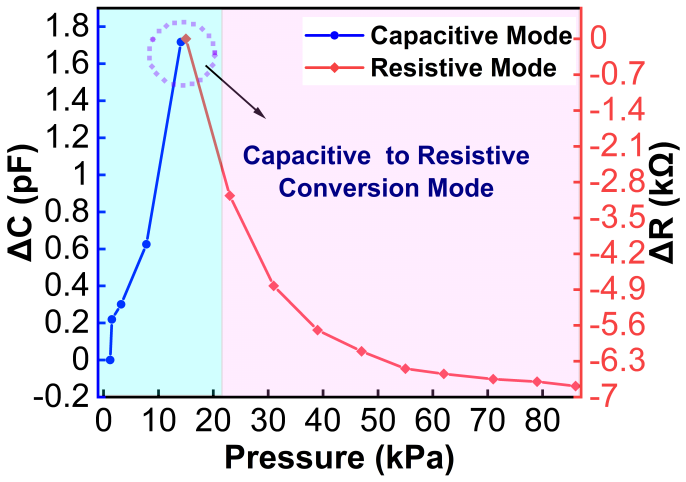
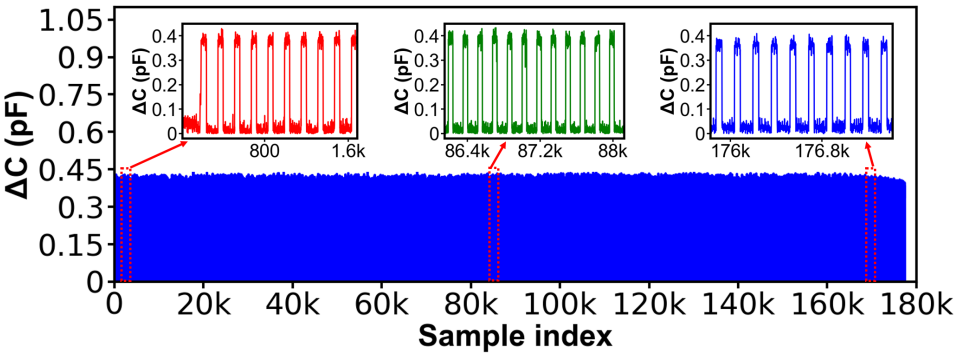


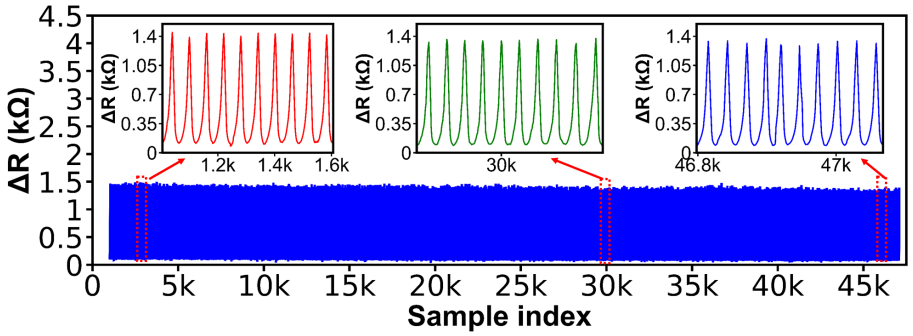
FIGURE 2.10: (a) Combined electromechanical response in hybrid capacitive–resistive mode, covering the full pressure range (0–86 kPa)

response times that are comparable to previously reported flexible sensors for similar applications, as summarized in Table 2.2. Figure 2.10 demonstrates the hybrid response of the device over entire sensing range. Combined capacitive-resistive operation enables wide-range force detection (0–86 kPa) with better sensitivity across, leveraging both mechanisms' complementary characteristics.

To further evaluate the durability of the hybrid sensor, cyclic loading–unloading tests are performed, as shown in Figures 2.11(a) and (b). A total of 2400 cycles is conducted, with 1200 cycles assigned to each transduction mechanism. In the capacitive mode [Figure 2.11(a)], the ΔC response remained highly stable with an overall drift of –1.63% relative to the first cycle, demonstrating consistent performance over extended use. In the resistive mode (Figure 2.11(b)), the $\Delta R/R$ signals are reproducible throughout the test, with the baseline drift stabilizing near –2% and peak drift stabilizing at approximately –5% after 2400 cycles. Also, the ΔR is within 3% drift range, making the signals highly reproducible and free of creep. Despite minor drift, both mechanisms retained their response integrity without signal degradation, confirming the long-term reliability of the device.



(a)

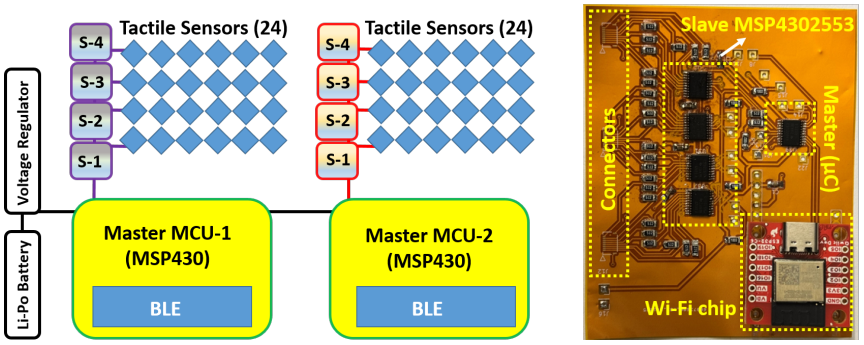


(b)

FIGURE 2.11: Stability test result of the device in 2400 cycles. (a) In capacitive mode for 1200 cycles. (b) In resistive mode for 1200 cycles.

2.4.3 Readout Electronic Circuitry

A tactile sensing system for human–machine interfaces (HMI) is developed with 48 individually addressable sensors. These sensors are interfaced with a modular readout circuit designed on a flexible PCB, as shown in Figure 2.12. The system leverages a hierarchical microcontroller architecture using MSP430G2553 chips to achieve low-latency, scalable data acquisition. The architecture comprises eight slave and two master microcontrollers. Each slave acquires analog signals from six devices using its internal 10-bit ADC, enabling local digitization without shared analog signal paths. In this configuration, each sensor pixel is connected to a dedicated electrode and a per-channel ADC input on the slave microcontroller, forming a fully parallel analog



(a) (b)

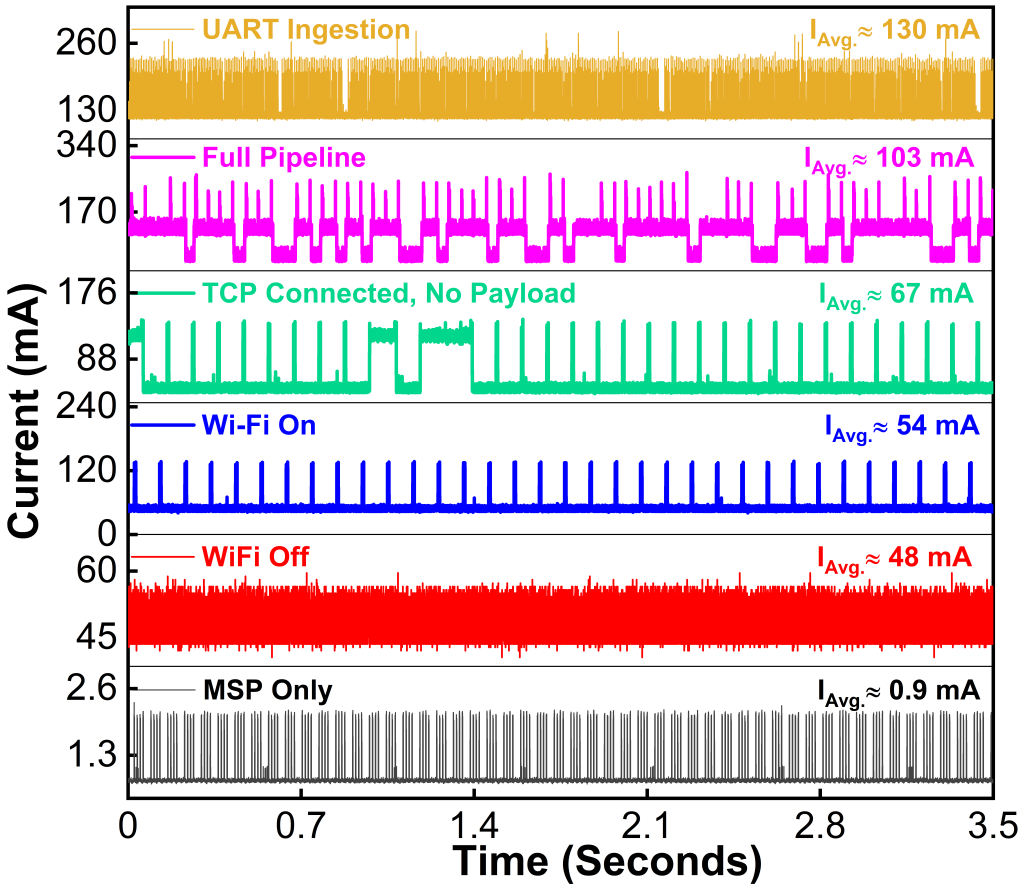
FIGURE 2.12: (a) Circuit diagram of the modular readout system with a 20 ms refresh rate. (b) Implementation of the circuit on a flexible PCB interfaced with ESP32 for wireless data transmission.

front-end. The slave then performs local processing such as averaging or filtering, and transmits the digitized data to the corresponding master via the I²C protocol (Figure B.1, appendix). Each master MSP430 communicates with four slave devices, maintaining independent I²C buses. To ensure synchronized acquisition, a dedicated GPIO line is used for inter-master triggering. One master initiates acquisition by sending a rising-edge signal to the second. This setup ensures all 48 device readings are captured simultaneously across the network. The master packages the incoming data, appends timestamps, and forwards it over UART to ESP32 modules, which handle wireless transmission (Wi-Fi or BLE) to a PC. A low-noise 3.3V power supply, regulated by an AMS1117 LDO with decoupling networks, ensures stable ADC operation. Figure 2.12 (a-b) shows the schematic of the readout electronics and flexible PCB for the tactile device.

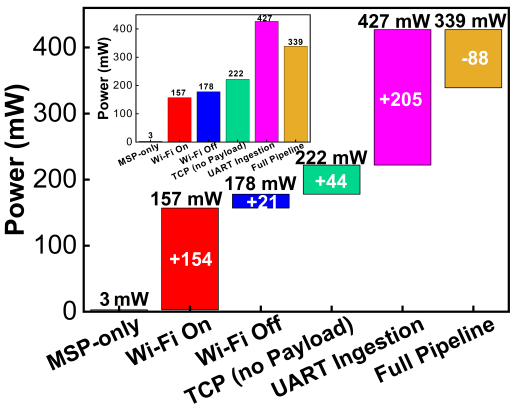
For the latency measurements, the 24-pixel tactile array is defined as the fundamental unit. It is organized into four I²C slave modules, each managing six channels, to achieve a compact and temporally deterministic acquisition cycle. Latency measurements utilize an on-chip microsecond timer within the MSP430G2553 master. With all per-slave data prints disabled, the complete four-slave scan requires 8.07 ± 2 ms, defining the true electronic latency from the acquisition trigger to data readiness.

Incorporating full data serialization, UART transmission at 1 Mbaud, and Wi-Fi forwarding via the ESP32 bridge are included, the effective system-level latency increases to 50 ± 5 ms per 24-pixel frame. This sub-100 ms performance meets the requirement for real-time tactile feedback. The low and deterministic latency validates the hierarchical parallel readout architecture and confirms its suitability for real-time interactive systems.

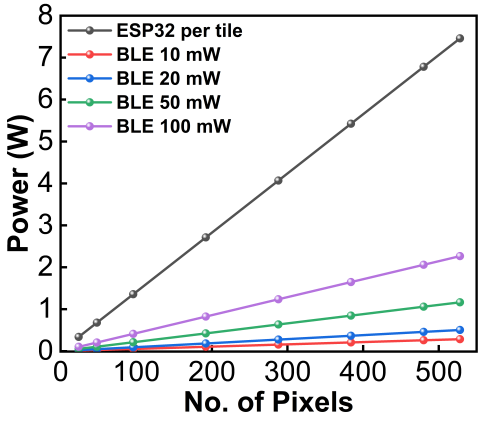
While the latency profile confirms architectural feasibility, power consumption identifies a constraint for further scaling. The detailed power profiling of the readout circuitry is performed using a Nordic PPK2 power profiler, with a 24-pixel tile defined as the fundamental unit. The methodology involved a staged activation of system components, progressing from a minimal MSP430 baseline to the full data transmission pipeline. The corresponding current and power consumption are detailed in Figure 2.13(a) and (b), respectively. The analysis reveals a decomposed power budget, isolating the contribution of each operational state. The MSP-only baseline consumes 2.96 mW (123 µW per pixel). Initialization of the ESP32 core and subsystems introduces a significant overhead, increasing the power to 157 mW (an increment of +154 mW). Subsequent Wi-Fi association raises consumption to 178 mW (+21 mW), while maintaining a TCP connection further increases it to 222 mW (+44 mW). The most substantial power burden arises from 1-Mbaud UART data ingestion, which elevates power draw to 427 mW (+205 mW). In the full operational pipeline, integrating UART ingestion with Wi-Fi forwarding, the average power settles at 339 mW (14.1 mW per pixel). This final state demonstrates a saving of 87 mW relative to the ingest-only condition, achieved through reduced buffering overhead from active host reading. The analysis identifies UART ingestion and wireless transport as the primary targets for future optimization and scaling efforts. Consequently, future iterations could significantly reduce power consumption by integrating low-power BLE with deep sleep modes.



(a)



(b)



(c)

FIGURE 2.13: System characterization of the 24-pixel tactile tile. (A) Current consumption profile during the staged activation of system components, from the MSP-only baseline to the full data pipeline, measured with a Nordic PPK2. (B) The corresponding decomposed power budget for each operational state, highlighting the incremental contributions of the ESP32, Wi-Fi, TCP, and UART subsystems. (c) Power scaling projection for larger arrays, comparing the total system power for a 512-pixel array using the current ESP32-per-tile architecture versus alternative low-power bridge solutions with fixed overheads.

The MSP-only establishes an intrinsic electronic slope of 0.1233 mW per pixel. However, with the present ESP32 bridge per tile, the measured full-pipeline power is 339 mW. For larger arrays operating in parallel, this model projects a total power of 7.46 W for a 512-pixel array (Figure 2.13(c)). This confirms that duplicating the high-overhead ESP32 gateway for every tile dominates the system budget and is impractical for scalable deployment. To overcome this limitation, a low-power architectural alternative is essential. Replacing the ESP32 with a per-tile bridge of bounded overhead (while preserving the intrinsic per-pixel slope) improves efficiency. For 22 tiles (512 pixels), the total power consumption becomes 0.285 W, 0.505 W, 1.165 W, or 2.265 W for bridge overheads of 10 mW, 20 mW, 50 mW, or 100 mW per tile, respectively. This analysis directly motivates the integration of a low-power Bluetooth Low Energy (BLE) protocol, which is capable of achieving the target sub-100 mW overhead. Coupled with deep sleep modes, BLE presents a viable path to reduce operational power. Consequently, while the per-tile power slope is favorable, a power-efficient wireless gateway (e.g., BLE) is necessary to establish a viable operating point at scale.

2.4.4 Cross-talk and Multitouch

One of the most prevalent issues in tactile devices is crosstalk. Crosstalk is unintended interference or signal mixing between adjacent pixels in a tactile sensing array. Crosstalk in tactile device arrays commonly arises from two main sources: design-related and circuitry-related factors. From a design perspective, crosstalk is often caused by the use of continuous, non-patterned functional materials and shared electrode structures. This allows electrical signals at one pixel to spread to adjacent pixels. In addition, insufficient mechanical isolation between pixels may allow deformation to propagate to adjacent sensing units, further contributing to

signal interference. On the circuitry side, the reliance on multiplexed or shared readout lines can result in electrical interference between device channels during signal acquisition.

To eliminate crosstalk, the problem is addressed at both levels as shown in Figure 2.14 (a-d). Our architecture eliminates crosstalk through a holistic strategy that integrates three key approaches. First, functional layer patterning is achieved by defining each pixel with a dedicated PEDOT:PSS/LIG/PDMS trilayer region (Figure 2.14 (c)). Second, mechanical isolation is provided by high-modulus SU-8 spacers that physically separate adjacent pixels to confine deformation (Figure 2.14 (d)). Finally, for circuit isolation, the architecture employs distributed slave modules, each providing independent ADC channels that are directly hardwired to individual sensor elements (Figure 2.14 (a)). This fully parallel, non-multiplexed readout completely avoids the signal interference inherent in shared or time-multiplexed circuits, ensuring every tactile input is captured with high fidelity and zero crosstalk. To quantify the residual coupling, individual pixels are activated, and the crosstalk is computed. Crosstalk is evaluated by actuating a single pixel while simultaneously recording all channels. For each actuation, the steady-state response of the actuated pixel and the corresponding side-neighbour and diagonal-neighbour pixels are averaged over the same number of samples. Crosstalk is defined as the normalized ratio of the averaged neighbor response to the averaged actuated-pixel response and expressed as a percentage. The measured side-neighbor and diagonal-neighbor crosstalk values are 0.29%/0.22% for pixel S3, 0.25%/0.22% for S4, and 0.18%/0.18% for S23. For each pixel, the actuation–measurement sequence is repeated over 100 loading cycles, and the reported values represent the mean over the repeated trials. The overall mean crosstalk is 0.23%, with all cases remaining below 0.3%. These results validate that the combined mechanical isolation (SU-8 cavity walls) and per-channel ADC

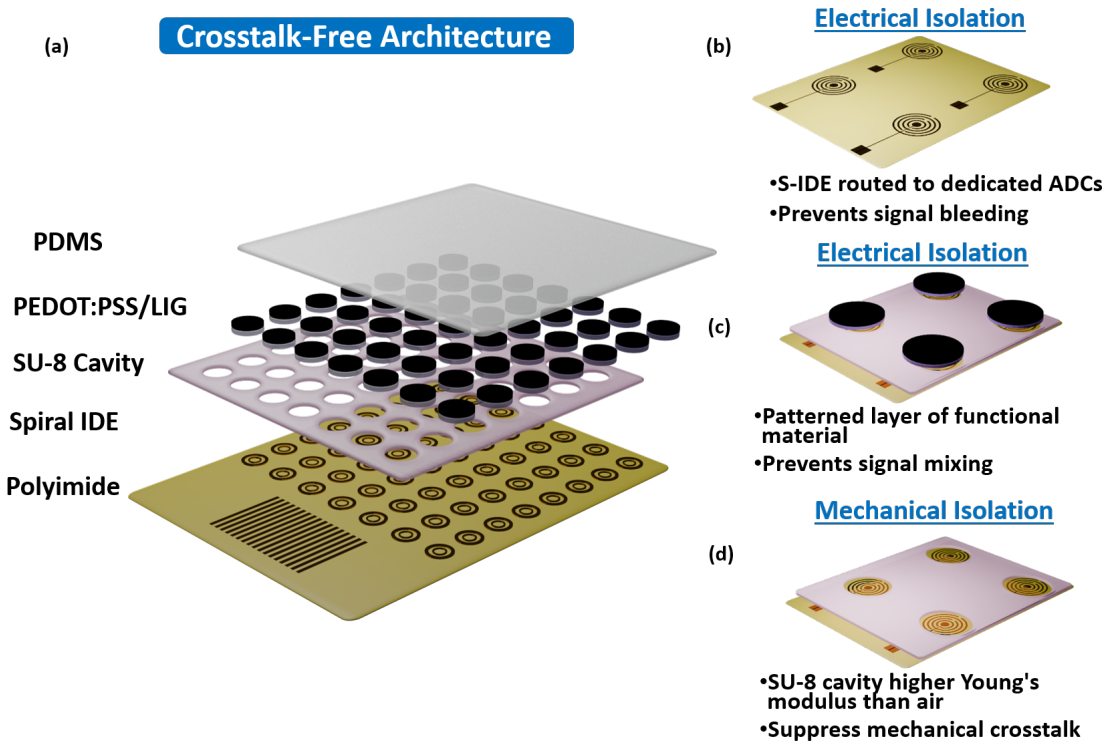


FIGURE 2.14: Crosstalk suppression strategies in the device architecture: (a) Exploded view showing the layered structure of the sensor. (b) Each IDE is routed to a dedicated analog-to-digital converter (ADC) to prevent electrical crosstalk or signal bleeding. (c) The patterned functional layer confines conduction paths, minimizing electrical crosstalk across adjacent pixels. (d) SU-8 cavities act as mechanical isolation barriers to suppress deformation-induced coupling.

decoupling successfully suppress crosstalk to a negligible level, ensuring precise spatial localization and stable multi-touch operation. The effectiveness of this crosstalk suppression strategy and multipoint detection is experimentally verified using 3D line plots and spatiotemporal heatmaps. As shown in Figure 2.15(a-b), selective activation of specific channels (e.g., S3 and S5) produced a clear response confined to the stimulated pixels, while all other channels remained inactive. When three devices (e.g., S3, S5, and S23) are simultaneously actuated (Figure 2.15(b)), the system captures independent responses on each channel without any signal overlap, validating the multi-touch capability. These results demonstrate that the proposed architecture effectively eliminates crosstalk and enables robust multi-touch sensing

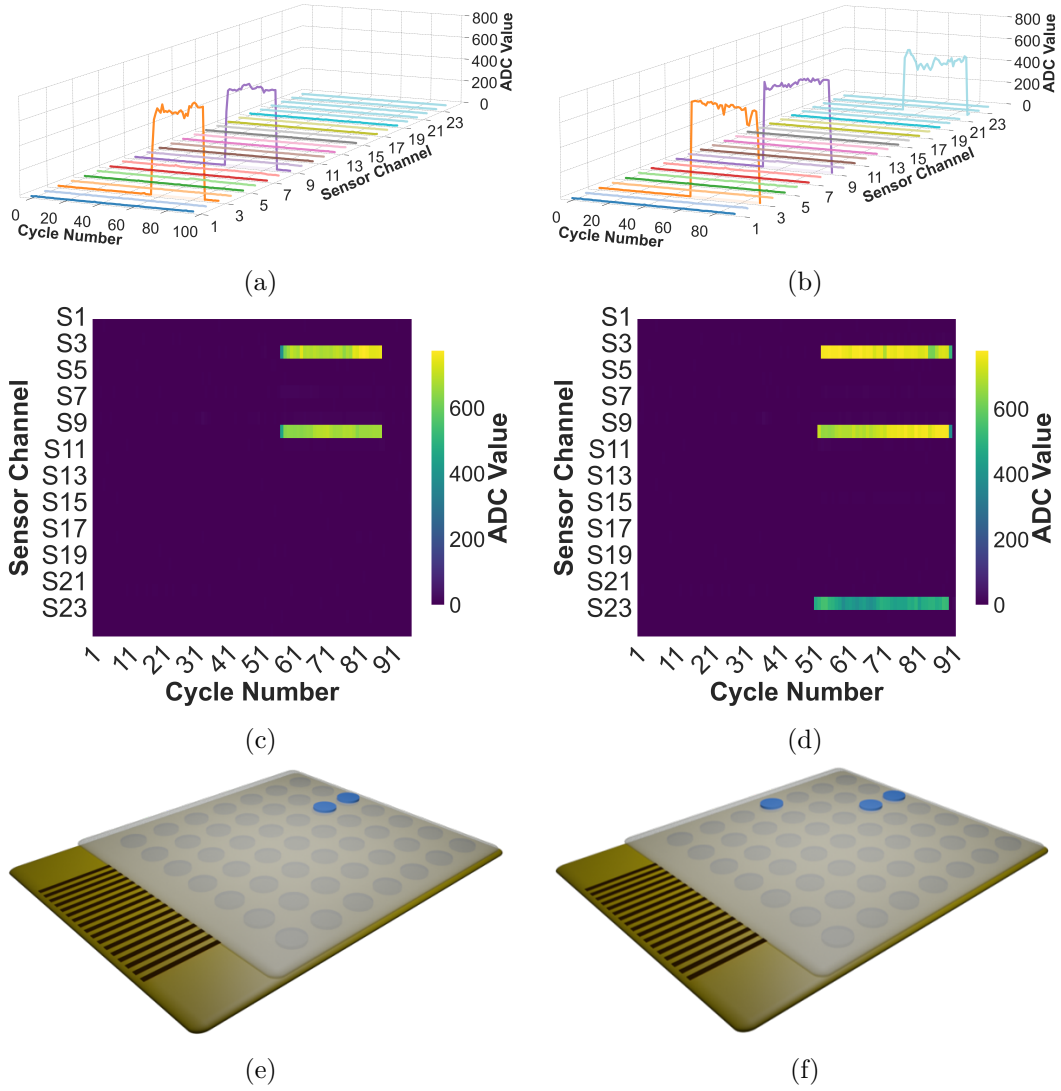


FIGURE 2.15: Cross-talk-free and multi-touch sensing demonstration: (a-b) Sensor schematics showing measurement points, (c-d) Heatmap responses demonstrating pixel isolation, (e-f) Selective actuation of specific pixels (e.g., S3, S5, S23) showing independent, localized responses with no signal overlap, confirming channel separation integrity.

performance. To further evaluate the performance of the proposed hybrid tactile sensor, its key metrics are compared with previously reported flexible pressure sensors in the literature and are summarized in Table 2.2.

TABLE 2.2: Benchmark Comparison with Previously Reported Flexible Pressure Sensors.

Ref.	Material System	Sensing Mode	Sensitivity (kPa^{-1})	Pressure Range (kPa)	Response Time (ms)	Crosstalk (%)	Durability (cycles)
[93]	Parylene/TPU	Capacitive	0.14	0–10	195	NA	1000
[106]	CNT/CB/TPU	Resistive	0.10	0–23.3	119	NA	1000
[107]	Graphene	Resistive	0.17	0–20	120	NA	NA
[108]	CNT–PDMS	Resistive	0.03	0–50	100	NA	NA
[109]	PDMS/Cu/CuNWs	Resistive	0.14	0.1–15	150	NA	1000
[110]	SU-8/Graphene	Capacitive	0.01	0–30	70	NA	500
This Work	**PEDOT:PSS/LIG /PDMS**	**Hybrid**	**0.03**	**0–86**	**71**	**0.3**	**2400**

2.5 Application

Traditional keypad locks are vulnerable to security breaches, as unauthorized users can easily replicate access by simply observing or recording the numeric code. To overcome this limitation, we introduce a pressure-based locking system that uses biometric authentication through tactile sensing (Figure 2.16(a-d). Each sensor distinguishes four discrete pressure levels (P1–P4: light, medium, hard, and very hard), converting them into unique analog responses within a 0–3.3 V range, which are processed in real-time by a microcontroller. A Python-based program acquires and classifies the pressure data via Wi-Fi, verifying both the input digits and their associated pressure intensities. As shown in the waveform plots, authentication is granted only when both the numeric sequence and the associated pressure intensities are correct. For example, the actual password "7722" requires the sequence 7(P2), 7(P3), 2(P1), and 2(P4). In the verified case (Figure 2.16(c)), each keystroke produces the expected pressure amplitude class, resulting in successful authentication. In contrast, the failed attempt (Figure 2.16(d)) shows mismatched pressure amplitudes despite the same digit sequence, leading to rejection. This dual-parameter verification significantly enhances security by embedding a biometric dimension into the conventional lock interface, enabling a smarter and more personalized access control mechanism.

Beyond authentication, the tactile device also serves as a flexible Human-Machine Interface (HMI). A Mario-style platformer game is implemented to demonstrate continuous real-time interaction. The schematic highlights the closed-loop cycle, as illustrated in Figure 2.16(e–f). The process begins with tactile input, where the

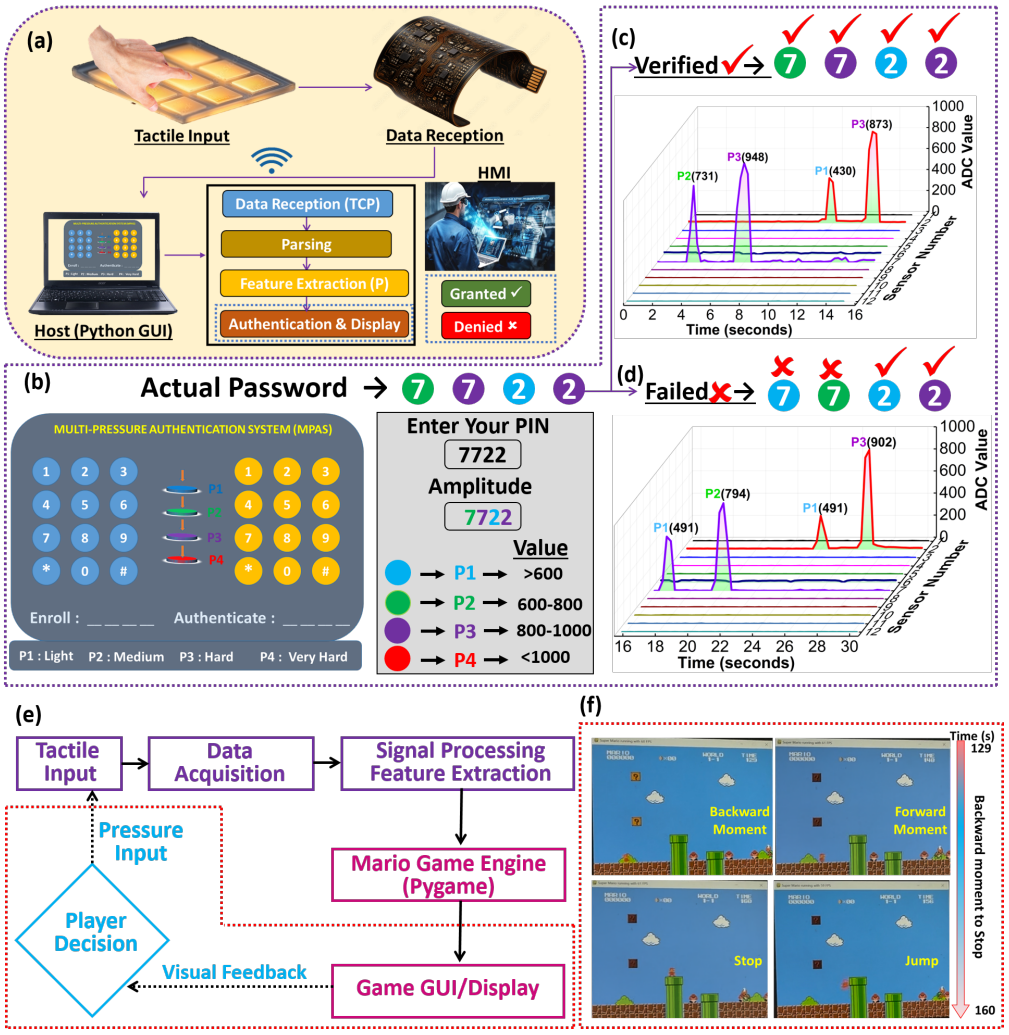


FIGURE 2.16: (a) Schematic of the pressure-based multi-parameter authentication system (MPAS) for secure digital lock applications. (b) Photograph of the tactile sensing array integrated into the lock interface. (c) Waveform plot of a verified password attempt ("7722") showing correct digit–pressure mapping. (d) Waveform plot of a failed attempt with mismatched pressure levels despite correct digits. (e) Schematic of the tactile device used as a Human–Machine Interface (HMI) for a Mario-style platformer game, highlighting the closed-loop feedback between player input and game display. (f) Gameplay screenshots demonstrating tactile control of Mario for forward, backward, jump, and stop actions.

player applies pressure to designated sensor pixels or pixel groups mapped to specific actions. These inputs are acquired and translated through spatial pixel mapping into predefined in-game commands, such as walk, run, and jump, rather than through continuous pressure-intensity classification. The commands are sent to the Mario game engine, built using Pygame, which updates the game state accordingly. The resulting visual feedback is displayed on the game GUI, allowing the player to observe Mario's actions and adapt subsequent inputs in real-time. To quantitatively evaluate the reliability of this interaction scheme, the accuracy of action recognition is measured. This metric is defined as the percentage of trials in which activation of a designated pixel group correctly triggered the intended command. Using this metric, the system achieved an overall accuracy of 95% across three representative actions (walk, run, and jump) in repeated trials. These results confirm the reliability of pixel-based action mapping for real-time human–machine interaction.

2.6 Conclusion

In conclusion, we demonstrated a flexible suspended hybrid tactile sensor that integrates capacitive and piezoresistive transduction mechanisms within a crosstalk-free design. The device architecture consists of a suspended PEDOT:PSS-coated laser-induced graphene (LIG) film on a PDMS substrate, positioned above interdigitated electrodes. A patterned SU-8 spacer defines the sensing gap. This enables pressure-dependent switching between non-contact (capacitive) and contact (piezoresistive) sensing modes. The capacitive mode operates in the low-pressure regime (0.3–15 kPa) with a peak sensitivity of 0.013 kPa^{-1}. The piezoresistive mode covers a higher pressure range (15–86 kPa) with a highest sensitivity of 0.03 kPa^{-1}. To suppress crosstalk between adjacent pixels, a dual-layered approach is employed. Each

sensing unit is physically isolated in the device layout and electronically decoupled through a fully parallel, per-channel ADC readout architecture, which suppresses both mechanical and electrical crosstalk to below 0.3%. Furthermore, a hierarchical MSP430–ESP32 readout pipeline enables real-time wireless data acquisition with low latency (50 ± 5 ms), ensuring system-level responsiveness. The proposed sensor demonstrates reliable performance in real-time applications. These include a multi-pressure authentication system (MPAS) and a gesture-controlled Mario-style game.

Chapter 3

Direction-Sensitive and Bimodal Capacitive Sensors for Human Motion Monitoring

This chapter presents two sections for electromechanical sensing for human motion monitoring. The first section introduces a 3×3 epidermal asymmetric capacitive pixel (E-CaP) array that provides direction-sensitive capabilities for mapping epidermal movements. The device features a μm-meshed PDMS dielectric layer integrated between asymmetric electrodes. The second section builds on this by presenting a bimodal device capable of concurrent strain and proximity detection. The sensor employs a PDMS matrix embedded with magnetic nanoparticles and is implemented with a single capacitive readout, complemented by a power-saving algorithmic strategy. Its applicability is demonstrated in limb-movement monitoring tasks.

3.1 Asymmetric Capacitive Pixel Array for Mapping Epidermal Vectored Movement

This section presents a 3 × 3 epidermal asymmetric capacitive pixel (E-CaP) array with direction-sensitive capabilities. The asymmetric design is motivated by the need to incorporate directional sensitivity into flexible tactile devices. A μ-meshed PDMS dielectric layer is integrated between asymmetric electrodes to allow conformal attachment and shear displacement. The functionality of the E-CaP array is validated through simulations and experimental characterization, confirming its ability to map epidermal movements with directional specificity.

3.1.1 Introduction

Epidermal skin (E-Skin) patches based on soft electronics are promising futuristic systems that find applications in movement tracking [17], healthcare [111], and robotics [112]. In biomechanics, direction-sensitive e-skins are indispensable to biomechanical tasks, such as object gripping and manipulation [113]. Furthermore, the direction-sensitive E-skins offer enormous promise in the field of gait biomechanics, such as walking and running, as well as in the detection of problems such as pressure ulcers [114]. Also, medical conditions such as Parkinson's disease, limb amputations, or postsurgical rehabilitation resulting in gait difficulties can all be evaluated with the directional-sensitive e-Skins [115].

Commercially available direction-sensitive devices are typically silicon-based, making them rigid and costly, and thus limiting their applicability in personal healthcare [116]. Additionally, most of the devices are incapable of discerning the direction-sensitive behavior when mounted on skin [117, 118]. Recently, flexible devices based

on polymers have shown great promise in achieving enough flexibility to conformally attach to the skin [119]. To obtain directional sensitive capabilities, a flexible device based on an out-of-plane bump structure has been reported [120]. However, bump structure adds complexity to the fabrication process, thereby reducing the rapid prototyping of the device. Furthermore, due to its rigidity, higher forces cause the bump structure to fracture [121]. The flexible device based on a solid dielectric layer with a multilayer planar structure has also been reported [122]. However, multilayer stacking results in alignment issues, leading to an erroneous response. Furthermore, the solid polymer limits the ability of the device to respond to shear force due to higher rigidity, causing the delamination of layers against each other [123].

Here, we demonstrate a 3×3 epidermal asymmetric capacitive pixel (E-CaP) array with direction-sensitive capabilities. The conformally laminated E-CaP has a capacitive sensing mechanism and effectively maps the direction and the pressure of epidermal movements. The difference between the previously retained and the present value of the response represents the rate of change of capacitance. This rate of change per unit displacement is crucial to determine the vectored response of the strain-induced in the E-CaP. The nominal capacitance of the array is ∼3.370 pF and shows a prominent change (d) of $1.341\hat{i} + 2.007\hat{j} + 8.750\hat{k}$ pF/mm. The micromeshed (μ-meshed) polydimethylsiloxane (PDMS) structure is fabricated using SU8 μ-mold and is sandwiched between the asymmetric electrodes. The μ-meshed design offers greater shear displacement, allowing the E-CaP to move conformally with the skin. The possible movement domain associated with the limbs that are laminated with E-CaP can map the entire generated vector response (direction-specific). The E-CaP is simulated and tested for mapping the direction-sensitive epidermal movement.

3.1.2 Device Concept and Design

3.1.2.1 Working Mechanism

Figure 3.1 shows the 3-D schematic of E-CaP array. The E-CaP array has a simpler design and provides a direction-sensitive capacitive readout, which simplifies epidermal circuit design. The proposed device consists of a 3 × 3 elemental pixel array. Each unit pixel has an asymmetric structure in the xy plane. This asymmetric geometry imparts a vectored ($\vec{d}$) rate of change of capacitance, enabling direction-sensitive operation. The sensor response arises from the shear displacement of the μ-meshed PDMS dielectric layer, i.e., relative movement of the top electrode with respect to the bottom electrode. The electrodes are fabricated using a thin metallic (aluminum) layer deposited on flexible polyethylene terephthalate (PET) sheets. A thin μ-meshed PDMS dielectric layer is sandwiched between these asymmetric electrodes, forming E-CaP. The viscoelastic μ-mesh enhances stretchability, thereby allowing the sensor to map the epidermal strain movement. Furthermore, the sandwiched μ-mesh enables the sensor to respond to normal pressure stimuli. Compared

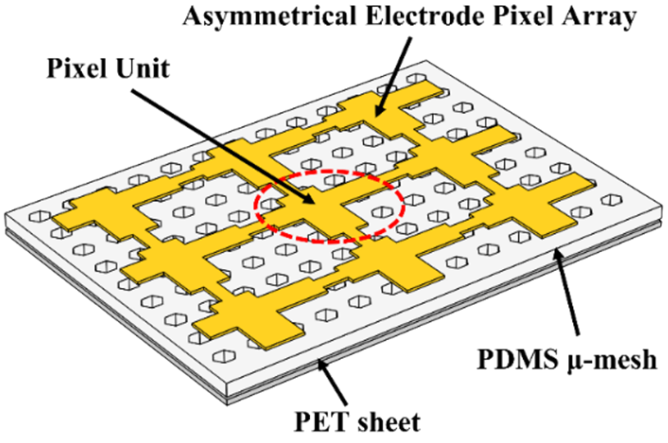


FIGURE 3.1: Schematic of the 3-D prototype of E-CaP in the relaxed state showing key components.

to a bulk dielectric film, the μ-mesh structure provides superior shear compliance and performance [124].

3.1.2.2 Analytical Model

To quantify the response of the asymmetric unit, an analytical model was developed as shown in Figure 3.2. The simplified 2-D schematic illustrates the in-plane displacement of an E-CaP unit pixel (Figures 3.2(ii) and 2(iii)). Initially, the electrodes are completely overlapped, having an initial capacitance $C_n = \left(\sum_{n=1}^{5} C_i\right)$ (Figure 2(i)). The displacement in the xy-direction changes the overlapping area, resulting in a capacitance change. The primary assumption is that the top electrode moves parallel to the bottom electrode without any change in the electrode gap [125]. The initial capacitance C_1 is given by:

$$C_1 = \frac{\varepsilon_0 \varepsilon_r A_1}{d} = \frac{\varepsilon_0 \varepsilon_r b^2}{d} \tag{3.1}$$

where ε_0 and ε_r are the permittivities of free space and the dielectric layer, respectively, and d is the gap between the top and the bottom electrodes. When the relative deflection of the top electrode is less than 0.1 cm in the x-direction, the

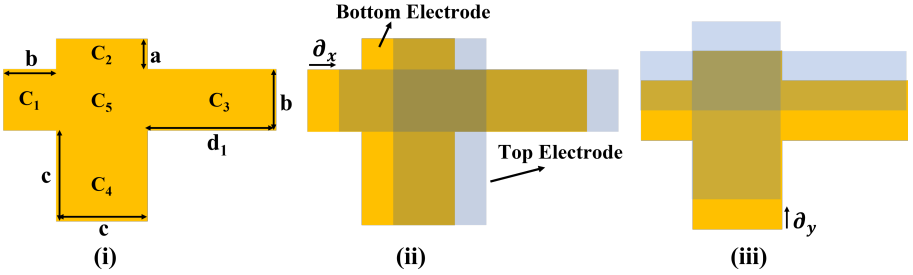


FIGURE 3.2: 2-D schematic of the unit pixel of E-CaP. (a) Initial position. (b) Displacement of the top electrode with respect to the bottom electrode in the x-direction. (c) Displacement of the top electrode with respect to the bottom electrode in the y-direction

overlap areas of C_1, C_2, and C_4 change. With displacement "d_x," the overlap area of C_1 changes from A_1 to A_1new, and the new capacitance is:

$$C_{1new} = \frac{\varepsilon_0 \varepsilon_r A_{1\text{new}}}{d} = \frac{\varepsilon_0 \varepsilon_r b\,(b - d_x)}{d} \tag{3.2}$$

The capacitance change (ΔC_1) for C_1 is then:

$$\Delta C_1 = C_1 - C_{1\text{new}} = \frac{\varepsilon_0 \varepsilon_r b}{d} d_x \tag{3.3}$$

Similarly, the changes for the remaining capacitors are:

$$\Delta C_2 = \frac{\varepsilon_0 \varepsilon_r a}{d} d_x, \quad \Delta C_4 = \frac{\varepsilon_0 \varepsilon_r c}{d} d_x, \quad \Delta C_5 = 0 \tag{3.4}$$

Thus, the overall change in capacitance for $d_x < 0.1$ cm is:

$$\Delta C_T = \frac{\varepsilon_0 \varepsilon_r (a + b + c)}{d} d_x \tag{3.5}$$

Similarly, when d_x ranges between 0.1 cm and 0.15 cm (i.e., $0.1 \leq dx < 0.15$cm), the overlapping area corresponding to C_2, C_4, and C_5 changes, but the total resulting change in capacitance remains the same as given in Equation 3.5. Similarly, the total capacitance change in the displacement region of $0.15 \leq dx < 0.45$ cm is given by the following equation:

$$\Delta C_T = \frac{\varepsilon_0 \varepsilon_r b}{d} d_x \tag{3.6}$$

Therefore, it can be concluded that in the displacement region up to 0.45 cm, the change in capacitance is determined by two different equations ((3.5) and (3.6)). After the displacement of 0.45 cm, the overlapping area between the top and bottom electrodes is zero, and no further capacitance formation occurs.

Similarly, the capacitance change due to displacement (d_y) in the y-axis is defined

by the following set of equations:

$$\Delta C_T = \frac{\varepsilon_0 \varepsilon_r (b + c + d_1)}{d} d_y, \quad 0 \leq d_y \leq 0.1\,\text{cm} \tag{3.7}$$

$$\Delta C_T = \frac{\varepsilon_0 \varepsilon_r c}{d} d_y, \quad 0.1 \leq d_y \leq 0.3\text{cm} \tag{3.8}$$

However, the displacement in the xy plane also results in the compression (d_z) of the dielectric layer. Hence, the effect of the dielectric compression on capacitance change is accommodated in the following equations. The initial capacitance of C_{1z} is given as:

$$C_{1z} = \frac{\varepsilon_0 \varepsilon_r A_1}{d} = \frac{\varepsilon_0 \varepsilon_r b^2}{d} \tag{3.9}$$

Given that the displacement (d_x) in the x-direction also results in the compression (d_z) of the dielectric layer, the new capacitance is formulated as:

$$C_{1z\text{new}} = \frac{\varepsilon_0 \varepsilon_r A_{1z\text{new}}}{d - d_z} = \frac{\varepsilon_0 \varepsilon_r b\,(b - d_x)}{d - d_z} \tag{3.10}$$

The corresponding change in capacitance for C_1 is:

$$\Delta C_T = C_{1z} - C_{1z\text{new}} = \frac{\varepsilon_0 \varepsilon_r b^2}{d} - \frac{\varepsilon_0 \varepsilon_r b(b - d_x)}{d - d_z} \tag{3.11}$$

$$\Delta C_T = \frac{\varepsilon_0 \varepsilon_r b(d d_x - b d_z)}{d(d - d_z)} \tag{3.12}$$

Similarly, incorporating the capacitance change for the other associated lumped capacitors (Figure 3.2), the total capacitance variation is expressed as:

$$\Delta C_T = \frac{\varepsilon_0 \varepsilon_r (d\,(a + b + c)\,d_x - A_T d_z)}{d(d - d_z)}, \quad 0 \leq d_x \leq 0.1\text{cm} \tag{3.13}$$

$$\Delta C_T = \frac{\varepsilon_0 \varepsilon_r (b d d_x - A_T d_z)}{d(d - d_z)}, \quad 0.15 \leq d_x \leq 0.45\text{cm} \tag{3.14}$$

where A_T is the total overlap area of capacitors in the initial state. Similarly, the displacement (d_y) in the y-direction also results in the compression (d_z) of the dielectric layer. Thus, the capacitance change is given by

$$\Delta C_T = \frac{\varepsilon_0 \varepsilon_r \left(d\left(b + c + d_1\right) d_y - A_T d_z\right)}{d\left(d - d_z\right)}, \quad 0 \leq d_y \leq 0.1\text{cm} \tag{3.15}$$

$$\Delta C_T = \frac{\varepsilon_0 \varepsilon_r (c d d_x - A_T d_z)}{d(d - d_z)}, \quad 0.1 \leq d_y \leq 0.3\text{cm} \tag{3.16}$$

Therefore, for the direction-sensitive capability, the dimension "a" should not be equal to "d_1" (i.e., $a \neq d_1$) (equations (3.13) and (3.15)), and dimension "b" should not equal "c" (i.e., $b \neq c$) (equations (3.14) and (3.16)).

Finally, the dimensions of the asymmetric electrode are chosen so that the minimum change is detectable with the associated interfacing circuitry. Although these dimensions can be scaled provided that the circuitry has a resolution in the attofarad range or lower, scaling introduces trade-offs. Increasing the electrode dimensions beyond the reported values enlarges the overall device footprint. Conversely, scaling down the dimensions by a factor of ten decreases the minimum detectable change from 1.468 fF to 0.1468 fF, thereby demanding higher circuit resolution. At the same time, scaling up the dimensions by ten times increases the minimum detectable change to 14.868 fF. However, the device footprint of E-CaP will increase by 90 times. Thus, optimization requires balancing electrode dimensions, circuit resolution, and device footprint for practical E-CaP implementation.

3.1.3 Fabrication Process Flow

The fabrication process of the flexible E-CaP array is divided into two main steps, viz., formation of PDMS μ-mesh using SU-8 μ-mold and fabrication of asymmetric electrode structure, as shown in Figure 3.3. Later, the μ-mesh and electrodes are

easily assembled to form E-CaP. The SU-8 μ-mold is fabricated on the standard silicon substrate. The μ-mold consists of an array with hexagonal pillars of height $\approx$500 μm, as shown in Figure 3.4. For improved direction-sensitive epidermal mapping, the bottom electrode is fabricated on a thinner PET sheet compared to the top electrode. The thin layer of liquid paraffin is spin-coated on the SU-8 μ-mold, which facilitates the removal of μ-mesh from the μ-mold in a later stage. For the formation of μ-mesh, the known volume of PDMS is edge drop-casted on the base of

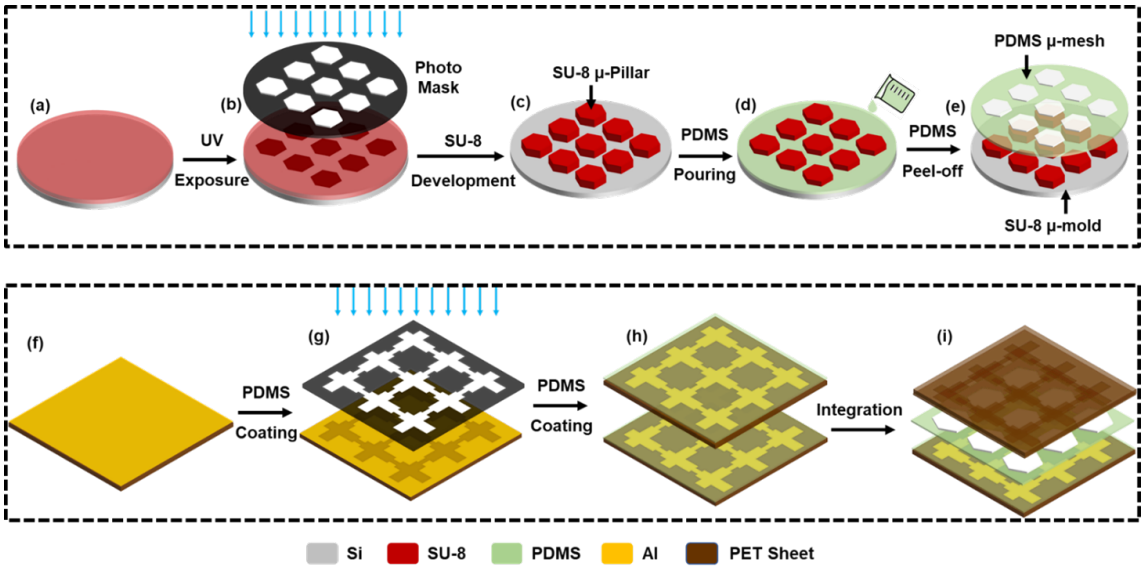


FIGURE 3.3: Fabrication process. (a) Spin coating of SU-8 (500 μm) on Si substrate followed by pre-exposure bake (at 100 °C for 2.5 min). (b) Exposure (E = 25 mJ/cm^2) of SU-8 using photomask. (c) Development of SU-8 after post-exposure bake (at 105 °C for 5 min) for the formation of μ-mold. Thereafter, spin coating of the thin layer of liquid paraffin is used to facilitate the release of PDMS μ-mesh in the subsequent step. (d) Pouring of the known volume of PDMS at the edge of the substrate to fill to a certain height of SU-8 micropillars. (e) Peeling-off PDMS μ-mesh from SU-8 μ-mold. The SU-8 μ-mold can be reused for batch fabrication of PDMS μ-mesh. (f) Deposition of aluminum ($\sim$100 nm) on two different thicknesses of PET sheet using thermal evaporation. (g) Exposure and patterning of a 3 $\times$ 3 asymmetric capacitive electrode array. (h) Coating of the thin layer of PDMS (5 μm at 8 k r/min) to facilitate proper adhesion in the next step. Prior to spin coating of a thin layer of PDMS, the PET sheet is treated with the diluted amine-PDMS linker. The amine linker forms a urethane linkage on the PET sheet, which facilitates the bond formation with the PDMS. (i) Assembling of PDMS μ-mesh and 3 $\times$ 3 asymmetric capacitive electrode array followed by curing (at 95 °C for 90 min) to form E-CaP.

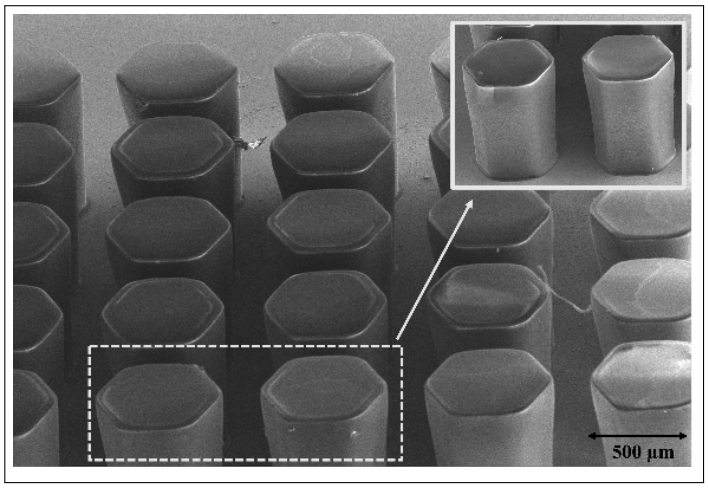


FIGURE 3.4: SEM image of the μm-mold of SU-8. The inset shows the gap and height of the hexagonal μm-pillar. The μm-mold can be reused for a batch fabrication

μ-mold. The viscoelasticity of PDMS allows the solution to spread uniformly across the SU-8 μ-mold. The mold is placed in a desiccator to remove trapped bubbles and subsequently cured at 95 for 90 min. Finally, the freestanding PDMS μ-mesh is easily peeled off from the μ-mold.

After that, the PDMS μ-mesh is gently rinsed in acetone and dried in an oven at 70 °C. For the formation of asymmetric electrodes, PET sheets of two different thicknesses are deposited with aluminum (≈100 nm) using thermal evaporation. Then, the metal-deposited PET sheet is mounted on a flat glass substrate using double-sided adhesive tape. Next, the S1813 positive photoresist is spin-coated on a metal-cladded sheet to define the pattern of asymmetric electrodes using lithography. The aluminum metal electrodes are etched using buffered Al etchant $H_3PO_4 + CH_3COOH + HNO_3 + H_2O$ (18:1:1:1) solution. This specific etchant does not attack the PET sheet during etching. For the integration of freestanding PDMS μ-mesh with the asymmetric electrodes for the formation of E-CaP, a thin layer of PDMS is spin-coated on the upper and bottom electrodes. Since the adhesion of cured PDMS (μ-mesh) is poor with a fabricated electrode array, the

spin coating of the thin layer of pre-cured PDMS (5 μm at 8000 rpm) enables proper adhesion when the assembly is arranged and cured. Prior to spin coating of the thin layer of PDMS, the PET sheet is treated with the diluted amine-PDMS linker. The amine linker forms a urethane linkage on the PET sheet, which facilitates the bond formation with the PDMS. The amine-PDMS linker increases the bonding strength around 400 kPa [126].

3.1.4 Results and Discussion

The fabricated prototype E-CaP unit (device shown in Figure 3.1; experimental setup in Figure 3.7) is first simulated and then tested to map the response arising from the relative displacement between top and bottom asymmetric electrodes. This displacement depends on the porosity of the PDMS μ-mesh, which in turn is controlled by the size of the SU-8 μ-pillars (Figure 3.4). The maximum achievable porosity in the PDMS μ-mesh can be estimated using:

$$\text{porosity}\% = \frac{\text{volume of hexagon}}{\text{volume of PDMS layer}} \times 100 \tag{3.17}$$

The theoretical porosity of $\approx$ 69% is achieved when the side of the hexagon is 0.5176$\times$ the side of a square. However, this condition is impossible to achieve since it implies neighbouring hexagons touching each other. The touching hexagons break the continuity of the PDMS layer, and it ceases to exist as a μ-mesh. Therefore, a gap of 0.2 mm is introduced between the adjacent hexagons, and the porosity achieved is 48%. The stress distribution on the PDMS μ-mesh at this configuration is shown in Figure 3.5(a). The gap less than 0.2 mm (more porosity) causes uneven stress distribution, as shown in Figure 3.5(b). Similarly, decreasing the porosity (decreasing the size of hexagons) compromises the shear displacement and

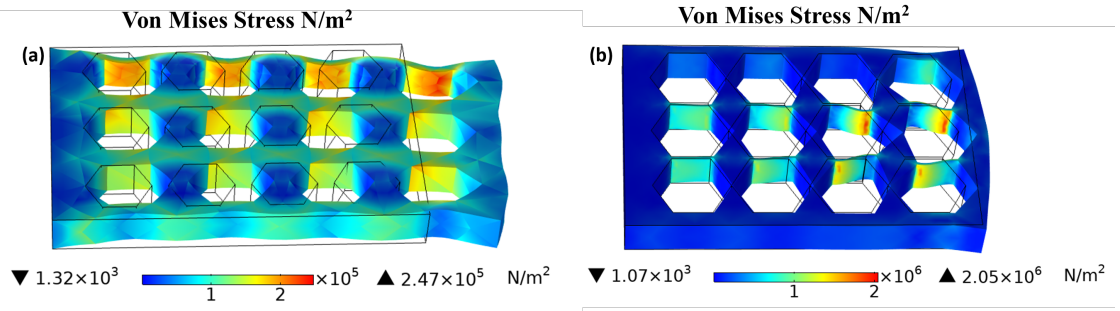


FIGURE 3.5: (a) Stress distribution in the PDMS μ-mesh at a gap of 0.2 mm between adjacent hexagons. (b) Stress distribution in the PDMS mesh when the gap is less than 0.2 mm. The stress generated is uneven throughout the PDMS μ-mesh.

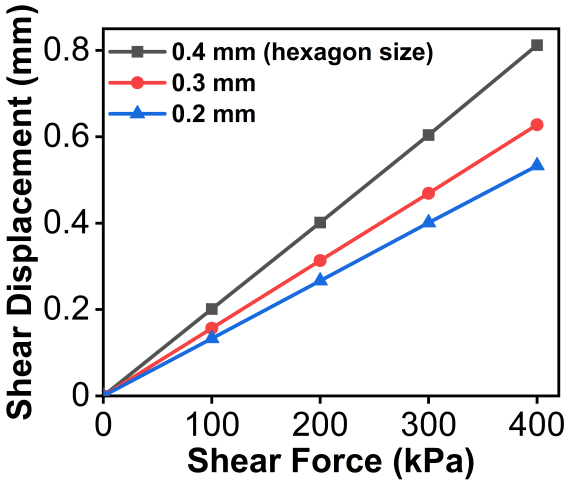


FIGURE 3.6: Shear displacement generated in the PDMS μ-mesh at different dimensions of hexagons due to shear force. The decrease in volume of the hexagon reduces the porosity, which in turn reduces the sensitivity of the device.

thus the sensitivity of the E-CaP, as shown in Figure 3.6. In addition to the lateral geometry, the 500 µm height corresponds to the thickness of the µ-meshed PDMS layer defined by the SU-8 mold. Thinner dielectric layers reduce mechanical amplification and strain sensitivity, whereas thicker layers beyond this limit are constrained by SU-8 processing reliability. Hexagonal microstructures are selected because they provide high packing efficiency while maintaining structural continuity of the PDMS μ-mesh. This geometry enables higher achievable porosity for a given

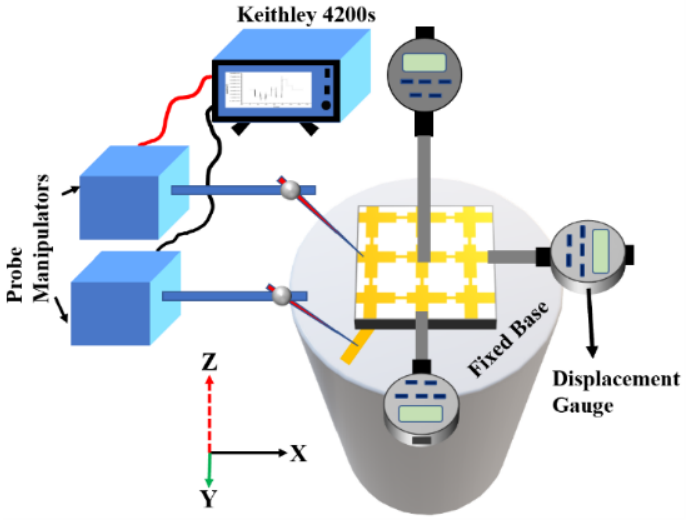


FIGURE 3.7: Experimental setup for the measurement of the vectored response of fabricated E-CaP

spacing, thereby improving shear displacement and directional sensitivity of the E-CaP. Therefore, the combination of hexagonal geometry, 0.2 mm spacing, and 500 µm SU-8 mold thickness provides a balance between porosity, mechanical stability, and fabrication feasibility.

The complete experimental setup is shown in Figure 3.7. Three displacement gauges are connected to measure the relative displacement of the top electrode with respect to the bottom electrode in the x, y, and z directions. The cumulative vectored response (i.e., $\vec{d}$ in pF/mm) of the E-CaP is obtained using a parametric analyzer (Keithley 4200-SCS) and displacement gauges. The measured rates of change of capacitance are 1.341, 2.007, and 8.750 pF/mm in the x, y, and z directions, respectively. In vector form, it is represented as follows:

$$\vec{d} = 1.341\hat{\imath} + 2.007\hat{\jmath} + 8.750\hat{k} \tag{3.18}$$

where $\hat{\imath}$, $\hat{\jmath}$, $\hat{k}$ are the unit vectors in the x, y, and z-directions, respectively. The capacitance values in the x and y axes can overlap, but the slopes (capacitance change per mm) are different. This capacitance change per millimeter defines the

direction of movement and is crucial for determining the vector response. To map the direction of stress-induced motion when E-CaP is mounted on the limb, the previous value of capacitance must be retained. The difference in the previous and present values represents the rate of change of capacitance. This rate of change is direction sensitive due to the asymmetrical design of the E-CaP. Figure 3.8 represents the real-time response of the E-CaP, whereas the inset shows the transition noise. The transition noise arises due to mechanical inertia in the viscoelastic PDMS μ-mesh. This mechanical inertia results in a transient between the transition of two stable capacitive states. The following expression is used to calculate the repeatability "R" of the E-CaP [127]:

$$R\% = \frac{\pm\sqrt{(C_1 - C_m)^2 + (C_2 - C_m)^2 + \cdots + (C_n - C_m)^2}}{2\,(n-1) \times C_m} \times 100 \tag{3.19}$$

where $C_1, C_2, \ldots, C_n$, are the n number of capacitive responses at the same stimuli, and Cm is the mean of these n capacitive values. The measurements are experimentally repeated around 80 times with the same stimuli. The response of E-Cap is highly repeatable with a deviation of only 0.37%.

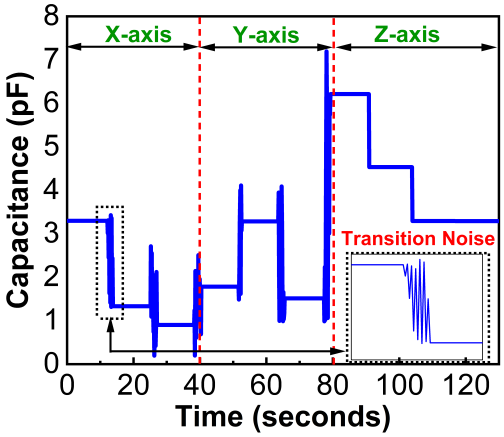
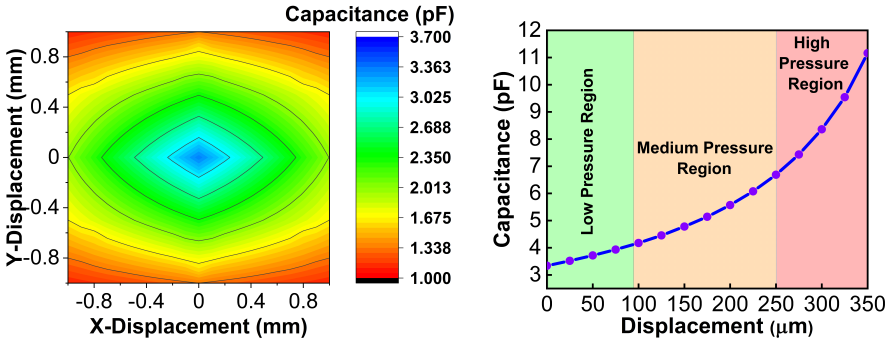


FIGURE 3.8: Real-time vectored capacitive response of E-CaP in global Cartesian coordinates. The inset shows the transition noise during the relative displacement of asymmetrical electrodes.

TABLE 3.1: Simulation Parameters

S.No.	Parameter	Value
1	Relative Permittivity	2.8
2	Young's Modulus	750 kPa
3	Poisson's Ratio	0.49
4	Electrode Overlap Area	0.075 cm^2
5	Thickness of Electrodes (Al)	50 nm

The E-CaP sensor array shown in Figure 3.1 is modeled using the ac/dc electrostatic module of COMSOL Multiphysics. In finite-element analysis (FEM), the top electrode array was specified with a terminal voltage of 1 V, while the bottom electrode was fixed and kept at ground potential. The sandwiched μ-mesh PDMS layer properties are specified in Table 3.1. Figure 3.9(b) shows the simulated spatial domain of the capacitive response to the pressure stimulus in the xy-direction. The nominal capacitance of E-CaP when there is no pressure stimulus (i.e., zero relative displacements) is ≈3.37 pF. The discrete data points corresponding to real-time capacitive response are mapped on this spatial domain. The simulated results yield the maximum linear range of ±0.8 mm in the corresponding xy-direction. The maximum linear range depends on the gap between adjacent hexagons of PDMS μ-mesh. The



(a) (b)

FIGURE 3.9: (a) Mapping of the simulated capacitive response of E-CaP in the xy spatial domain, defining the region of operation. (b) Mapping of the capacitive response of E-CaP in Z spatial domain, defining the region of operation.

maximum linear range of ±0.8 mm is obtained when the gap between the adjacent hexagons of the PDMS μ-mesh is 0.2 mm. Reducing the gap below 0.2 mm results in the uneven stress distribution in the μ-mesh (Figure 3.5). These discrete data points lie within the boundary of the spatial domain, defining the region of operation of E-CaP. The response to pressure stimuli in the z-direction is also shown in Figure 3.9(b). Table 3.2 compares the previously reported directional sensing strategies with the proposed E-CaP sensor.

TABLE 3.2: Comparison of Previously Reported Directional Tactile Sensing Approaches with the Proposed E-CaP Sensor.

Ref.	**Device Structure**	**Advantages**	**Limitations**
[120]	All-elastomer structure Varying μ-pillar height	High shear sensitivity High dynamic range No bump structure	In-plane wiring complexity Large routing area
[128]	Multilayer structure PDMS bump structure	Differential capacitive sensing 3-axis force measurement	Layer alignment complexity Complex fabrication process High circuit complexity
[121]	Solid dielectric layer SU-8 bump structure	Simple device architecture Easy fabrication Low circuit complexity	Limited shear compliance Reduced sensitivity Cell-to-cell variation
[123]	Two-capacitor structure	Improved spatial resolution Multi-axis detection	Low shear sensitivity Complex algorithm required
This Work	**μ-meshed PDMS dielectric** **Asymmetric design**	**Single-pixel directional sensing** **Minimal circuit complexity** **Batch fabrication**	**Larger device footprint**

3.1.5 Conclusion

In summary, a simple 3 × 3 epidermal asymmetric capacitive pixel (E-CaP) array was simulated and tested for its vectored response. The directional sensitivity of the E-CaP was characterized by measuring the rate of capacitance change, which quantifies the vectored strain response. The device fabrication involves two key steps: formation of an SU-8 μ-mold and fabrication of asymmetric electrodes. Notably,

the SU-8 μ-mold can be reused, facilitating batch fabrication and scalability. The nominal capacitance of the array is approximately 3.37 pF, with a capacitance change vector of $\vec{d} = 1.341\hat{i} + 2.007\hat{j} + 8.750\hat{k}$ pF/mm per unit displacement. The E-CaP effectively maps the entire vectored response associated with the movement domain of limbs.

3.2 Bimodal E-Skin for Human Motion Monitoring

Following the demonstration of the E-CaP array for direction-sensitive sensing in the previous section, this section introduces a magnetodielectric layer (MDL)-based bimodal device capable of both strain and proximity detection. Directional sensitivity provides valuable information about epidermal motion. However, the ability to concurrently detect contact strain and non-contact proximity adds another important modality for wearable devices. The proposed device employs a PDMS matrix embedded with magnetic nanoparticles and is implemented with a single capacitive readout. The sensor is integrated with dedicated circuitry and complemented by a power-saving algorithmic strategy to ensure efficient system operation. Experiments are carried out to validate the bimodal performance, and its applicability is demonstrated in limb-movement monitoring tasks.

3.2.1 Introduction

Human skin is inherently multisensory, integrating mechanoreceptors, nociceptors, and thermoreceptors to perceive and respond to diverse external stimuli simultaneously [129]. Therefore, flexible electronic skin (E-skin) featuring multisensory

qualities becomes an essential technological platform for detecting and quantifying external stimuli [130, 131]. Earlier E-skin approaches often relied on single-modality sensors integrated in parallel, which restricted their ability to capture complex, multimodal stimuli [132, 133]. Therefore, equipping next-generation E-skins with multiple sensing capabilities has become a central objective [17].

Recently, studies reported on bimodal E-skins that emulate mechanoreception coupled with thermoreception [134] or mechanoreception integrated with hygroreception [135], or thermoreception combined with hygroreception [136]. However, devices that simultaneously sense strain and proximity remain scarce, despite their importance in robotics and prosthetics. In practice, autonomous systems require both modalities to interact safely with their surroundings. For example, an artificial skin designed for visually impaired individuals should not only detect an approaching object and determine whether it is metallic or non-metallic, but also perceive the strain induced upon contact [137, 138, 139].

In most reported works, strain sensing and proximity sensing in E-skin are accomplished by combining two separate sensors [140]. Such approaches demand the integration of different single-modality sensors on heterogeneous substrates. It often requires complicated layouts (e.g., open mesh and serpentine interconnect) to eliminate false mechanical strain effects [140]. Notably, the aforementioned approaches also require different readout mechanisms for detection that increase the space occupied by these sensors, hence making E-skin bulky. A single readout-based fringing field capacitive sensor has been recently investigated for bimodality (strain and proximity sensing) [141]. However, the proximity response range is limited to just a few millimeters (1.4 mm) and has low sensitivity. The higher strain sensitivity is achieved at the cost of process complexity in fabrication. Silicon molds are used directly for micro-structuring of the dielectric layer for enhanced strain sensitivity that increases fabrication complexity (especially molding, peel-off, and transferring

the active layer) and cost. Thus, there remains a need for a single-platform, process-efficient bimodal E-skin with an extended proximity range and high sensitivity.

This section reports on a magneto-dielectric layer (MDL)-based bimodal (strain and proximity) sensing device with a single capacitive readout. Introducing MDL (nanoparticles blended homogeneously in polydimethylsiloxane) in the design enhances the sensitivity $S_{\mathrm{ST}} \approx$ 4x-times and $S_{\mathrm{Prox}} \approx$ 1.5x-times and widens the dynamic range (from 6 to 20 mm). Nanoparticles within the PDMS redistribute differently under strain loading, improving strain responsivity compared to conventional PDMS-based interdigitated electrodes (P-IDEs). Additionally, spiral electrodes integrated with the MDL (M-IDEs) enhance the overall electric field density, which significantly improves proximity performance ($S_{\mathrm{Prox}} = 93.23$ fF/mm, with a detection range up to 21 mm for conducting objects). Moreover, this configuration enables discrimination between conducting and non-conducting targets. To mimic curvilinear body surfaces, a 3D-printed test platform is employed to generate calibration curves under bending conditions. Finally, the fabricated skin-inspired device is validated by tracking limb movements, demonstrating its potential for next-generation prosthetic and robotic applications.

3.2.2 Device Concept and Design

Figure 3.10 illustrates the bimodal sensing concept of the M-IDE. The strain-sensing mechanism is shown in Figure 3.10(a–b), while the expected proximity response is summarized in Figure 3.10(c–d). For strain sensing, the capacitance of the device is governed by the effective dielectric constant of the magnetodielectric layer (MDL) and the electrode geometry:

$$C = \varepsilon_{\mathrm{eff}} \times (\text{geometric constant}). \tag{3.20}$$

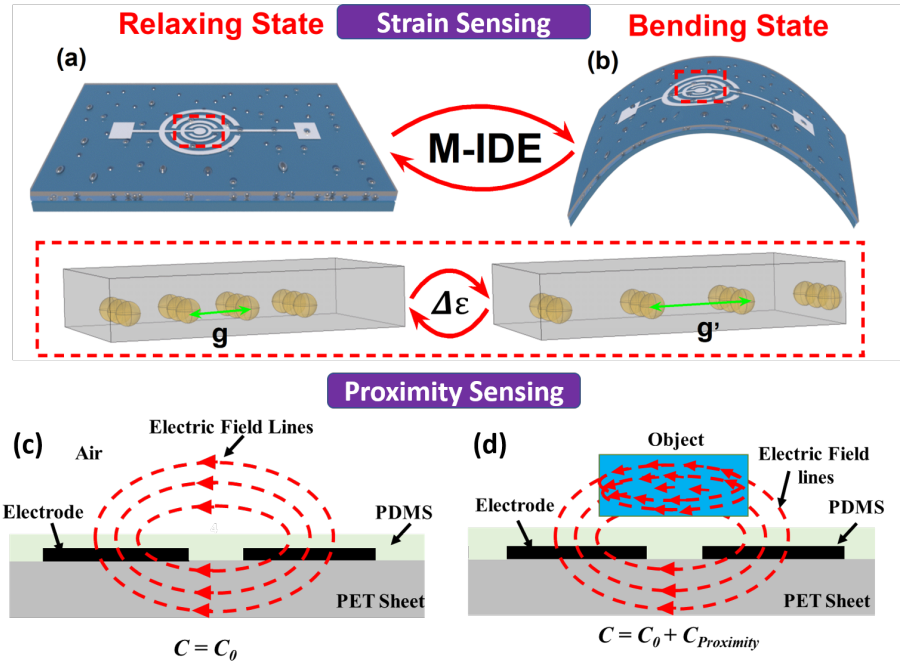


FIGURE 3.10: Concept of the bimodal M-IDE sensor. (a–b) Strain-sensing mechanism: bending alters inter-particle separation ($g \rightarrow g'$) within the MDL, reducing the effective dielectric constant and capacitance. (c–d) Proximity-sensing mechanism: approaching objects perturb fringing fields, generating additional capacitance (C_{prox}). Together, these effects enable simultaneous strain and proximity detection with a single capacitive readout.

In the relaxed state, the fringing fields between the interdigitated electrodes dominate, and the capacitance of the M-IDE is nearly identical to that of a conventional IDE with PDMS as dielectric (P-IDE). When the device is bent, the average inter-particle separation increases ($g' > g$). This redistribution alters the local electric field distribution, causing nanoparticles to behave as isolated capacitive elements. The reduction in effective dielectric constant leads to a measurable decrease in capacitance. The capacitance variation with MDL geometry can be empirically expressed as:

$$C = f(t, g) \propto \varepsilon_P \left(\frac{t}{g}\right), \tag{3.21}$$

where t is the effective thickness of the MDL and g represents the average particle separation. Thus, as bending increases and $g' \rightarrow g$, the field separation improves,

leading to enhanced strain sensitivity. For proximity sensing, the spiral IDE geometry enhances fringing field density and extends the detection range. When an object enters the vicinity of the electrodes, the local field distribution is perturbed, resulting in a measurable change in capacitance. The magnitude of this change depends on the distance, position, and nature of the object.

3.2.3 Finite Element Modeling

To validate the proposed working principle, two device classes are studied: P-IDEs (without MDL) and M-IDEs (with MDL). Figure 3.11(a) shows the schematic of the M-IDE with PET substrate, spiral IDEs, and the magnetodielectric layer (MDL). Finite element simulations (COMSOL Multiphysics) are performed on a representative two-electrode structure to quantify capacitance variation with inter-particle separation g. As bending increases, particle separation increases ($g' > g$), which modifies the effective dielectric constant (ε_{eff}) and produces a measurable reduction in capacitance. Figure 3.11(b) shows the normalized capacitance change $|\Delta C/C_0|$ with

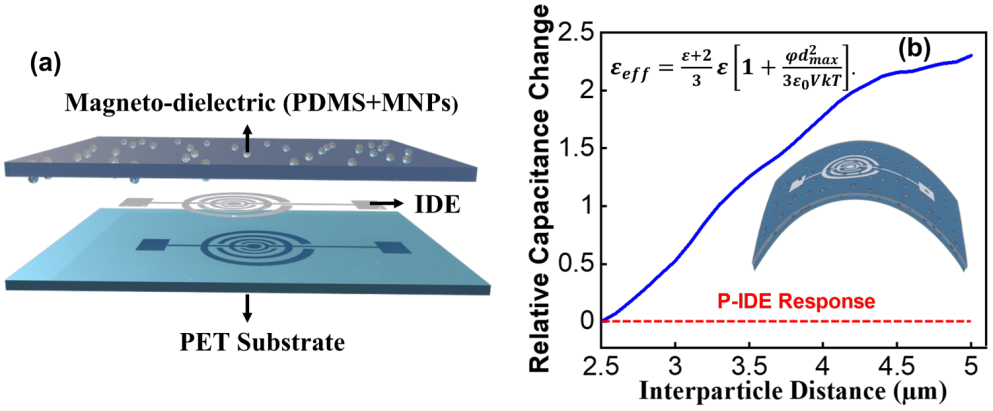


FIGURE 3.11: (a) Schematic of the M-IDE device showing different layers. A thin flexible PET sheet (150 μm) is used as the substrate, with interdigitated electrodes (IDEs) fabricated on top. The sensing layer consists of magnetic nanoparticles (MNPs) blended in PDMS. (b) Simulation results showing the capacitance change as a function of separation, correlated with the effective dielectric constant.

increasing g, confirming this trend. The results are consistent with the analytical relations introduced earlier (Equation 3.20–3.22). Notably, these findings confirm that the M-IDE response is primarily determined by the average inter-particle separation g within the MDL, which dictates ε_{eff} and thereby governs the strain-sensing behavior (Figure 3.11(b)).

3.2.4 Fabrication Process Flow

Figure 3.12 illustrates detailed steps for bimodal flexible sensor fabrication. Initially, a thin layer (100 nm) of aluminum is deposited on a polyethylene terephthalate (PET) sheet using an e-beam evaporator (HHV ATS 500). Aluminum-coated PET sheet is then lithographically patterned to define the spiral IDEs (Figure 3.12(b)). Two different devices are fabricated for comparison. In the reference device (P-IDE), PDMS is spin-coated over the patterned electrodes to act as the dielectric layer. In the proposed device (M-IDE), the dielectric consisted of a magnetodielectric layer (MDL), prepared by blending magnetic nanoparticles homogeneously in PDMS, which is then spin-coated on the patterned electrodes. For the MDL preparation, Fe_3O_4 magnetic nanoparticles (8 wt%) are dispersed in the PDMS prepolymer using mechanical stirring followed by controlled sonication to obtain a homogeneous dispersion. The curing agent is then added in a 10:1 base-to-curing-agent ratio and mixed thoroughly to maintain uniform filler distribution. The mixture is subsequently degassed to remove trapped air bubbles before spin-coating on the patterned electrodes. The incorporation of Fe_3O_4 nanoparticles increases the effective dielectric permittivity of the composite layer through interfacial (Maxwell–Wagner–Sillars) polarization at the nanoparticle–polymer interface, thereby enhancing the capacitive sensitivity of the device. Furthermore, during mechanical deformation

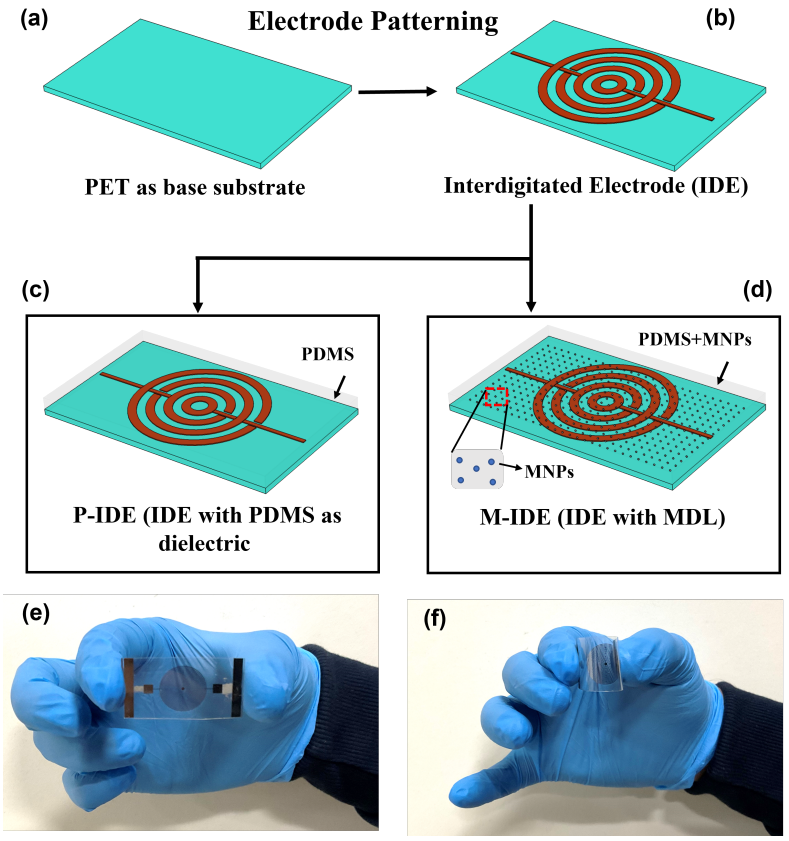


FIGURE 3.12: Fabrication process of P-IDE and M-IDE devices. (a–b) Lithographic patterning of IDEs on Al-coated PET substrates. (c) P-IDE prepared by spin-coating PDMS. (d) M-IDE is fabricated by spin-coating MDL (PDMS + magnetic nanoparticles). (e–f) Optical images of M-IDE in relaxed and bent states.

the interparticle spacing within the Fe_3O_4–PDMS composite changes, which modulates the local electric field distribution and contributes to the observed capacitance variation. Both devices were subsequently cured in an oven at 80°C for about 2.5 hours. This controlled preparation process ensures uniform nanoparticle dispersion and reproducible dielectric properties of the magnetodielectric layer. Optical images of the fabricated M-IDE in relaxed and bent states are shown in Figure 3.12(e–f). Commercially available materials (PET sheets, PDMS, and chemicals) are used throughout the experiment for device fabrication. All devices are fabricated with identical dimensions, with an electrode width and spacing of 100 µm, to ensure a fair comparison between P-IDE and M-IDE. The proposed device is scalable and

tailorable for miniaturized sensing applications, but faces a fundamental trade-off. As the device is miniaturized, its sensitivity decreases. Conversely, a larger device area increases sensitivity at the cost of a larger footprint.

3.2.5 Results and Discussion

3.2.5.1 Strain Sensing Performance

Electromechanical characterization of the devices is carried out using a customized 3D-printed setup (shown in the inset of Figure 3.14 (a)), which allowed systematic bending at radii of curvature (ROC) ranging from 2 mm to 22 mm. Both P-IDE and M-IDE devices (with electrode width = 100 μm and spacing = 100 μm) are mounted sequentially on the 3-D setup, and electrical characterization is performed using a high-end parameter analyzer (Keithley 4200s-SCS). Figure 3.13(a) compares the absolute relative capacitance change in both devices. As shown in Figure 3.13(b), the relative capacitive change in M-IDE is consistently higher than that of the P-IDE. Under bending conditions, the dynamically changing inter-particle separation ($g \rightarrow g'$) results in a four-fold enhancement in strain-sensitivity ($S_{ST} \approx$ 4x-times) at lower radii of curvature in M-IDE devices. At a larger radius of curvature, the capacitance change is approximately identical in both devices, as capacitance behavior is dictated by the separation 'g'. Thus, the efficacy of the MDL incorporation in enhancing strain responsivity is clearly established when comparing M-IDE and P-IDE. Furthermore, no significant capacitive change is found in P-IDE for ROC $>$ 10 mm, whereas the M-IDE responds effectively down to ROC = 6 mm. This demonstrates that the MDL tailors strain sensitivity and expands the working range from 20 mm to 6 mm. Here, M-IDE's working range is divided into three distinct sensitivity regimes: two linear regions and a nonlinear transition region. The first region offers a linear

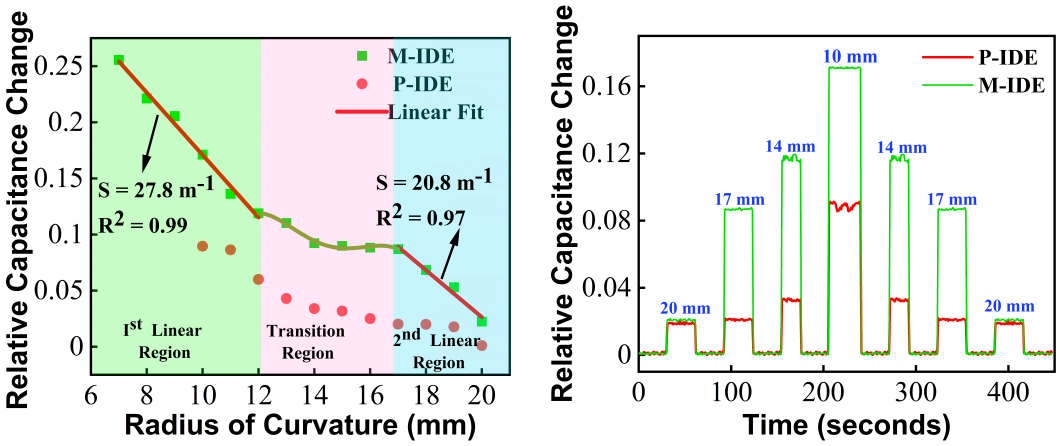


FIGURE 3.13: Comparison of strain sensing between P-IDE and M-IDE. (a) M-IDE shows enhanced sensitivity and a greater working range (6–20 mm) compared to P-IDE. M-IDE working range is divided into three distinct sensitivity regimes: two linear regions and a nonlinear transition region with the highest sensitivity of $27.8\,\mathrm{m}^{-1}$ (b) Step response at different radii of curvature (ROCs) that correspond to varying separation within MDL.

relationship between $\left|\frac{\Delta C}{C_o}\right|$ and ROC with the sensitivity ($\mathrm{S} = \delta\left(\Delta \mathrm{C}/\mathrm{C}_0\right)/\delta\mathrm{ROC}$) of $27.8\mathrm{m}^{-1}$ and an R^2 (coefficient of linear fit) value of 0.99. Sensitivity enhancement corresponds to a newly automated dynamic position of nanoparticles. The second region shows a nonlinear transition regime between the first and third linear regions. This behaviour can be attributed to the small net gap variation between particles. Finally, the third region shows a linear relationship with a sensitivity of 20.8 m $^{-1}$ and an R^2 value of 0.97. Notably, no distinct sensing regions are observed in P-IDE. The response of P-IDE is a function of the electrode's gap variation only at different bending radii. In contrast, in M-IDE the relative capacitance change arises from the synergistic effect of both dynamic nanoparticle separation and electrode gap variation. This combined mechanism leads to enhanced sensitivity and an expanded working range, confirming the role of the MDL.

Figure 3.14(a) illustrates the time response of M-IDE for one bending cycle. Response and relaxation time, as shown in Figure 3.14(b-c), are measured by cyclically

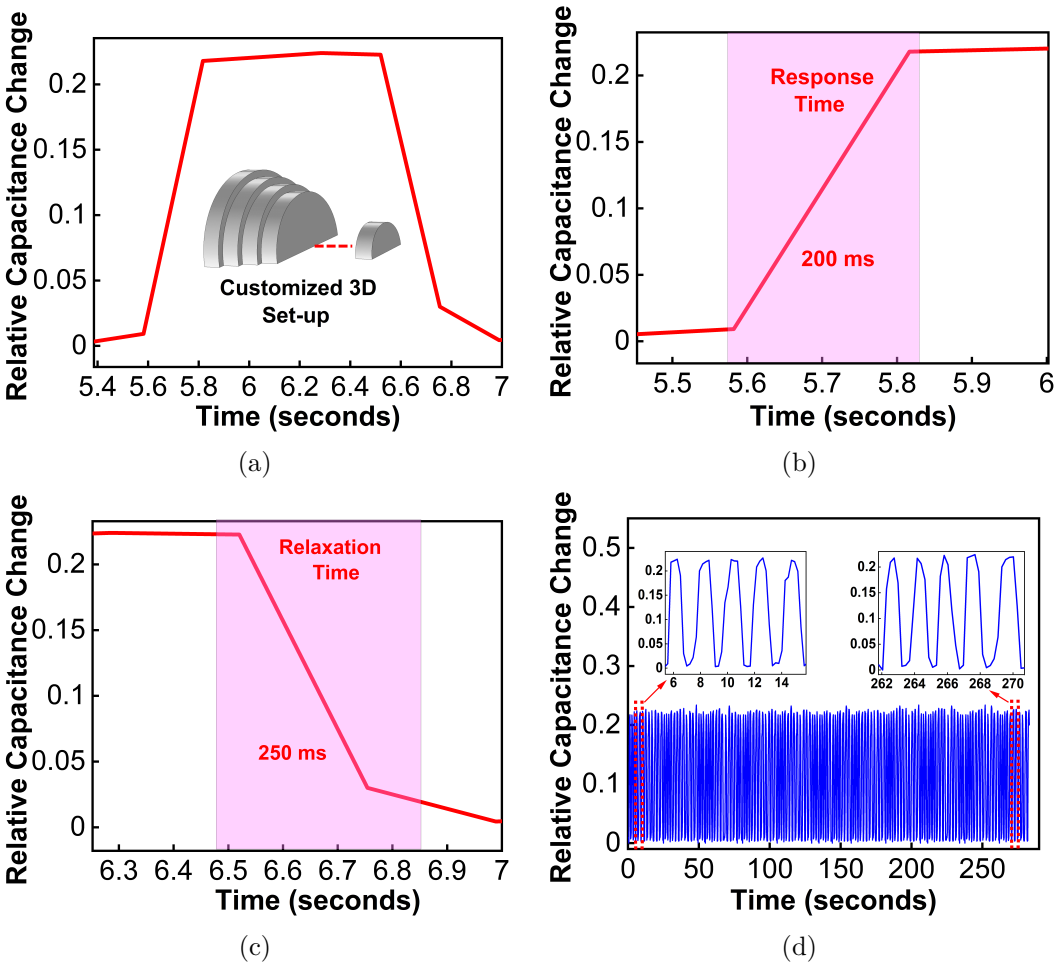


FIGURE 3.14: Dynamic response of M-IDE. (a) Strain response at ROC = 8 mm for one cycle. (b–c) Response and relaxation times measured as 200 ms and 250 ms, respectively. (d) Repeatability over 1000 bending cycles at ROC = 8 mm, showing highly stable and durable performance with consistent amplitude. Insets show magnified start and end cycles, confirming excellent reliability.

bending and releasing the device. The response time for the as-prepared device is found to be 200 ms, while the relaxation time is 250 ms, which is in good accordance with the past reports. The response time is mainly determined by the data acquisition system, how fast or slow dynamic strain is applied, and the nature of the strain-sensitive film. In M-IDE, the response time can be improved by using a relatively thinner PET substrate, micro-structuring the magneto-dielectric layer (improves viscoelastic behavior and reduces friction between nanoparticles and the

PDMS), and the relatively faster strain applying setup [142]. The relatively lower relaxation time demonstrates quick recovery, making the device suitable for real-time applications such as limb motion tracking. Finally, device longevity is examined to evaluate durability and repeatability, which are critical for practical use. Figure 3.14(d) shows the repeatability test of M-IDE devices measured at a constant ROC = 8 mm over 1000 cycles. The response remained highly consistent with nearly constant amplitude. The overlap between the initial and final cycles, highlighted in the inset, confirms excellent repeatability and stability, thereby demonstrating the endurance of the proposed M-IDE devices. The M-IDE sensor exhibits signal variation within ±2.5% during 1000 loading cycles, thereby demonstrating the endurance and structural robustness of the proposed device.

3.2.5.2 Proximity Sensing Performance

To corroborate the dual-sensing modality of the skin-inspired device, the proximity response of both P-IDE and M-IDE devices is evaluated and compared. Proximity measurements are carried out using a custom-made stage (inset of Figure 3.15(c)), with 0.0 mm as the point of contact. In the M-IDE, contactless proximity sensing occurs due to the enhanced fringing fields emanating from the IDE structures. During experiments, capacitance is continuously recorded with respect to object position using the Keithley analyzer. First, a 20 mm thick non-conducting object is moved away from the device in steps of 1 mm using a high-precision micrometer attached to the Z-stage. As the object moves farther, capacitance decreases due to the reduction in the electric field strength. Figure 3.15(a) shows the proximity sensing response for a non-conducting object. In the case of conducting objects, as shown in Figure 3.15(b), the MDL in M-IDE results in high electric-field confinement, which enhances the S_{Prox} = 1.5x times greater than P-IDE. The capacitance change is substantially

greater close to the device's surface in both devices, with a detectable range of 21 mm. However, unlike the P-IDE, the M-IDE could clearly distinguish between conducting and non-conducting objects. This distinction is highlighted in Figure 3.15(d). Conducting objects, such as copper, produced a much larger capacitance shift compared to non-conducting objects. The sensitivity of the M-IDE to conducting objects is found to be approximately 23× higher than for non-conducting ones.

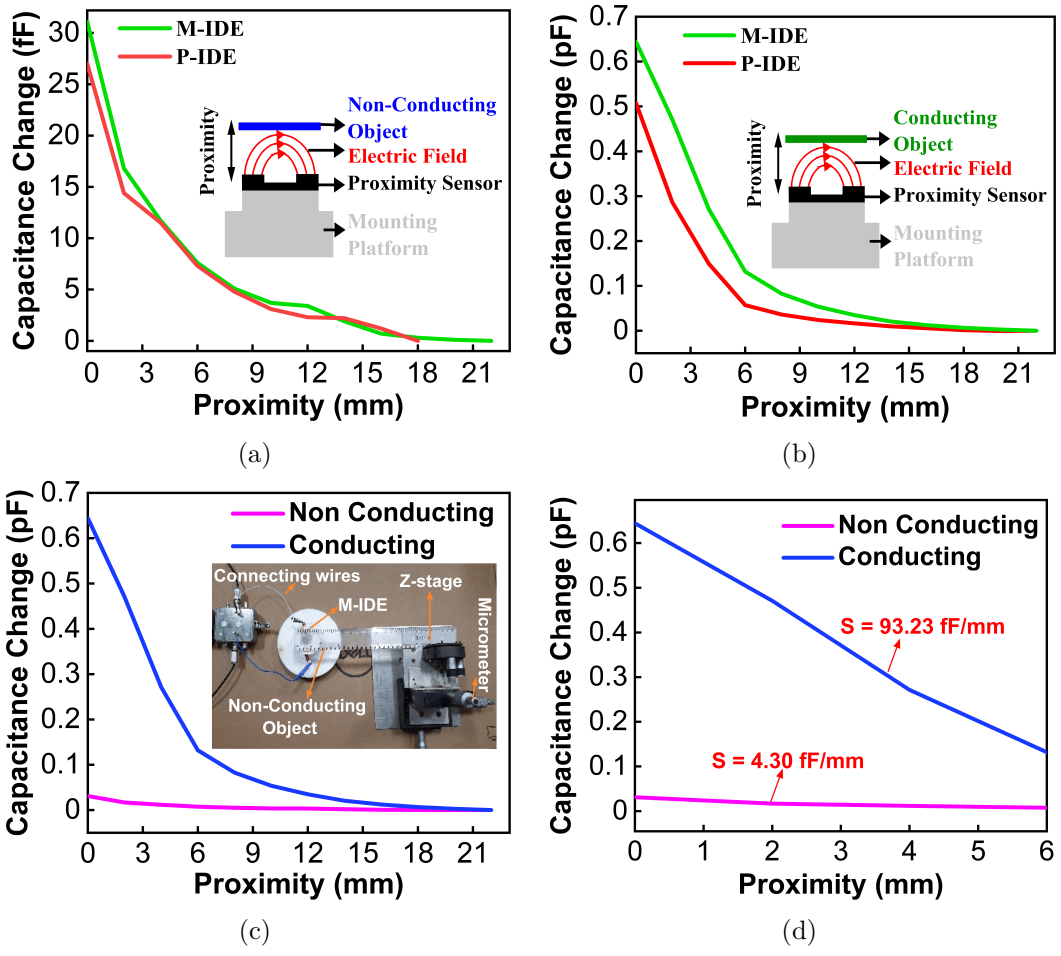


FIGURE 3.15: Proximity-sensing performance of M-IDE. (a) Sensitivity (S_{Prox})) to non-conducting objects is 1.5× higher than P-IDE. (b) Response of the M-IDE to conducting objects at varying proximity distances. (c) Universal proximity response of M-IDE for both conducting and non-conducting objects. Sensitivity for conducting objects is found to be ∼23× higher, highlighting the M-IDE's strong metal-detection capability. The inset shows the experimental setup with 0.0 mm defined as the point of contact. (d) Short-range proximity sensitivity in M-IDE for conducting objects is 93.23 fF/mm, significantly higher than 4.30 fF/mm for non-conducting objects.

At short range, the M-IDE achieved a sensitivity of 93.23 fF/mm for conducting objects, compared to only 4.30 fF/mm for non-conducting objects. Thus, by analyzing the slope of the capacitance–distance curve, the device can readily identify the nature of approaching objects. This multimodal sensing capability significantly enhances the versatility of the M-IDE, enabling simultaneous proximity detection, range estimation, and material discrimination within the same sensing area. Such a feature is particularly relevant for applications in artificial skin for visually impaired users, where both proximity detection and strain sensation are required for safe and intelligent interaction with the environment.

3.2.5.3 Electronic Readout Circuitry

Following the sensor fabrication and characterization, the next stage of system development focused on the design of a flexible Printed Circuit Board (fPCB) to interface with the capacitive strain sensor. As shown in Figure 3.16(a), the system integrates multiple functional blocks for signal transduction, conditioning, digitization, processing, and wireless data transmission. At its core is the ESP32-S3-WROOM1 microcontroller, programmed using the Arduino IDE and connected to a USB–serial interface. The strain-induced capacitive changes from the M-IDE are digitized by a high-resolution, sigma-delta capacitance-to-digital converter (CDC), the AD7746. This CDC communicates with the microcontroller over the I^2C protocol. The system is powered either via USB or a 1000 mAh lithium-ion polymer battery, regulated to 3.3 V for all active components, including the ESP32-S3 and CDC. In both modes, the processed data is transmitted wirelessly via Wi-Fi to a Python-based server running on a host machine for real-time visualization and logging.

To optimize power consumption for portable operation, we evaluated two firmware modes: (i) continuous sensing without delay and (ii) periodic sensing with a 300 ms

delay between read–process–transmit cycles (Figure 3.16(c-d)). In the continuous mode, the microcontroller and CDC remain fully active, leading to sustained high current draw (132 mA average). This limits battery life to only 7.55 hours. In delay mode, the ESP32-S3 enters a low-power state between measurements. Conversely, the 300 ms delay mode introduces a cyclic sensing routine where each readout is followed by a defined sleep interval. This enables the ESP32-S3 to enter a low-power state between measurements, significantly reducing the average current draw to 78 mA and extending the operational lifetime to 12.77 hours (Figure 3.16(b)). Measured current profiles confirmed these behaviors. In no-delay mode, a dense continuous signal is observed. In delay mode, well-separated peaks appeared, corresponding to short active periods interspersed with low-power sleep intervals. This

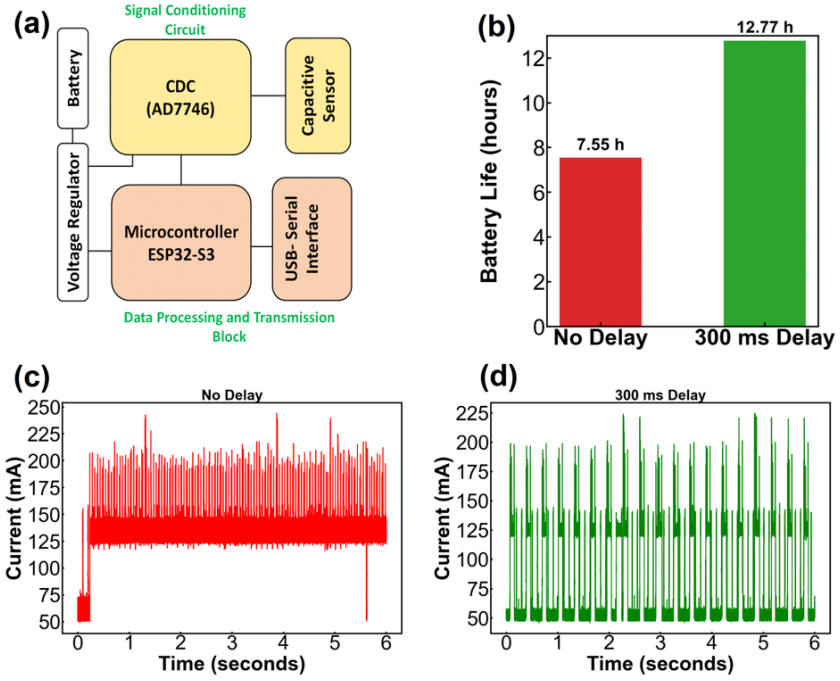


FIGURE 3.16: Electronic readout circuitry for M-IDE integration. (a) Block diagram showing sensor interfacing with AD7746 capacitance-to-digital converter, ESP32-S3 microcontroller, USB–serial interface, and Wi-Fi transmission. (b) Power profiles comparing continuous mode (132 mA, 7.55 h lifetime) and delay mode (78 mA, 12.77 h), demonstrating effective firmware-based power optimization for portable applications.

delay-based power cycling strategy is therefore highly effective in improving energy efficiency for wearable or long-duration sensing applications, without compromising system responsiveness or data integrity.

3.2.6 Application to Real-time Limb Movement Tracking

To demonstrate practical utility, the M-IDE device is attached to various body parts (wrist, hand, elbow, and knee), as shown in Figure 3.17. In these experiments, the devices acted as motion detectors, capturing precise movement patterns under different bending curvatures. A goniometer is employed to calibrate and verify the bending angles. The collected data confirmed that MDL-integrated M-IDEs accurately tracked bending–releasing cycles in real time, even on curvilinear body

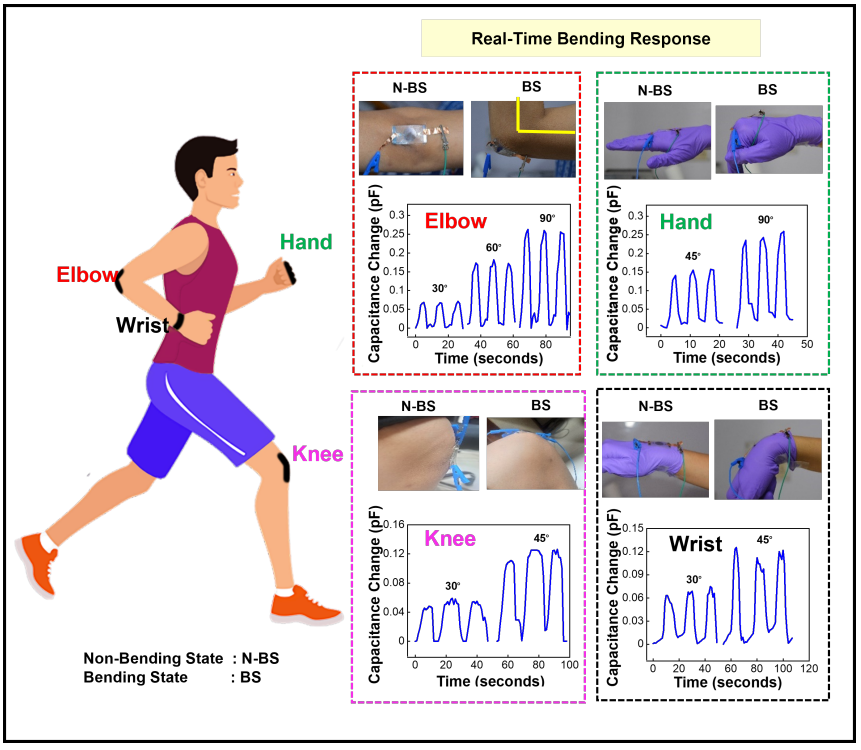


FIGURE 3.17: Real-time motion tracking with M-IDEs attached to the elbow, wrist, hand, and knee. A goniometer was used to calibrate bending angles (e.g., 45° and 90°). The device reliably distinguishes non-bending (N-BS) and bending states (BS).

surfaces. These results highlight the ability of M-IDE devices to capture complex motion patterns, offering valuable information for neurophysiological and kinesiological studies. Such capabilities are critical for applications in ergonomics, post-surgical rehabilitation, intelligent robotics, and artificial prosthetic systems.

3.2.7 Conclusion

In summary, a high-performance, skin-inspired bimodal device integrating strain and proximity sensing with a single readout mechanism has been developed and validated for limb motion detection. The engineered magnetodielectric layer (MDL) enhances strain sensitivity and extends the working range beyond 10 mm. This is achieved without additional fabrication steps such as molding, peel-off, or active layer transfer that are common in previous methods. The fabricated magnetically interdigitated electrodes (M-IDEs) demonstrate a four-fold increase in strain sensitivity and a 1.5-fold increase in contactless proximity sensitivity compared to planar interdigitated electrodes (P-IDEs). The working range of the M-IDE, varying from 6 mm to 20 mm, is tuned by the inter-particle separation within the magnetic nanoparticles embedded in the MDL. Additionally, the IDE-integrated design enables proximity sensing capable of distinguishing between conducting and non-conducting approaching objects. The M-IDE's sensitivity to conducting objects is approximately 23 times higher than to non-conducting ones, with a detection range reaching up to 21 mm. A compact readout circuit incorporating the AD7746 CDC and ESP32-S3 microcontroller with Wi-Fi transmission further enables real-time wireless monitoring with optimized power efficiency. Finally, real-time limb tracking experiments were performed by attaching M-IDEs to the wrist, hand, elbow, and knee, confirming their potential for applications in wearable electronics, prosthetics, and human–machine interfaces.

Chapter 4

Multimodal Sensors for Static and Dynamic Pressure Sensing

This chapter is divided into two sections on flexible pressure sensing. The first section focuses exclusively on dynamic pressure sensing, introducing a porous-based piezoelectric sensor. This device utilizes a poroelastic barium titanate matrix (PBM), where its engineered microstructure enhances deformation and sensitivity for capturing transient stimuli.

The second section significantly expands the sensing capability by introducing a hybrid multimodal sensor that concurrently detects both static and dynamic pressure. It synergistically combines a capacitive mechanism for static forces with a piezoelectric mechanism for dynamic forces, overcoming the inherent limitations of single-mode sensors.

4.1 Poroelastic $BaTiO_3$/PDMS for Dynamic Pressure Sensing

This chapter presents a poroelastic barium titanate matrix (PBM) for flexible pressure sensing applications. The use of a porous structure is motivated by its ability to undergo larger deformation compared to non-porous devices, thereby enhancing sensitivity. The fabrication process is designed to be simple, cost-effective, and sustainable. Prior to device fabrication, optimization of porosity and filler composition is carried out using COMSOL Multiphysics to ensure superior electromechanical response. A systematic assessment of the proposed PBM sensor is conducted by comparing its performance with that of non-porous composites, demonstrating the advantage of porosity engineering for flexible pressure sensors.

4.1.1 Introduction

Flexible and wearable sensors capable of capturing dynamic pressure signals are vital for applications in gait biomechanics, motion monitoring, and epidermal electronics [143]. Among the different sensing mechanisms, piezoelectric transduction is especially attractive because it is self-powered and well-suited for dynamic signal detection. [144]. However, the performance of conventional piezoelectric thin films is restricted by their high stiffness and limited deformability, which reduces stress transfer and lowers sensitivity [35]. While aligned piezoelectric nanowires enhance stress transduction, their brittleness under repeated deformation leads to crack formation [144]. To overcome these limitations, researchers explored porous architectures that reduce effective modulus [145]. This allows larger deformation under small forces and improves stress localization on piezoelectric domains [146].

The key challenge lies in the fabrication of porous piezoelectric composites. Traditional routes to induce porosity, such as acid–base reactions (e.g., HNO_3–$NaHCO_3$) [147], thermal decomposition of sacrificial particles (e.g., NH_4HCO_3) [148], and gas-foaming/emulsion methods. They rely on highly corrosive chemicals or generate toxic byproducts like NH_3 gas. These processes not only pose environmental and health hazards but also complicate the process, limiting their suitability for wearable and large-area device fabrication.

Recently, templating approaches have been proposed, where a sacrificial solid framework defines the porous structure. Among them, sugar templating stands out as an eco-friendly, cost-effective, and rapid method [149]. Sugar cubes naturally form interconnected porous networks, and once infiltrated with the piezoelectric composite precursor, they can be dissolved in plain water, leaving behind a mechanically robust, poroelastic framework. This method avoids toxic solvents, eliminates chemical waste, and even allows the retrieval of the sugar, reinforcing its sustainability. Moreover, the resulting porous barium titanate matrix (PBM) offers lower modulus, higher flexibility, and improved dynamic stress transduction compared to non-porous composites, thereby enhancing piezoelectric voltage generation.

This chapter demonstrates an eco-friendly and chemical-free fabrication process for introducing porosity into the piezoelectrically active BTO/PDMS functional layer. The porous functional layer is fabricated using sugar as scaffold material. First, the appropriate ratio of BTO/PDMS is allowed to infiltrate the sugar template via capillary action. Then, the sugar is leached using water and can be retrieved, resulting in an eco-friendly and chemical-free process. The fabricated flexible pressure sensor based on BTO/PDMS operates in a pressure range of 5-100 kPa, with a sensitivity of 110 mV/kPa. Additionally, finite element modeling (FEM) is performed to optimize the weight ratio and the porosity.

4.1.2 Device Concept and Design

The operating principle of the poroelastic barium titanate matrix (PBM) sensor is based on piezoelectric transduction, where mechanical stress applied to the active layer is converted into an electrical signal. The fundamental constitutive relation governing piezoelectricity is:

$$D = d \cdot \sigma + \varepsilon \cdot E \tag{4.1}$$

where D is the electric displacement, d is the piezoelectric coefficient, σ is the applied stress, ε is the dielectric permittivity, and E is the electric field. Under dynamic loading, an applied pressure generates stress within the BTO/PDMS composite. This stress induces polarization of the embedded barium titanate (BTO) nanoparticles, which manifests as an output voltage across the electrodes.

In conventional nonporous BTO/PDMS composites, the relatively high elastic modulus of the polymer matrix restricts deformation (Figure 4.1). This limits stress transfer to the embedded nanoparticles, thereby reducing effective polarization and lowering device sensitivity. Moreover, stress distribution within the dense matrix tends to be non-uniform, causing stress shielding effects around particle clusters. The introduction of porosity in the polymer matrix fundamentally alters this behavior. The effective modulus of the poroelastic structure decreases, enabling larger deformation under smaller external loads. This enhances strain localization at the nanoparticle sites, improving stress transduction and polarization. Additionally, the interconnected pore network allows localized stress redistribution, further amplifying the voltage response. Thus, the PBM sensor leverages two synergistic mechanisms: reduced stiffness of the porous matrix allows higher strain for a given load, while localized stress concentration at pore boundaries improves piezoelectric activity (Figure 4.1). Together, these effects yield a higher piezoelectric output compared

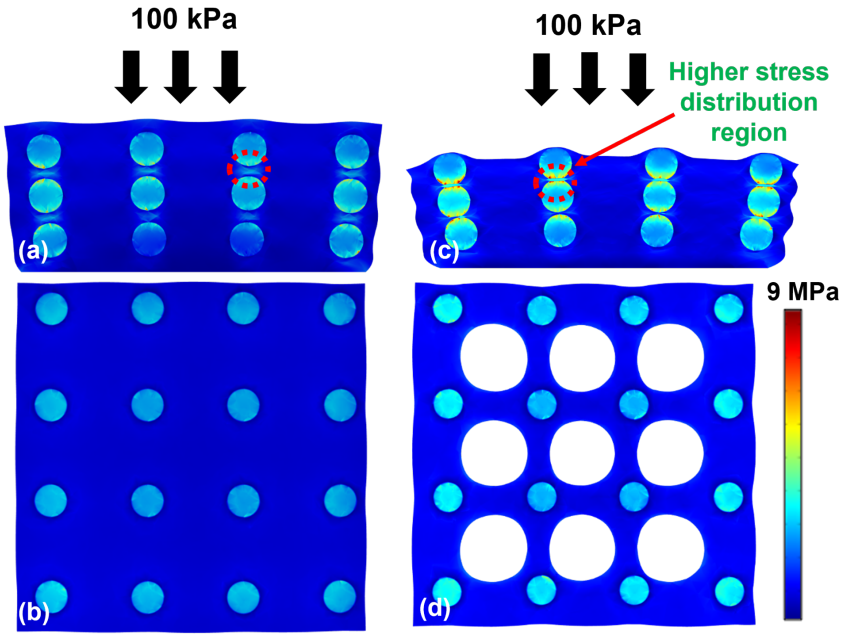


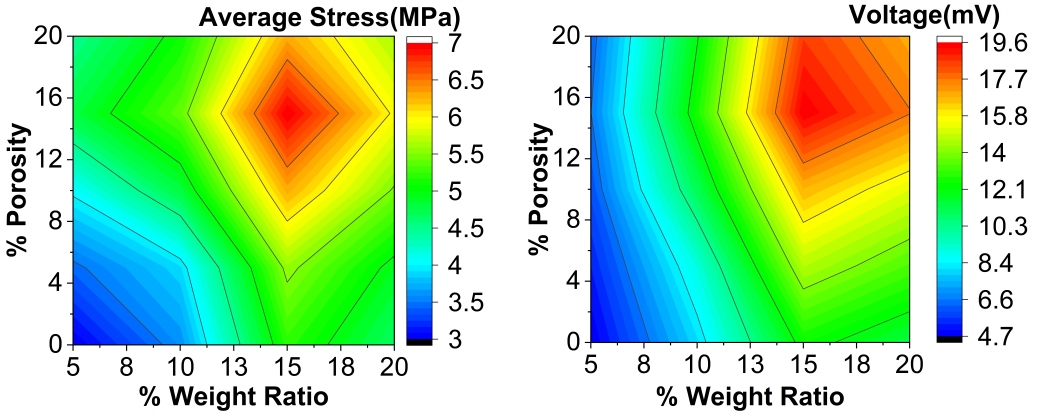
FIGURE 4.1: The stress analysis of a simulated model of a flexible piezoelectric pressure sensor. (a) Cross-sectional view of a model with no porosity. (b) Top view of a model with no porosity. (c) Cross-sectional view of a model with porosity. (d) Top view of a model with porosity. The stress analysis shows that for the same applied pressure (100 kPa), the porous model deforms more, giving a higher stress generation as well as a higher probability of nanoparticle cross-linking compared to the non-porous model.

to nonporous composites, making porosity engineering a simple, scalable, and sustainable strategy for enhancing the performance of flexible dynamic pressure sensors.

4.1.3 Finite Element Modelling

Non-porous (bulk) BTO/PDMS and PBM devices are simulated in COMSOL^{TM} Multiphysics 5.5a using the piezoelectric module. A model consists of a 1μm x 1μm x 0.5μm PDMS substrate embedded with BTO nanoparticles of 50 nm radius (Figure 4.1). Different porosity levels are introduced in the substrate to study their influence. The bottom electrode is electrically grounded and structurally fixed. The boundary load from no load to 100 kPa is applied on the top surface.

The %weight ratio of BTO nanoparticles (NPs) and substrate porosity is varied in the range of 0-20%. The generated internal stress and piezoelectric voltage are analyzed. For each configuration, the internal stress distribution and piezoelectric voltage are analyzed. Initially, the non-porous BTO/PDMS nanocomposite is simulated by changing the %weight ratio of BTO in the PDMS. The simulated output response of the non-porous nanocomposites is then compared with PBM, where porosity is introduced to improve performance [147]. The introduction of porosity enhances the stress/strain distribution on NPs within the composite, thereby improving the effective piezoelectric activity. The porosity is varied from 0 to 20% at different %weight ratios of BTO/PDMS. The 2D simulated models with and without porosity at a 10% weight ratio are shown in Figure 4.1(a) and Figure 4.1(b), respectively. Figure 4.2(a) and Figure 4.2(b) present the simulated average stress and the generated voltage for different %weight ratios and porosities. The results clearly indicate that with an increase in BTO loading and porosity, the simulated response improves [150]. However, the response degrades when the BTO weight ratio and porosity exceed ∼16%. The decay in output response can be attributed



(a) (b)

FIGURE 4.2: 2-D plots for optimizing the weight % of BTO in PDMS and % porosity in the substrate. (a) Voltage generated at different % porosity and weight ratios of BTO nanoparticles in PDMS. (b) Average stress generated at different weight ratios of BTO in PDMS and % porosity. The plots indicate that the maximum voltage is generated at a 15% weight ratio and 16% substrate porosity.

to the formation of NP agglomerates for higher %weight ratios [151]. Such agglomerates reduce the effective strain distribution and cancel out the polarization fields of individual NPs, thereby decreasing the response. Furthermore, the introduction of porosity changes the structural properties of the nanocomposite. The effective stiffness of the nanocomposite decreases with increasing porosity. This allows for a larger displacement range and higher internal stress generation on individual NPs in the direction of applied pressure. At the same time, the output voltage also depends on the effective number of active NPs per unit volume [151]. The introduction of porosity in the nanocomposite decreases the effective number of NPs per unit volume. Also, the capillary action responsible for filling up the composite template causes an increase in the effective %weight ratio in composite interconnects. The combined effect of reduced nanoparticle density per unit volume and agglomeration at higher weight ratios results in deterioration of the electromechanical response at higher %porosity levels. From this combined porosity–filler study, the optimum configuration is identified as 15 wt% BTO loading with ∼16%. porosity in the PBM.

4.1.4 Fabrication Process Flow

Figure 4.3 shows the simple and cost-effective fabrication process of a PBM-based flexible pressure sensor. Firstly, the PDMS base and curing agent (Slygard 184) are mixed/stirred in the ratio 10:1 for about 20 minutes. The solution is desiccated for about half an hour. Afterwards, 15% (by weight ratio) BTO nanoparticles (NPs) (50 nm) are added to the PDMS solution and mixed until a white suspension is obtained. The solution is again desiccated for about half an hour to remove the bubbles. Sugar cubes are then used as sacrificial templates to introduce porosity. The pre-mixed BTO/PDMS solution infiltrates the sugar template via capillary action. The process typically requires ∼4 hours for complete absorption. The nanocomposite-soaked

sugar cubes are subsequently cured at 70°C for 4 hours, solidifying the poroelastic framework. After curing, the sugar is dissolved in hot water, leaving behind an

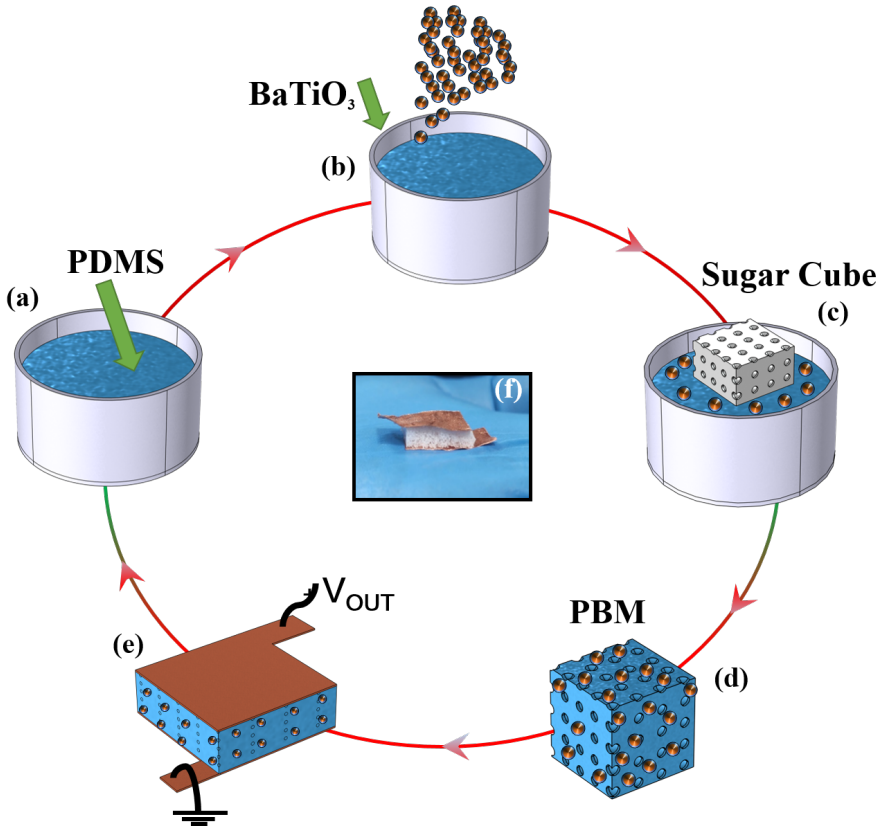


FIGURE 4.3: Fabrication process of the PBM sensor. (a) PDMS base and curing agent are thoroughly mixed in a ratio of 10:1 for about 20 min. (b) 15% by weight of BTO is added to the PDMS solution. (c) Sugar template is placed in the BTO/PDMS nanocomposite, and the nanocomposite is allowed to soak in it. (d) Poroelastic matrix of the nanocomposite-soaked sugar cube. (e) A thin nanocomposite layer is sliced and sandwiched between the copper electrodes. (f) Device prototype of a fabricated PBM sensor.

interconnected porous BTO/PDMS skeleton. Any residual water trapped within the pores is evaporated via convection heating, resulting in the final poroelastic barium titanate matrix (PBM). The porous PBM blocks are sliced into thin layers using a surgical blade. To form the device, copper tape electrodes (EMS Hatfield, UK) are attached to the top and bottom surfaces, and the assembly is encapsulated with Kapton tape to ensure stable electrical connections. For comparison, nonporous

BTO/PDMS bulk films are also fabricated using the same procedure but without the sugar templating step. Figure 4.4 shows SEM images highlighting the difference between the dense nonporous composite and the interconnected porous network of the PBM sensor.

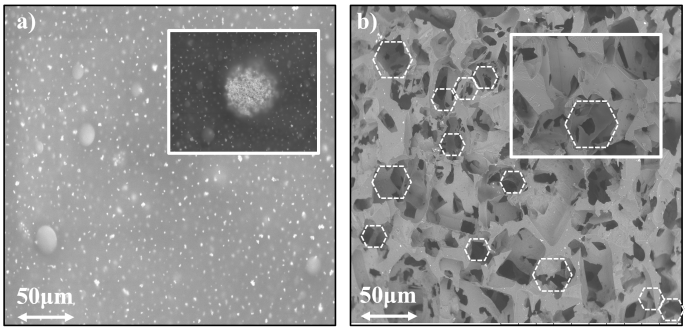
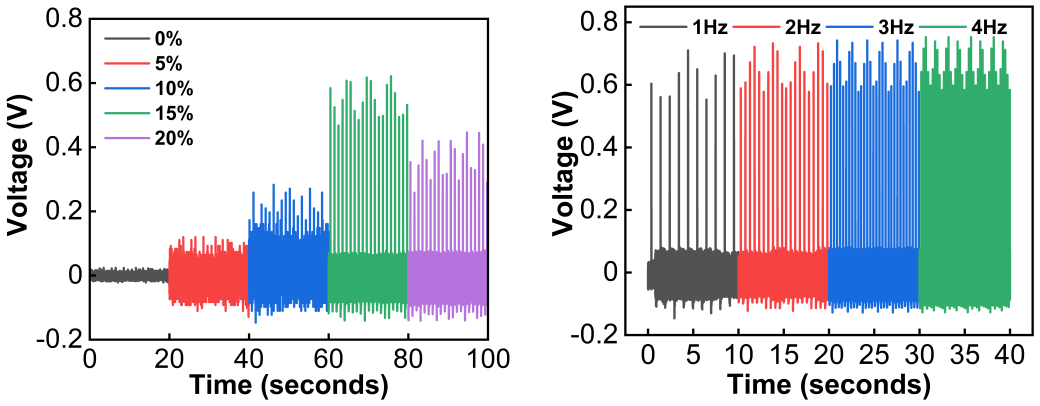


FIGURE 4.4: SEM image. (a) Nonporous composite in which BTO NPs are homogeneously blended with PDMS. (b) PBM flexible sensor showing the porous network.

4.1.5 Electromechanical Characterization

The PBM sensors with different % weight ratios of BTO/PDMS are fabricated and tested. Figure 4.5(a) shows the generated piezoelectric voltage as a function of the % weight ratio of BTO in PDMS. The generated voltage increases with an increase in the % weight ratio of BTO in PDMS. After a 15% weight ratio, the induced voltage decreases. The decay in output is due to nanoparticle agglomeration at higher % weight ratios [150]. The experimentally obtained voltage response trend agrees with the simulated results for different % weight ratios of BTO/PDMS. Furthermore, the devices are tested under pressure loading at 1 Hz. As shown in Figure 4.4(b), no noticeable change in output voltage is observed across frequencies from 0 to 5 Hz [146]. The compressive stress–strain testing of the nonporous BTO/PDMS composite and PBM sensor is measured using a universal testing machine (Instron 3365). Figure 4.6(a) and (b) show the measured compressive stress–strain curves for the

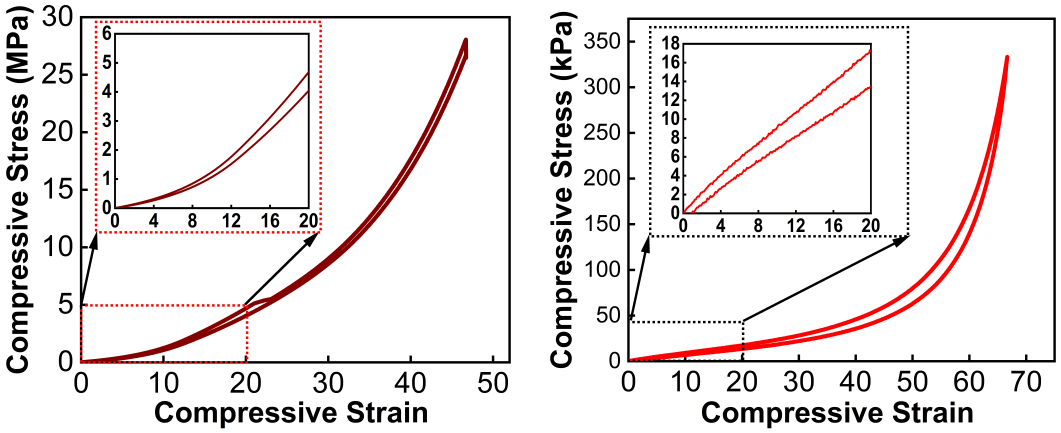


(a) (b)

FIGURE 4.5: (a) Sensor response at different % weight ratios of BTO in PDMS. (b) Frequency response of the PBM sensor. The generated voltage remains constant over a frequency range (0–5 Hz).

nonporous BTO/PDMS and PBM sensors. The compressive moduli (E_c) of the two samples are calculated by fitting a straight line to the linear stress–strain curves [152].

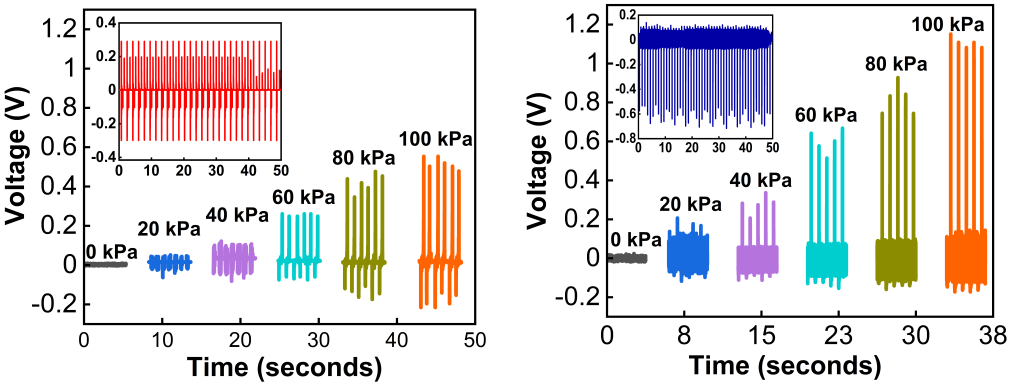
The obtained compressive moduli (E_c) of PBM and nonporous BTO/PDMS are 83 kPa (0.083 MPa) and 12 MPa, respectively. Thus, the introduction of porosity results in a lower compressive modulus for the PBM sensor, indicating that smaller



(a) (b)

FIGURE 4.6: (a) Compressive stress–strain curve of the non-porous BTO/PDMS sample. The calculated elastic modulus (E_c) of the sample is 12 MPa. (b) Compressive stress–strain curve of the PBM sensor. The calculated E_c of the sample is 83 kPa. The introduction of porosity results in a lower compressive modulus of the PBM sensor, indicating that smaller forces generate larger deformation and, hence, account for higher sensitivity.

forces generate larger deformation and hence contribute to higher sensitivity. The dielectric constants of the nonporous BTO/PDMS and PBM are 4.27 and 3.89, respectively. The performance of the as-fabricated PBM pressure sensor is measured by applying a load varying from 0 to 100 kPa, and the electrical output of the device is recorded using a DSO (SIGLENT SDS 1072 DSO). Figure 4.7(a) and (b) show the voltage response of the nonporous and the PBM flexible pressure sensors, respectively. The results show that the peak voltage generated in the PBM sensor is 1.1 V, in contrast to 500 mV in the nonporous sensor at 100 kPa. The piezoelectric voltage for the PBM sensor thus shows a nearly two-fold enhancement. The superior performance can be attributed to the combined effect of increased mechanical flexibility (i.e., small forces cause large stress) and the interconnected PBM structure, which helps localize stresses on the BTO NPs. Polarity switching tests are performed to confirm the piezoelectric origin of the PBM sensor's signal [153]. The "switching polarity" tests are conducted to exclude the interference from ambient environmental noise and stray triboelectric effects on the PBM sensor [153]. The resulting responses are shown in the inset of Figure 4.7(b). Figure 4.8(a) compares



(a) (b)

FIGURE 4.7: Voltage response at different pressures. (a) Voltage generated in nonporous BTO/PDMS composite at a weight ratio of 15%. (b) Voltage generated in the PBM sensor at 15%. weight ratio of BTO in PDMS. The results show that the PBM generates a voltage two times greater than nonporous sensor. The inset shows the switching polarity test of the PBM sensor.

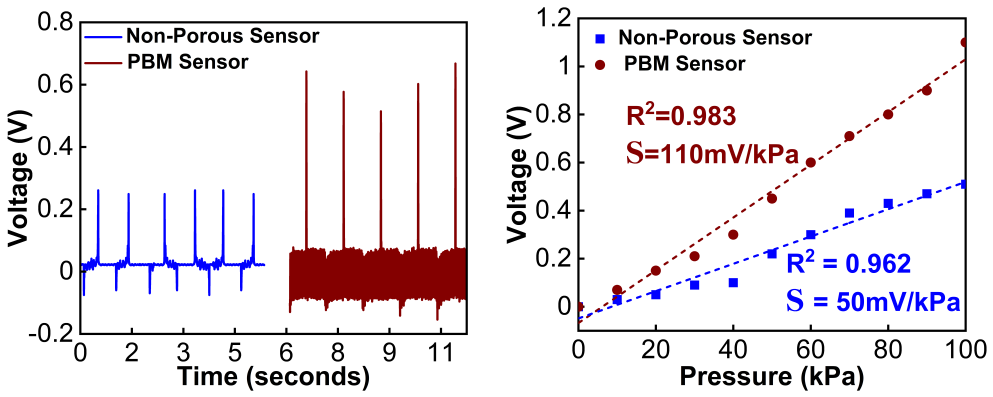


FIGURE 4.8: (a) Comparison of responses for nonporous and PBM sensors at 50 kPa. (b) Sensitivity (S) curve of the sensors for different pressures.

both devices under an applied pressure of 50 kPa, showing repeatable performance with a deviation of only 0.47%. Both devices exhibit linear behavior across the 5–100kPa range, but the PBM sensor demonstrates higher linearity and sensitivity. The PBM sensor shows a sensitivity (S) of approximately 110 mV/kPa, in contrast to 50 mV/kPa for the nonporous device (Figure 4.8(b)). Therefore, the PBM device is more sensitive to desired biomechanical pressure ranges (10–50 kPa) than the nonporous sensor [154]. The working range of the PBM sensor is also investigated. The minimum detection limit is determined by applying impulse pressure loads, with the minimum detectable pressure found to be 5 kPa. Similarly, the maximum pressure detection limit is identified by increasing the pressure load until the output voltage of the PBM sensor saturates. The maximum detectable pressure is 100 kPa. Thus, the working range of the PBM sensor is 5–100 kPa.

4.1.6 Conclusion

A highly sensitive PBM sensor is developed using a simple and cost-effective sugar-templated process. Compared to the nonporous BTO/PDMS composite, the PBM sensor shows a two-fold increase in sensitivity, generating a peak output of 1.1 V

at 100 kPa. The device exhibits excellent linearity ($R^2 = 0.983$), a repeatability deviation of 0.47%, and an effective working range of 5–100 kPa. Finite element simulations confirm that optimal performance is achieved at a 15% BTO loading and ∼16% porosity, balancing stress localization with sufficient nanoparticle density. These results highlight the PBM sensor's potential for applications in wearable pressure monitoring, gait biomechanics, and motion-tracking systems.

4.2 Multimodal Integrated Device for Static and Dynamic Sensing

This section introduces a multimodal mechanoreceptor that integrates capacitive and piezoelectric transduction mechanisms to emulate the human somatosensory response. In contrast to conventional devices that rely on a single sensing mode, the proposed design combines a μ-pyramidal capacitive sensor for static stimuli with a piezoelectric device for dynamic stimuli. This synergistic configuration extends the detection range from 1 to 140 kPa while maintaining high sensitivity across regimes, overcoming the limitations of standalone capacitive or piezoelectric sensors. The functionality of the multimodal device is validated through real-time demonstrations of human grabbing and holding, confirming its ability to simultaneously capture static and dynamic responses.

4.2.1 Introduction

Human skin perceives and differentiates different spatiotemporal tactile stimuli (static and dynamic pressure, vibrations) through different mechanoreceptors [129]. Slowly adapting mechanoreceptors (i.e., Merkel and Ruffini corpuscles) perceive

static or sustained pressure on the skin [155], while fast-adapting mechanoreceptors (i.e., Meissner and Pacinian corpuscles) detect dynamic pressure and vibrations. For electronic skin (E-skin) to truly emulate this somatosensory response, the ability to perceive and discriminate between both static and dynamic stimuli over a wide sensing range is paramount [129]. For instance, these capabilities are essential for robots to perform complex tasks like grasping, holding, and manipulating objects with dexterity and feedback [156].

Previous efforts in E-skin development have often relied on single-mode sensing mechanisms. Piezoresistive or capacitive sensors are typically used for static stimulus perception, whereas piezoelectric sensors are employed for dynamic stimulus detection, though often with a limited sensitivity range [157]. This division is inherent to their operating principles: capacitive (C-mode) and piezoresistive sensors rely on a continuous change in an electrical property (capacitance, resistance) under sustained load, whereas piezoelectric (P-mode) sensors generate a response only to dynamic stimuli. Although novel material designs, including micro-pillars, micro-pyramids, and graded structures, have improved the sensitivity and range of individual modes [158], a fundamental challenge persists. No single-mechanism sensor can simultaneously detect both static and dynamic pressure with high sensitivity across a broad range. A few reported multimodal sensors demonstrate texture recognition but are ultimately limited by a poor sensing range (typically ∼1–60 kPa) [159].

This section extends the functionality of E-skin by integrating capacitive and piezoelectric sensing into a single device for the simultaneous detection of both static and dynamic signals across a wide pressure spectrum. In this design, the C-mode detects subtle and sustained static pressure with high sensitivity, enabled by an epidermal micro-pyramidal polydimethylsiloxane (PDMS) dielectric layer. Simultaneously, the P-mode detects dynamic touch and vibration across a large pressure range. The synergetic combination of these two modes significantly extends the overall sensitive

range of the device (1–140 kPa) and enables true multifunctionality, mirroring the perceptual capabilities of human skin. As a proof of concept, we demonstrate the application of this multimodal device for real-time object manipulation, successfully discerning the distinct static and dynamic signals associated with grabbing, holding, and slipping of an object.

4.2.2 Device Concept and Design

A wide detection range multimodal (P/C-mode) sensory platform by integrating epidermal μ-structured capacitive (for C-mode) and piezoelectric device (P-mode) is reported. Inspired by human skin, the device (Figure 4.9) integrates the piezoelectric sensor and the capacitive device. Here, C-mode perceives static stimuli, whereas P-mode detects the dynamic response simultaneously. In the demonstrated device, the top piezoelectric layer consists of a polyvinylidene fluoride (PVDF) film incorporated with 3 wt% MoS_2 nanosheets. The incorporation of MoS_2 enhances the piezoelectric coefficient (d_{33}) by improving dipole alignment and promoting nucleation of the electroactive β-phase in PVDF through strong interfacial interaction

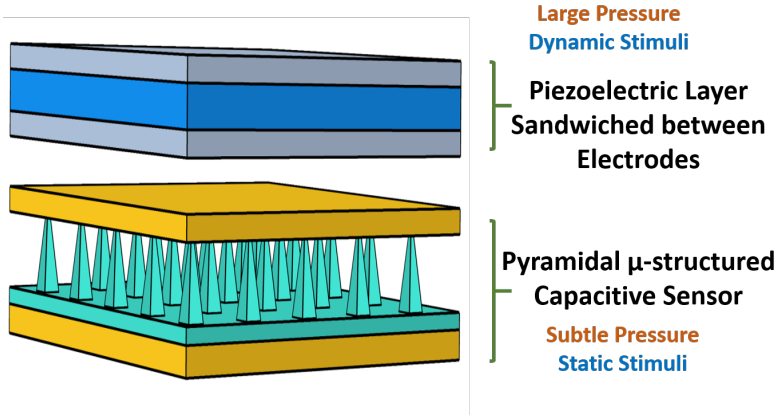


FIGURE 4.9: Conceptual Image of the multi-mode device. The device integrates the capacitive-piezoelectric sensors for the static and dynamic mechano-response. This synergetic effect allows detection of pressure stimuli over a broad sensing range (1-140 kPa).

between the layered MoS_2 surface and the polymer chains. This enables higher voltage generation under dynamic pressure stimuli. This layer is primarily responsible for sensing fast-changing, high-amplitude signals. The bottom μ-pyramidal PDMS dielectric layer functions as the capacitive element for static and subtle stimuli. The μ-pyramidal structure offers improved compressibility and stress–displacement transduction compared to a planar dielectric, thereby enhancing sensitivity [160]. Together, the two transduction mechanisms are vertically integrated into a multimodal device that captures both static and dynamic stimuli, effectively mimicking the dual mechanoreceptor behavior in human skin.

4.2.2.1 Working Mechanism

Mimicking the somatosensory response of the human skin, the multimodal sensor is fabricated by integrating a capacitive-piezoelectric layer for a wide sensing range. The dynamic pressure stimuli on the piezoelectric layer generate the output voltage. The generated voltage is quantified by the equation given as [161]:

$$V_{oc} = g_{33} \times \sigma \times Y \times g = \frac{d_{33}}{\varepsilon_0 \varepsilon_r} \times \sigma \times Y \times g \tag{1}$$

where g_{33} is the voltage constant, σ is the induced stress, g is the thickness of the material, and Y is Young's modulus. Therefore, the output voltage is proportional to the induced stress, which in turn depends on the applied pressure. The response of the capacitive sensor can be realized by the parallel plate configuration, the capacitance is given as

$$C = \frac{\varepsilon_0 \varepsilon_r A}{d} \tag{2}$$

where $\varepsilon_0 \varepsilon_r$ is the permittivity of the dielectric material, A is the overlapping electrode area, and d is the thickness of the dielectric layer. With increasing static

pressure, the relative permittivity ε_r increases while the distance d between the plates decreases [162]. This dual effect leads to a greater change in capacitance. The capacitive sensor with a planar dielectric layer is less sensitive compared to the μ-pyramidal-structured dielectric.

4.2.3 Fabrication Process Flow

The multimodal device is fabricated by vertical stacking of capacitive and piezoelectric sensors. The fabrication process is divided into three steps: fabrication of the capacitive sensor, fabrication of the piezoelectric sensor, and assembly of these sensors (Figure 4.10). First, the μ-pyramidal PDMS dielectric layer is fabricated using silicon molds. The silicon substrate is lithographically patterned with a **square** window opening of 30 μm x **30 μm** at a pitch of 50 μm, followed by wet etching with

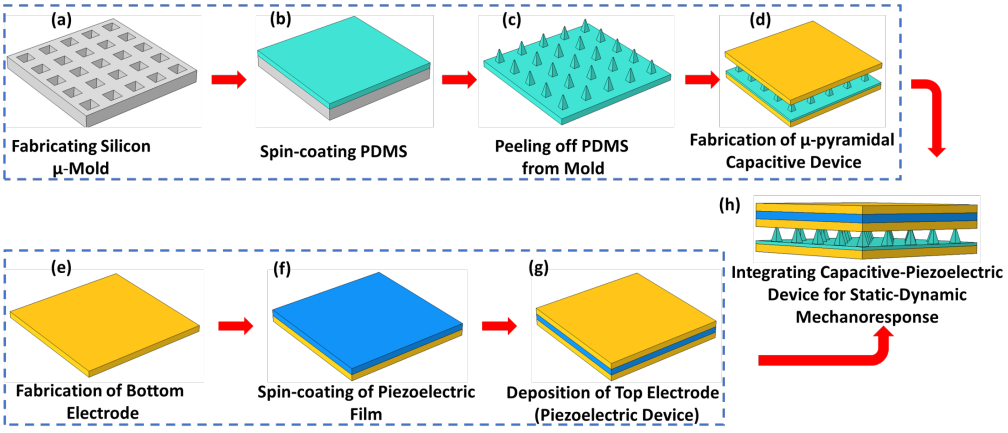


FIGURE 4.10: Schematic of the fabrication process of the multimode device. The process is divided into three main steps: fabrication of the capacitive sensor, fabrication of the piezoelectric sensor, and integration of both components. (a) Fabrication of the silicon mold via standard photolithography followed by wet etching of silicon using KOH. (b) Spin coating of PDMS onto the silicon mold. (c) Peeling off the cured PDMS to obtain the μ-pyramidal structure. (d) Sandwiching the μ-pyramidal PDMS between two electrodes to form the capacitive sensor. (e) Deposition of a gold electrode on a PET sheet using e-beam evaporation to serve as the bottom electrode. (f) Spin coating of the piezoelectric layer onto the bottom electrode. (g) Fabrication of the top electrode. (h) Final integration of the capacitive and piezoelectric layers to form the multimode device.

potassium hydroxide (KOH) at 80 °C. Then, PDMS is spin-coated onto the mold. After curing for 1 hour at 120°C, the PDMS dielectric layer is peeled off from the mold. The top and bottom electrodes are formed by depositing gold onto a polyethylene terephthalate (PET) sheet. Prior to gold deposition, a thin chromium adhesion layer is deposited to improve film adhesion. Both electrodes are spin-coated with a very thin layer of PDMS, and after pre-curing for 10 minutes, the μ-pyramidal layer is sandwiched between them. The thin layer of pre-cured PDMS serves as an adhesion promoter between the electrodes and the sandwiched μ-pyramidal dielectric layer. Secondly, the piezoelectric sensor is fabricated by spin-coating a piezoelectric film onto a bottom electrode (deposited on a PET sheet). The top electrode is formed by gold deposition using an e-beam evaporator. Finally, the individual capacitive and piezoelectric devices are vertically assembled and encapsulated in PDMS after electrical contacts are established. Figures 4.11(a) and 4.11(b) show the top-view SEM images of the μ-pyramidal PDMS layer.

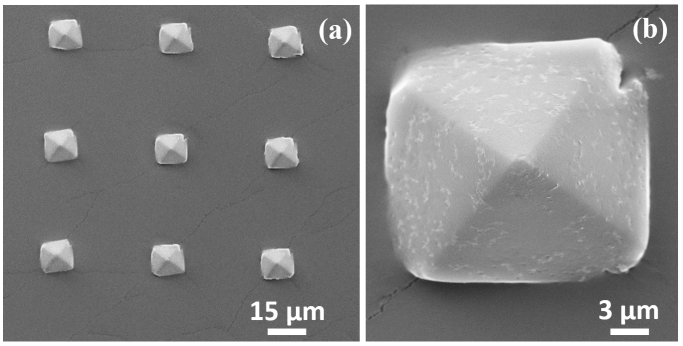
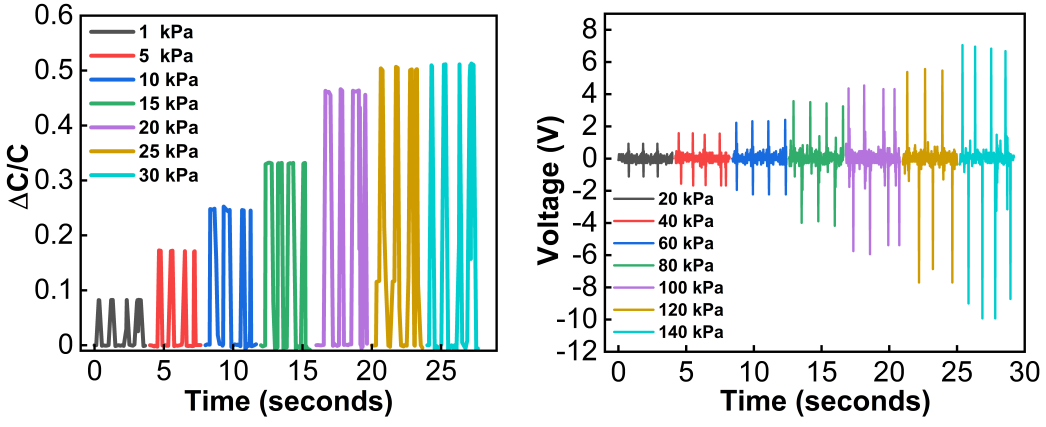


FIGURE 4.11: (a) SEM image of the μ-pyramidal PDMS layer. (b) Magnified view showing a single μ-pyramid.

4.2.4 Results and Discussion

The electromechanical characterization of the multimodal device is performed using a standard push tester. The corresponding electrical responses are measured by

two instruments: the capacitive response (C-mode) is recorded using a Keithley Parameter Analyzer (4200 SCS), and the piezoelectric response (P-mode) is captured with a digital oscilloscope (PicoScope 3000 series). Figure 4.12(a) shows the response of the μ-pyramidal-based capacitive device. The results confirm that the sensor is responsive to static pressure stimuli in the range of 1–25 kPa. The C-mode detects a minimum pressure of 1 kPa and saturates beyond 25 kPa. In contrast, under P-mode operation, the device responds to dynamic pressure stimuli over a broader range of 20–140 kPa, as shown in Figure 4.12(b). The incorporation of MoS_2 into the PVDF matrix enhances the piezoelectric coefficient d_{33}, resulting in a higher voltage output of up to 16 V at 140 kPa. Figure 4.13 illustrates the overall working range characteristics of the device. Notably, the synergistic effect of the multimodal mechano-receptor extends the sensing range from 1 kPa to 140 kPa. The C-mode exhibits a sensitivity of 30 fF/kPa^{-1} up to 25 kPa, which is attributed to the enhanced compressibility and deformation of the μ-pyramidal PDMS structure. The P-mode extends the working range up to 140 kPa with a voltage sensitivity of 160 mV/kPa. Thus, the combined operation of the C-mode and P-mode enables both



(a) (b)

FIGURE 4.12: Capacitive response of the multi-mode mechanoreceptor. The device can detect the minimum pressure of 1 kPa (b) Dynamic electromechanical characterization of piezoelectric device. The device has a working range of 20-140 kPa with peak-to-peak voltage generation of 16V.

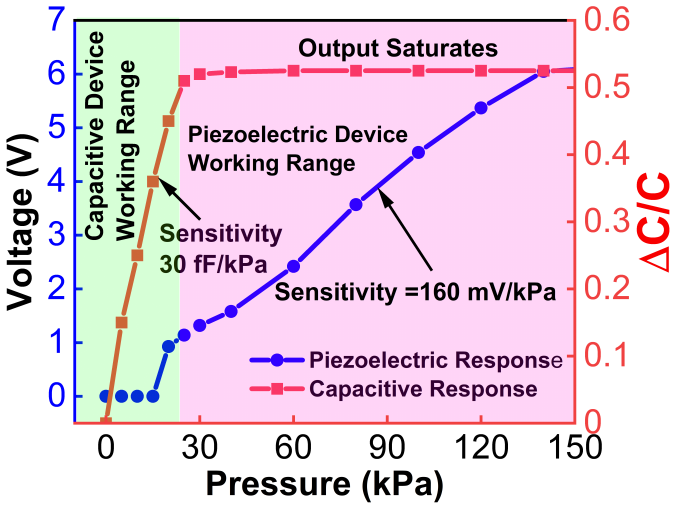


FIGURE 4.13: Sensing range of the multi-mode mechanoreceptor. The capacitive device detects minimum pressure of 1 kPa while piezoelectric device has working range of 20-140 kPa.

static and dynamic pressure sensing, significantly enhancing the device's functional range and application versatility.

As the device can successfully discriminate the static and dynamic stimuli, a real-time response of the device's mutual touch and pressure sensation is presented in Figure 4.14. In a relaxed state (when fingers are not in touch with the bottle), both devices show zero response. As the first touch is made, the instantaneous voltage (4 V) generation occurs dynamically and is recorded by a piezoelectric device, whereas the capacitive device shows a shift in response from the base value. When a glass is grabbed firmly, the piezoelectric device initially shows a small peak (2 V) and zero afterward. The capacitive response value increases as the glass is grabbed tightly (more pressure results in more capacitive change). Similarly, during release, multiple voltage peaks are generated within the piezo-device, confirming the slipping of the bottle. The capacitive response just returns to the initial value without inferring slipping details. Therefore, real-time detailed information can be obtained for decoding complex human motions covering subtle-to-large stimuli (0-150 kPa).

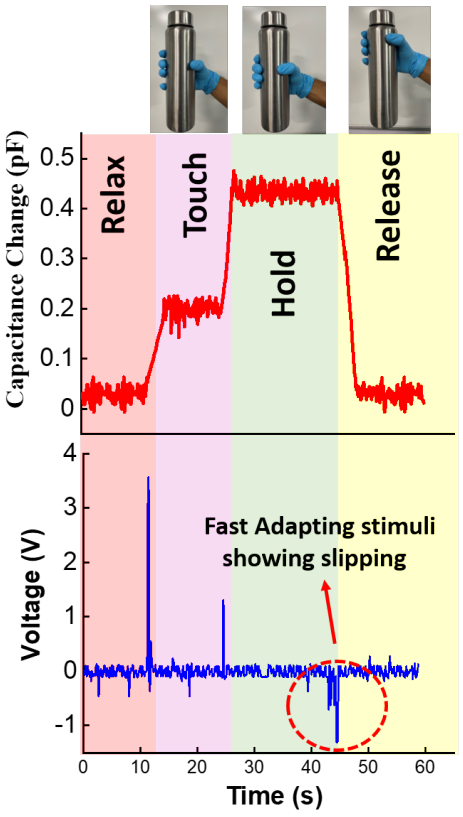


FIGURE 4.14: The voltage response of Fast adapting (piezoelectric device) and Slow adapting (capacitive device) mechano-receptor from holding to releasing of the object.

4.2.5 Conclusion

In conclusion, we introduce a multimodal integrated sensory platform capable of simultaneously detecting static and dynamic stimuli across a wide pressure sensing range. Static and subtle stimuli are detected by the μ-pyramidal capacitive device (C-mode), while dynamically changing stimuli are sensed by the piezoelectric device (P-mode). The synergistic effect of the multimodal architecture enables pressure detection over a broad range from 1–140 kPa. The C-mode effectively detects subtle pressure stimuli in the range of 1–25 kPa with a sensitivity of 30 fF/kPa. The P-mode extends the detection range from 20–140 kPa with a sensitivity of 150 mV/kPa. This approach streamlines sensory integration for next-generation electronic skin (E-skin)

systems. As a proof of concept, a real-time human grabbing and holding activity is demonstrated, validating the functionality of the device for both static and dynamic tactile perception.

Chapter 5

Sub-mm High-Resolution Flexible Capacitive Sensor Array for Surface Texture Mapping

This chapter introduces a high-density flexible capacitive tactile array designed to achieve sub-millimeter spatial resolution, a key requirement for human-like tactile sensing. Contrary to conventional tactile systems with limited pixel density, the proposed platform integrates 4096 individually addressable sensing units in a 64×64 configuration on a polymer substrate. A magnetodielectric layer (MDL) is incorporated between the electrodes to enhance device performance. The concept is validated through simulation and experimental characterization. A customized readout circuit, designed and implemented as a flexible hybrid electronic (FHE) system, enables independent pixel addressing for the 64×64 array. The fully integrated system demonstrated its 100-μm spatial resolution by successfully reconstructing the surface profile of a circular ring.

5.1 Introduction

Tactile sensing is a critical attribute of human skin, enabling the perception of a wide range of physical stimuli from the surrounding environment [163]. Developing advanced, human-like tactile sensing capabilities remains a critical challenge for next-generation robots, prosthetics, and human-machine interfaces [163]. A key feature for such tactile sensing is the integration of high-density sensors to achieve high spatial resolution. To achieve this, three key requirements must be addressed. First, high spatial resolution is essential for precision across diverse applications, ideally reaching 0.2 mm or better [164]. Second, tactile sensing arrays must exhibit strong immunity to external noise, which requires robust circuit architecture and careful signal acquisition design [165]. Third, scalability and seamless integration are critical, allowing tactile arrays to conform to three-dimensional surfaces with mechanical flexibility and efficient electrical connectivity [166]. Simple, scalable fabrication processes are vital for practical implementation in robotics, prosthetics, and wearable technologies.

Recent advancements to meet these requirements have introduced a wide range of innovations in designs and materials. In resistive sensing, Chen et al. developed a 12×12 array incorporating a macrodome structure to enhance sensitivity, while Park et al. utilized CNT-coated porous PDMS with stacked electrode layers for improved signal detection [167, 168]. Nela et al. presented a 16×16 CNT-based active matrix with 4 mm spatial resolution [169]. Optical and triboelectric sensors have also been explored as alternate tactile sensing strategies. For instance, Lumelsky et al. developed an 8×8 infrared-sensitive skin, and Lin et al. demonstrated a 5×5 piezoelectric array using PTFE textiles with integrated row-column electrodes [170, 171]. Although these systems are effective in detecting force distributions, they face inherent limitations in spatial resolution and sensitivity.

Capacitive tactile sensors have emerged as a promising solution due to their mechanical compliance, low power consumption, and scalable architecture. Pyo et al. reported a 10×10 capacitive array with a pixel pitch of 4.2 mm using SU-8 spacers to maintain structural separation [95]. Another flexible platform integrated 12×12 sensors of 600 μm size directly onto a bendable interconnect substrate, achieving repeatability and robustness across multiple wafers [60]. A more advanced MEMS-fabricated design incorporated 340 μm × 340 μm electrodes in a flexible polyimide substrate and achieved a spatial resolution of 420 μm using a compressible PDMS dielectric [165]. Despite these advancements, most reported capacitive tactile arrays remain limited to fewer than 256 sensors and pixel sizes exceeding 400 μm, restricting their applicability for high-resolution tactile mapping. Achieving pixel sizes below this threshold is essential to emulate the spatial resolution of human fingertip sensitivity, but it introduces significant design challenges. Reducing the pixel size to 100 × 100 μm significantly lowers the electrode area, resulting in extremely small baseline capacitance values in the femtofarad range, especially with conventional low-permittivity dielectrics such as PDMS ($\epsilon = 2.5$). Under such conditions, the capacitance change under applied pressure becomes negligible, leading to poor signal resolution. To address this issue, ionic dielectric materials have been explored, but their moisture sensitivity and poor compatibility with MEMS fabrication processes limit their scalability. To overcome this trade-off, we introduce a magnetodielectric composite layer by dispersing magnetic nanoparticles into PDMS. This material, first presented in Chapter 3 for enhancing strain and proximity sensing, improves dielectric properties while maintaining mechanical flexibility and MEMS compatibility. Its integration into the high-density array enables stronger capacitive responses even at pixel dimensions of 100 μm.

This chapter presents a high-resolution flexible capacitive tactile sensor array comprising 64 × 64 individually addressable pixels, for a total of 4096 sensors over a

2.5 cm^2 active area. Each sensor unit measures 100 μm $\times$ 100 μm, achieving a spatial resolution comparable to that of human skin. To address individual cells and mitigate parasitic effects and external noise, common challenges in fF-range measurements of small electrodes, a custom electronic read-out circuit is developed. Additionally, a thin compressible polydimethylsiloxane (PDMS) layer is incorporated to tune the pressure sensitivity and expand the dynamic range. The tactile sensing array effectively demonstrates its capability by mapping force distributions with high precision.

5.2 Device Concept and Design

5.2.1 Sensing Method

The proposed device is designed to detect the tangential component of force using a parallel-plate capacitive mechanism. Each sensing pixel operates as a parallel-plate capacitor with dimensions of 100 μm $\times$ 100 μm and a center-to-center pitch of 150 μm, closely emulating the ridge spacing of a typical human fingerprint. This biomimetic layout facilitates high spatial resolution and sensitivity in detecting local force vectors.

As illustrated in Figure 5.1(a), the sensor comprises two electrodes with a magnetodielectric layer (MDL) (consisting of Fe_3O_4 nanoparticles in PDMS) sandwiched in between. The fundamental sensing mechanism is depicted in Figure 5.1(b). When external pressure is applied, the dielectric layer is compressed, leading to an increase in capacitance through two distinct mechanisms:

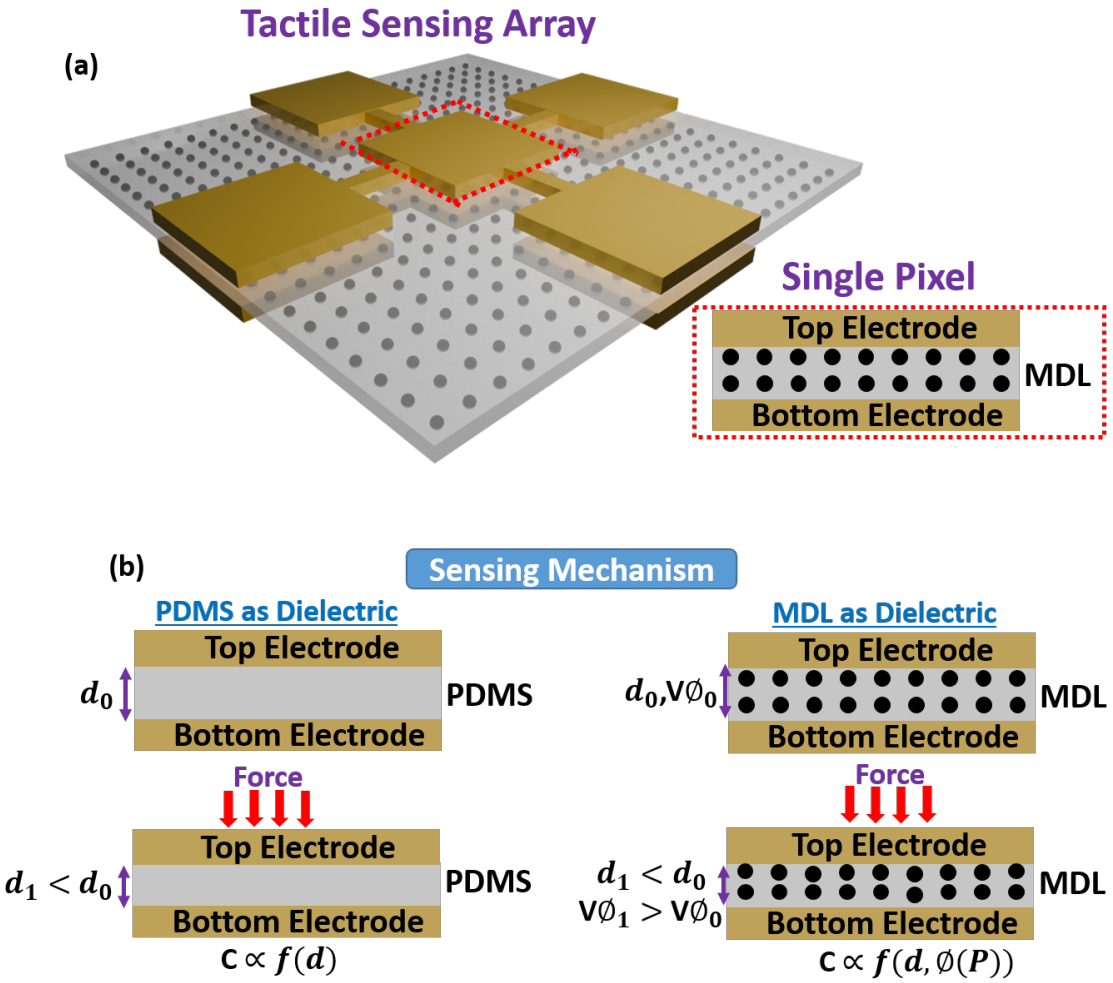


FIGURE 5.1: (a) Conceptual schematic of the tactile sensing array and a single pixel showing different layers of the pixel. (b) Schematic describing the sensing mechanism of the device. One device has PDMS as a dielectric, while another has MDL as a dielectric. The capacitance in the former device is a function of the gap between the electrodes, while the latter device capacitance is a function of both the gap and the volume fraction of NPs.

1. **Geometric Effect:** The compression reduces the separation distance (d) between the two electrodes, which directly increases the capacitance. This is the primary mechanism in conventional capacitive sensors using pure PDMS.

2. **Dielectric Effect:** In the proposed MDL-based device, compression also increases the volume fraction (ϕ) of the magnetic nanoparticles by reducing the overall volume of the elastomeric matrix. This increased filler concentration

enhances the effective permittivity (ε_{eff}) of the composite layer. The permittivity behavior can be described by an effective medium theory, such as the Maxwell-Garnett approximation for spherical inclusions:

$$\varepsilon_{\text{eff}} = \varepsilon_m \frac{2(1-\phi)\varepsilon_m + (1+2\phi)\varepsilon_i}{(2+\phi)\varepsilon_m + (1-\phi)\varepsilon_i} \tag{5.1}$$

where ε_m and ε_i are the permittivities of the PDMS matrix and filler particles, respectively. This provides a second, synergistic contribution to the capacitance signal.

The key mechanism of this design is the transition from a conventional dielectric, where capacitance is primarily a function of electrode gap ($C \propto 1/d$), to a magnetodielectric composite, where capacitance depends on both the electrode gap and the variable permittivity ($C \propto \varepsilon_{\text{eff}}(\phi)/d$). This dual-response mechanism enables a significantly higher sensitivity to applied pressure compared to conventional designs.

5.3 Finite Element Modelling (FEM)

Finite element modeling (FEM) is performed in COMSOL Multiphysics to validate the operational principle and quantitatively assess device performance. The simulations use a coupled electromechanical approach. The Solid Mechanics module models the dielectric's deformation, while the Electrostatics module computes the resulting capacitance. A model of a single sensing pixel is modelled as a parallel-plate capacitor. Two separate models are developed and compared: one using pure PDMS as the dielectric and another using the magnetodielectric composite (MDL). The bottom electrode is structurally fixed, while a uniformly distributed pressure is

TABLE 5.1: Dimensions and Material Properties

Symbol	Value	Description
W_e	$100\,\mu$m	Width of electrode
L_e	$100\,\mu$m	Length of electrode
A_p	$100 \times 100\,\mu\text{m}^2$	Area of a single pixel
g	$20\,\mu$m	Initial dielectric thickness
PI-2611 material		
E_{PI}	8.5 GPa	Young's modulus
ν_{PI}	0.3	Poisson's coefficient

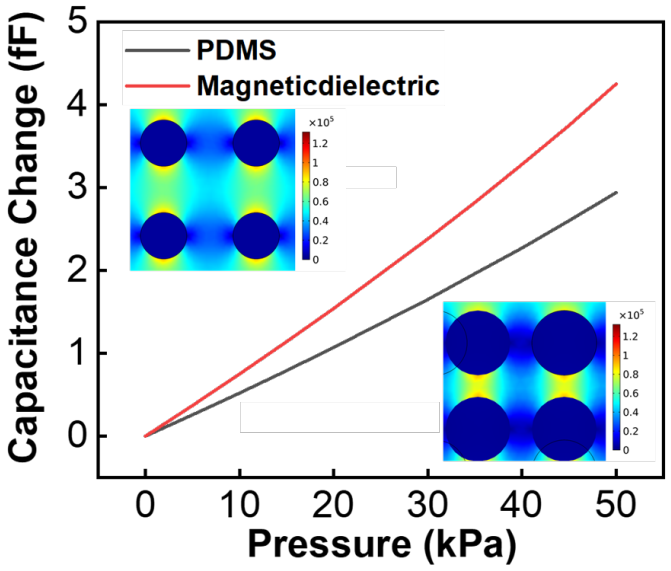


FIGURE 5.2: Comparison of an FEM simulation of a capacitance change of the single pixel with PDMS-only dielectrics and magnetodielectric layer (MDL).

applied to the top surface, ranging from 0 to 50 kPa. Table 5.1 outlines the geometrical and material properties. In the simulation, the dielectric compression increases the nanoparticle volume fraction, which dynamically updates the permittivity in the electrostatics module.

The simulated capacitance change under applied pressure is shown in Figure 5.2. The results quantify the advantage of the MDL, showing an approximately 60% greater capacitance change (at 50 kPa) compared to the PDMS-only structure. The capacitance increase for PDMS is modest and stems primarily from the geometric reduction in electrode separation. In contrast, the MDL exhibits better sensitivity

due to the synergistic combination of this geometric effect and the compression-induced enhancement of its effective permittivity. These simulation results provide validation for the proposed dual-mechanism sensing principle.

5.4 Fabrication Process Flow

The fabrication process is illustrated in Figure 5.3, starting with a temporary handling wafer of silicon (Si). An $\approx 8\mu$m polyimide (PI) layer is spin-coated onto the Si wafer at 2000 rpm for 30 seconds. This is followed by a multi-step curing process: moisture/solvent removal by baking at 90 °C for 90 seconds, initial soft curing at 150 °C for 90 seconds, and final curing at 300 °C for 30 minutes. Then, the temperature is gradually ramped from 150 °C to 300 °C.

The next step involves deposition and patterning of Metal Layer 1 (M1), which forms the bottom electrode of the capacitive sensing array. Since PI surface has comparatively poor adhesion to the sputtered/deposited thin film metals, the surface treatment of PI using plasma RIE in the presence of 10 standard cubic centimetres (SCCM) of O_2 flow at 5 mTorr chamber pressure, 30 °C table temperature and 150 W RF power for 2 minutes is performed. Following surface preparation, a thin layer of Ti/Au (10/150 nm) is deposited using DC sputtering under 25 SCCM Ar flow at 400 W target power. The deposited metal is patterned using photolithography with a positive photoresist (PR) S1813. The metal electrode pattern is then etched using the wet etchant. Subsequently, the PR is removed using acetone. The sample is then rinsed sequentially with isopropanol (IPA) and deionized (DI) water to eliminate residual contaminants, followed by drying under N_2 gas. The dielectric layer consists of a magnetodielectric (MDL) composite, prepared by dispersing magnetic

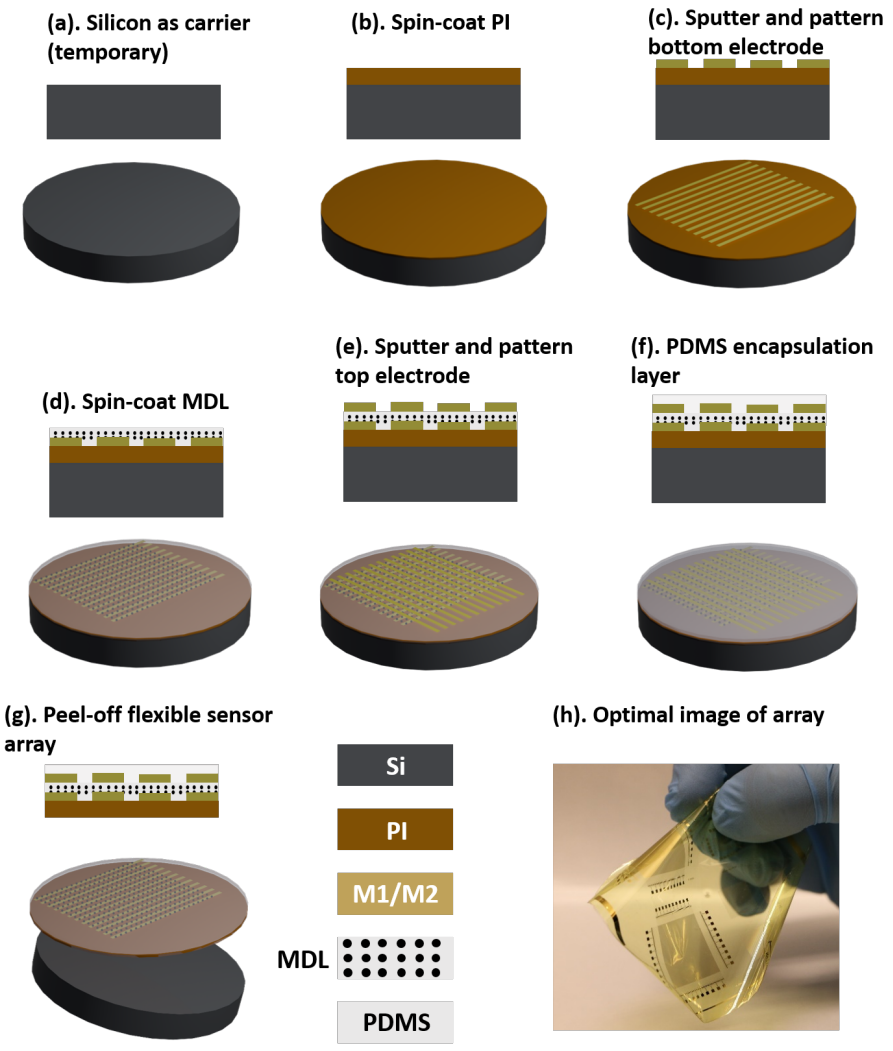


FIGURE 5.3: Schematic illustrating the fabrication process for the flexible high-density sensor array. The process begins with (a) silicon as a temporary carrier. (b) Spin-coating of the polyimide (PI) substrate. (c) Sputtering and patterning of the bottom electrode. (d) Spin-coating of the magnetodielectric layer (MDL). (e) Sputtering and patterning of the top electrode. (f) Spin-coating of PDMS as the encapsulation layer. (g) Finally, peeling off the completed flexible sensor array. (h) Optical image of the fabricated sensor array demonstrating mechanical flexibility.

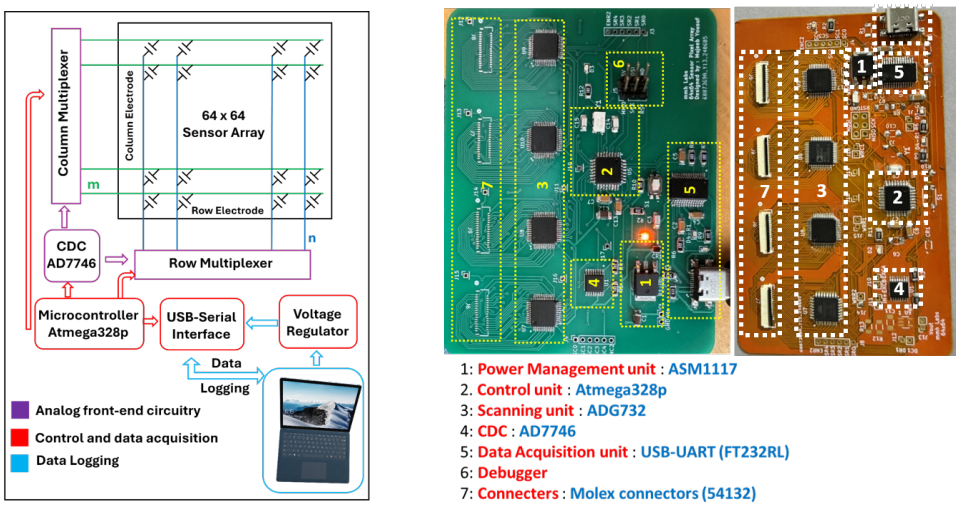
nanoparticles in Sylgard™ 184 PDMS (base: curing agent = 10:1). PDMS is chosen for its biocompatibility and compatibility with cleanroom microfabrication and CMOS processes. The MDL is spin-coated at 2000 rpm for 1 minute and cured at 65 °C for 90 minutes. This low-temperature curing preserves the compressive properties

of the MDL, which can degrade if cured at higher temperatures. The same process used for M1 is repeated to fabricate metal layer 2 (M2) on the PDMS dielectric layer, forming the second set of electrodes. To protect the capacitive pressure sensor array from wear and tear, the top layer is encapsulated with a thin 5–10 μm PDMS layer. Finally, the device is peeled off the Si wafer, completing the fabrication process.

5.5 Readout Circuit Design

Figure 5.4 illustrates the schematic of the readout electronics for the sensor array, focusing on scalability and system-level integration. The sensor array is configured as a cross-bar matrix of 64×64 sensors, where each pixel incorporates an MDL sandwiched between top and bottom electrodes. The readout electronics are implemented on a fully integrated, two-layer flexible PCB that ensures mechanical compliance with curved or deformable surfaces (Figure 5.4(b)). This architecture includes five primary subsystems: an analog front-end, signal processing and control circuitry, power management, data acquisition, and a logging and visualization interface. The analog front-end includes a scanning circuit and a capacitance-to-digital converter (CDC). The scanning circuit utilizes four 32:1 analog bidirectional multiplexers (ADG732), with two dedicated to row selection and two to column selection. This configuration allows assignment of a unique address (C_{mn}) to each pixel in the 64×64 crossbar matrix comprising 4096 sensors. The multiplexers enable sequential signal transmission and capacitance measurement at each pixel. The CDC (AD7746) continuously samples a square-wave excitation to power line m and collects the capacitance data through the readout line n, where each m, n line is selected by the scanning circuit sequentially (Figure 5.4). It operates with the ATmega328P microcontroller using the I^2C communication protocol, enabling efficient

data transfer. The CDC can measure capacitance up to 17 pF with a resolution of 1 fF. Calibration routines are implemented to compensate for parasitics introduced by the PCB and cables, leveraging the capacitive offset and CAPDAC registers of the AD7746 chip to nullify the initial capacitances of all pixels. Signal processing



(a) (b)

FIGURE 5.4: (a) Schematic of the readout electronics for the 64×64 capacitive tactile array, showing multiplexers, CDC, and control circuitry. (b) Flexible two-layer PCB integrating analog front-end, control, and communication modules.

and control are managed by the ATmega328P microcontroller, which coordinates with the multiplexers and handles data logging. The microcontroller sequentially selects pixels via the multiplexers by addressing a specific row and column, thereby assigning a unique address to each pixel. The data acquisition circuitry utilizes the FT232RL chip and a USB-C port to bridge the microcontroller's UART interface with a host device, such as a computer. This setup facilitates serial communication for data transfer, programming, and debugging, enabling monitoring and logging of sensor data. Power to the system is regulated by an ASM1117 linear voltage regulator, which provides a stable 5.0 V output. Figure 5.5 shows the images of the experimental test bench for electromechanical characterization of the sensor array.

The mechanical force applying setup consists of a force gauge (Mark-10) that has a resolution of 1 mN. The force gauge is fixed on the motorized force tester ESM303.

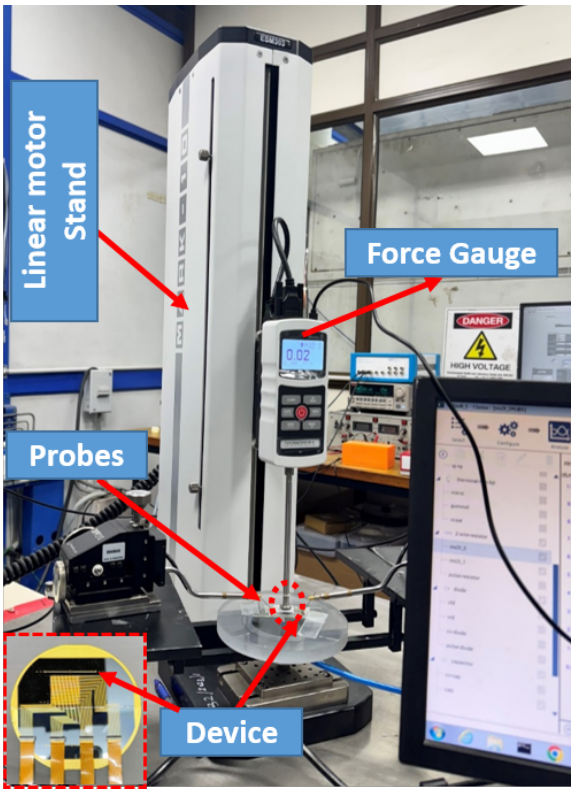
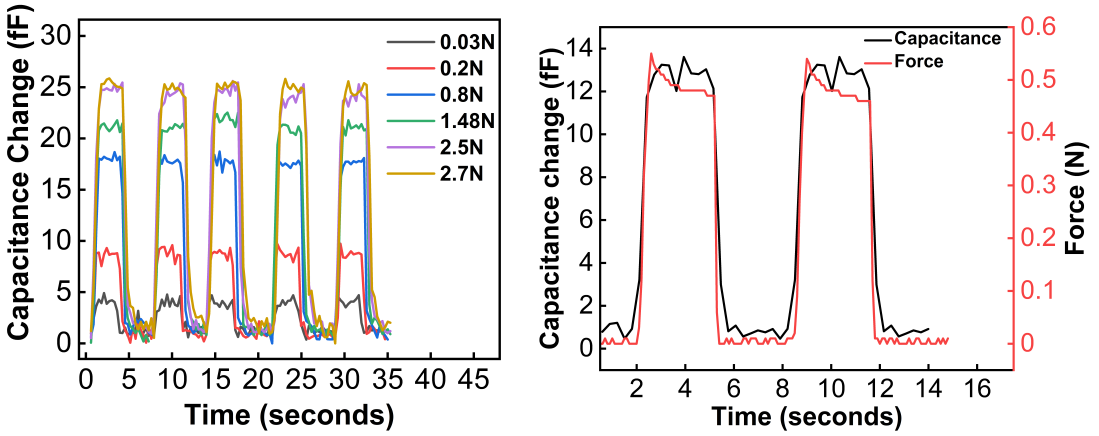


FIGURE 5.5: Experimental setup for electromechanical characterization of the tactile array, including the Mark-10 force gauge (1 mN resolution) mounted on the ESM303 motorized tester.

5.6 Results and Discussion

Figure 5.5 shows a picture of the experimental set-up and a close-up view of the overall sensor array. To evaluate the performance of the sensor array, three types of studies are conducted. First, the capacitance between the top and bottom electrodes of each pixel is measured to assess the electromechanical response of the sensor. Second, repeatability tests are performed on different devices across the wafer to assess the consistency and robustness of the fabrication process. Finally, the array's ability

to perform 2D pressure distribution mapping is tested using the developed readout electronics. The performance of a single pixel is evaluated by analyzing the pressure-



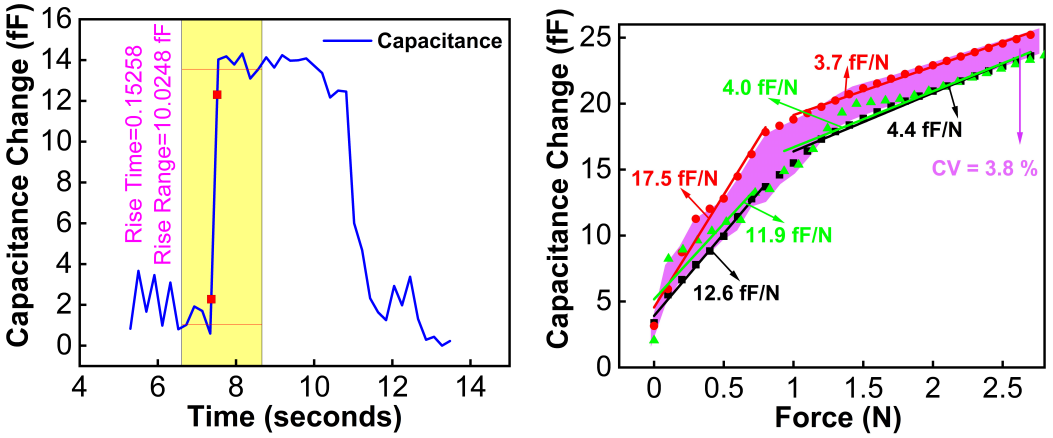
(a) (b)

FIGURE 5.6: Individual (single) pixel characterization. (a) Response of the applied pressure on a single pixel (b) Capacitance change following the dynamic applied force, showing better electromechanical coupling.

capacitance curve. The force is applied using an ESM303 motorized force tester, and the capacitance measurements are performed using a semiconductor parameter analyzer (Keithley 4200-SCS). The electromechanical response of a single sensor pixel is systematically characterized. During each measurement, the applied force is increased to a predefined value, and the corresponding capacitance is recorded. Figure 5.6(a) illustrates the pressure-capacitance relationship for a single pixel, demonstrating a consistent and repeatable increase in capacitance with applied force up to 2.7 N. This response profile results from the combined effect of the geometric reduction in dielectric thickness and the compression-induced enhancement of the MDL's permittivity. The capacitance shows a reliable incremental change across multiple trials at each force level. The response saturates after approximately 2.5 N, beyond which the capacitance change becomes negligible, indicating the operational limit of the sensor's dynamic range. The dynamic performance is evaluated under cyclic loading.

Figure 5.6(b) illustrates the sensor's response to repeated loading and unloading cycles at 0.55 N. The capacitance signal closely follows the profile of the applied force with minimal hysteresis and rapid response time. The sharp transitions observed in both the force and capacitance signals confirm effective electromechanical coupling and the fast recovery of the MDL, highlighting the sensor's suitability for detecting dynamic tactile events.

Figure 5.7(a) illustrates the response time of a single pixel when subjected to a dynamic load measured to be approximately 150 ms, which aligns well with previously reported values [172]. The response time of the device is influenced by several factors, including the data acquisition system's speed, the rate at which dynamic load is applied to the sensor, and the properties of the dielectric film used in the sensor. The second study focuses on repeatability testing of three different devices from different regions on the same wafer. As seen from Figure 5.7(b), the capacitance curves of all three devices follow closely, providing an initial visual confirmation of consistency. This performance is further characterized in 5.7(b), which illustrates the spatial uniformity across the 4096 pixels of sensor array, where a colour-filled



(a) (b)

FIGURE 5.7: (a) Dynamic time response of a single pixel, showing a response time of 150 ms. (b) Capacitive response of pixels located at different corners of the device.

band visually represents the device-to-device variance. Analysis of three representative devices from different wafer corners confirms good manufacturing consistency at scale. The devices exhibited a consistent dual-region capacitance-force relationship, with a high-sensitivity region (0.1–0.9 N) averaging 14.5 ± 2.2 fF/N and a saturation region (1.0–2.7 N) averaging 4.12 ± 0.38 fF/N. This behavior can be understood by examining the sensor's operational mechanism. The initial high sensitivity is a direct result of the magnetodielectric layer (MDL). Under light compression, the sensor benefits from a synergistic effect: the capacitance increases both from the geometric reduction in electrode separation and from a significant, rapid increase in the MDL's effective permittivity. This permittivity enhancement arises from the reduced interparticle spacing of the magnetic nanoparticles. The transition to the lower sensitivity saturation region is attributed to two main factors. First, the magnetodielectric composite exhibits progressive stiffening, diminishing the geometric contribution to the capacitance change. Second, the dielectric enhancement saturates as the nanoparticle network approaches its maximum packing density. The tight distribution of these responses, coupled with an impressive 8.8× average dynamic range across extreme spatial positions, confirms excellent fabrication uniformity. Most significantly, the convergence of the color band in 5.7(b) illustrates how spatial consistency improves under force, culminating in an excellent operational coefficient of variation of just 3.8% at 2.5 N. Statistical analysis validated this wafer-scale uniformity, showing no significant differences between corner devices (ANOVA, $F = 1.138$, $p = 0.326$). This progressive normalization under load indicates that our fabrication process produces consistent mechanical and electrical properties.

To evaluate the sensor's detection limit and operational range, capacitance measurements are performed across a range of applied forces from 0 N to 2.7 N (Figure 5.8). The results demonstrate three key characteristics. First, a clear detection threshold exists at 0.03 N, where the capacitance first deviates from its baseline. Second,

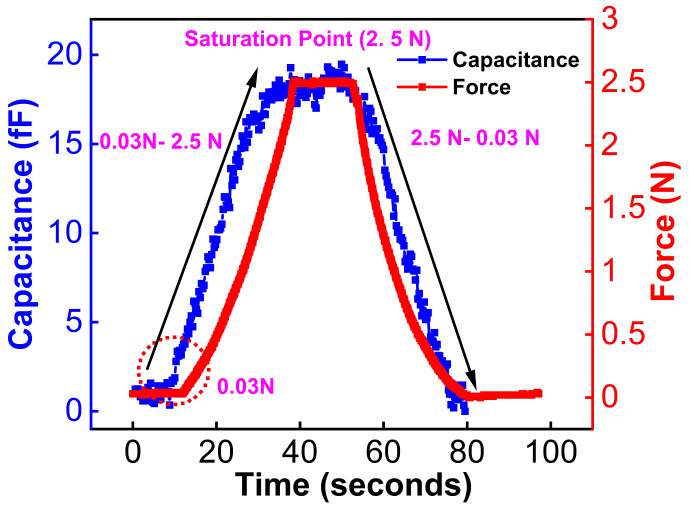
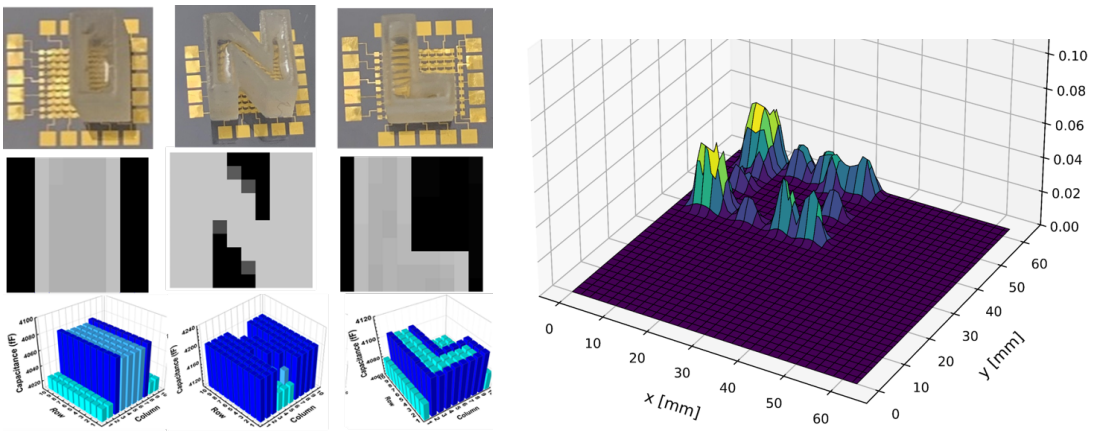


FIGURE 5.8: Capacitance response of the sensor array across the full force range (0–2.7 N), showing a minimum detectable load of 0.03 N and saturation at 2.5 N.

a proportional capacitance-force relationship is maintained throughout the loading phase. Third, the capacitance completely returns to baseline upon force removal, showing minimal hysteresis. The saturation behavior becomes apparent at approximately 2.5 N. At this point, the capacitance plateaus despite further force increases. This performance confirms a wide dynamic range and excellent reversibility. The spatial mapping capability of the high-resolution tactile sensor array is evaluated by applying uniform pressure to 3D-printed letters ("INL"). Figure 5.9 presents the resulting 2D pressure distribution heatmaps, which clearly and accurately replicate the shapes of the stamps. The sensor successfully resolves the distinct spatial features of each character, demonstrating its ability to translate physical contact into a high-fidelity digital pressure image. This capability is further validated using a more complex contour, a circular ring, where the sensor clearly delineates both the inner and outer radii in the pressure heatmap. The sharp definition in these maps confirms the effective spatial resolution and functional uniformity of all 4096 sensing pixels. These findings conclusively demonstrate the potential of this high-density array for advanced applications in flexible E-skins, particularly for tasks requiring detailed texture discrimination and object recognition in wearable devices and



(a) (b)

FIGURE 5.9: 2D pressure mapping using the high-resolution tactile array. Heatmaps correspond to (a) 3D-printed letters "INL". (b) A circular ring profile.

robotics. While the demonstrated 64×64 capacitive array provides sub-millimeter spatial resolution, further scaling of such arrays introduces several practical challenges. As the pixel density increases, parasitic capacitances between neighboring electrodes may lead to electrical crosstalk, which can distort the spatial pressure distribution. In addition, routing a large number of electrode interconnections becomes increasingly complex and may introduce additional parasitic resistance and capacitance. Large arrays also generate significant data throughput, requiring efficient multiplexing and high-speed readout electronics. Furthermore, maintaining uniform sensitivity across all pixels becomes challenging due to possible variations in dielectric thickness and electrode geometry during fabrication. Therefore, careful optimization of electrode design, circuit architecture, and fabrication processes is necessary for scalable implementation of high-density tactile sensor arrays.

5.7 Conclusion

This work presents a sub-mm resolution capacitive sensor array consisting of 64×64 (4096) individually addressable pixels. The sensor array is fabricated on a flexible substrate using a standard MEMS process. Each pixel measures 100 μm x 100 μm, and a magnetodielectric layer is sandwiched between the electrodes. The use of this magneto-dielectric layer enables tunable effective permittivity under mechanical deformation, resulting in enhanced capacitive sensitivity across a wide pressure range. The sensors demonstrate a pressure detection range from 0.37 to 30.86 kPa (0.03 mN to 2.5 N) and a sensitivity of 17.5 fF/N. The array is interfaced with custom-designed readout electronics, forming a fully integrated system. The sensor pixels can potentially be fabricated with reduced critical feature sizes, enabling a higher density of sensors within the same area. With an active area of 2.2 cm × 2.2 cm, the system achieves a device density of approximately 846 sensors/cm^2. Furthermore, the integrated system offers significant upscaling potential by leveraging technologies commonly employed in modern mass-fabrication lines. The three studies are carried out to validate the robustness of the device. First, the capacitance between the top and bottom electrodes of each pixel is measured to verify the array's readout capability. Second, repeatability tests are performed on devices from the same wafer and on devices from three additional wafers to assess the consistency and robustness of the fabrication process. Finally, the array's capability to conduct 2D pressure distribution mapping of the complex contour is demonstrated.

TABLE 5.2: Comparison with Previously Reported Works

Work	**Mechanism**	**Pixel Size** (μm)	**No. of Sensors**	**Range (kPa)**
This Work	Cap	100	4096	0.37-30.86
[165]	Cap	420	256	0-500
[128]	Cap	2000	64	0-2.5
[173]	Cap	4000	16	0-30
[174]	Cap	600	144	0.1-0.6
[175]	Cap+OFET	7500	64	0-5
[176]	Res	2500	16	N/A
[177]	Res	1000	400	0.1-6
[178]	Res+OFET	2540	256	N/A

Chapter 6

Conclusion and Future Outlook

This chapter summarizes the key contributions of this thesis and outlines potential directions for future research in this area.

6.1 Summary of the Research

The objective of this thesis was to develop flexible electromechanical sensors that embody the mechanical adaptability required for Sensor 4.0. A series of devices was designed and fabricated with performance parameters such as sensing range, multimodality, crosstalk suppression, and scalability that limit existing flexible electromechanical sensor technologies. Each device was integrated into a complete system combining sensor, readout, and application demonstration, thereby bridging the gap between material-level innovation and functional platforms. The first device developed in this thesis targeted human-machine interface applications. To overcome the limitations of conventional single-mechanism devices, it combined capacitive and resistive transduction principles, thereby achieving an extended sensing range with

improved sensitivity. An array of devices was fabricated, with each pixel mechanically and electrically isolated to suppress crosstalk, a critical requirement for tactile sensing. The device architecture employed a suspended PEDOT:PSS/LIG/PDMS film over interdigitated electrodes, supported by an SU-8 spacer. A dual-isolation strategy using these SU-8 spacers and a fully parallel, per-channel ADC readout effectively suppressed crosstalk to <0.3%. In operation, the capacitive mode was effective in the low-pressure regime (0.3–15 kPa), achieving a sensitivity of 30 fF/kPa (0.0013 kPa^{-1}). At higher pressures (15–86 kPa), the device switched to piezoresistive mode, delivering a sensitivity of 148 kΩ/kPa (0.03 kPa^{-1}). The sensor was integrated into a complete system via a flexible PCB, where a hierarchical MSP430–ESP32 readout pipeline enabled real-time wireless data acquisition with low latency (50 $\pm$ 5 ms).

Building on this, the thesis advanced towards human motion monitoring, where new requirements emerged: the ability to sense strain directionality and proximity in addition to pressure. To address these challenges, two devices were developed. Unlike conventional direction-insensitive sensors, the first device employed an asymmetric design to achieve direction-sensitive strain sensing, a key requirement for applications such as artificial prosthetics and rehabilitation. By incorporating a μ-meshed PDMS dielectric layer, the device could discriminate strain directionality, offering enhanced functionality compared to symmetric strain sensors. The second device combined strain sensing with non-contact proximity sensing, enabling multimodal operation within a single platform. In addition to its multifunctionality, this device was fabricated through a single-step process and required only a single readout interface circuit. Its strain-sensing layer was realized by introducing a magnetodielectric (MDL) composite, where nanoparticles were homogeneously dispersed in PDMS. This configuration enhanced sensitivity (strain $\approx$4$\times$, proximity $\approx$1.5$\times$) and

broadened the dynamic range (6–20 mm). The distinct repositioning of nanoparticles under varying loads improved strain responsivity compared to a PDMS-only sensing layer.

While the above devices performed well for static pressure stimuli, they were inherently limited in capturing dynamic signals, which are critical for tasks such as robotic gripping or human biomechanics. To address this challenge, two devices were proposed. The first device was fabricated through a low-cost process using porous PDMS embedded with BTO piezoelectric nanoparticles. Simulation studies were employed to optimize porosity and the BTO/PDMS ratio, resulting in a twofold increase in sensitivity and a dynamic sensing range of 5–100 kPa. While effective for dynamic signals, this device could not capture static stimuli. To overcome this, a second device was developed that combined capacitive and piezoelectric transduction within a single platform, enabling detection of both static and dynamic pressures. A μ-pyramidal microengineered capacitive layer provided high sensitivity to static and subtle stimuli, whereas a MoS_2/PVDF piezoelectric layer was responsible for detecting dynamic and high-frequency stimuli. The device achieved a working range of 1–140 kPa with sensitivities of 30 fF/kPa in capacitive mode and 160 mV/kPa in piezoelectric mode. As a proof of concept, the multimodal device was demonstrated in robotic gripping tasks, successfully distinguishing between grabbing, holding, and slipping events.

Finally, the thesis addressed the need for scalability and high-resolution tactile mapping, introducing a sub-millimeter resolution capacitive array. The final section of the thesis presented a sub-millimeter-resolution, high-density capacitive sensing array (4096 pixels) for next-generation applications requiring spatial resolution comparable to that of human skin. The platform achieved fine-grained surface texture detection, pushing the limits of resolution and integration in flexible tactile systems. The high-resolution array comprises 64 $\times$ 64 individually addressable pixels over a

2.5 cm^2 active area, with each pixel measuring 100 μm $\times$ 100 μm. The sensors were fabricated through a standard MEMS process, operating on a capacitive mechanism with a pressure detection range of 0.03 mN–2.5 N (0.37–30.86 kPa) and a sensitivity of 17.5 fF/N. A custom circuit was developed to individually address each pixel and mitigate parasitic capacitance, enabling accurate readout in the femtofarad range. The system was first implemented on a rigid PCB and later adapted to a flexible PCB to mechanically conform to curved surfaces. The integrated array successfully reconstructed the morphology of a circular ring with 100 μm spatial resolution, demonstrating its capability for high-resolution tactile mapping.

6.2 Scope for Future Work

This thesis focused on the development of flexible electromechanical sensors for human-motion monitoring and human–machine interfaces. The flexible electromechanical sensors form the core component of Sensor 4.0, representing intelligent and adaptive sensing nodes. The different device designs and material optimization were carried out to tailor the response according to their applications. Verification was done by a series of simulations and experiments to analyze their utility. In addition, a complete integrated system was developed for each of the devices. Nevertheless, the research directions outlined here provide opportunities for extending this work into new and transformative domains.

6.2.1 Multi-functional and Multi-modal Devices

Most applications operate in complex environments, where collecting comprehensive environmental and physiological information requires multimodal sensing. A

single-modal sensor is often insufficient in such scenarios, while the integration of multiple sensing mechanisms can improve the quality and reliability of the acquired information. Therefore, multimodal or multi-sensing capability should be a key feature of next-generation flexible devices. There are two strategies to achieve this: (i) integrating multiple sensors into a single device, or (ii) designing a single sensor capable of sensing multiple signals. The choice depends on the complexity of design, fabrication cost, signal conditioning requirements, and the challenge of effectively decoupling multiple signals. Future efforts in this direction will enable flexible sensors to deliver richer datasets, facilitating applications such as intelligent human–machine interaction, advanced prosthetics, and precision healthcare.

6.2.2 Standalone Truly Flexible Electronic Systems: From FHE to Transformational Electronics

At present, most flexible electronic systems incorporate flexible sensors but rely on rigid CMOS chips for data processing. A complete, standalone, flexible electronic system requires both sensors and interfacing circuits to be flexible. Organic electronic systems provide an attractive alternative, but their integration and performance remain limited compared to state-of-the-art CMOS technology. On the other hand, Flexible Hybrid Electronics (FHE) systems combine flexible sensors and flexible PCBs, but the rigid CMOS chips reduce overall flexibility and limit form factor. The next state-of-the-art will be standalone flexible systems where every component, including ICs, is flexible. One approach is to thin down bare-die ICs to less than 50 µm using advanced fabrication techniques such as DRIE, and then integrate these ultra-thin dies onto flexible substrates like polyimide. The integration strategy will depend on the device footprint and the intended application. Heterogeneous integration techniques, including 1D, 2D, 2.5D, and 3D schemes, will

be central to achieving this vision. Such advancements will shift flexible electronics from FHE to truly transformational electronics, combining high-performance CMOS-level processing with the mechanical compliance needed for wearable and implantable systems.

6.2.3 Flexible Electronics for Neural Interfaces

Flexible electronic systems have been widely applied in human–machine interfaces, robotic grippers, and health monitoring. However, one of the most underexplored domains is their use in neural interfaces. Flexible electrodes for brain–computer interaction and brain organoid studies could make significant strides in understanding complex neurophysiological phenomena. Traditional techniques such as patch clamping and rigid microelectrode arrays are not fully compatible with brain organoids. Future research must focus on improving their sensitivity, spatial resolution, and biocompatibility. Flexible electrodes and conformal microelectrode arrays offer the potential to seamlessly attach to the intricate 3D geometry of brain organoids, enabling detailed recording of neuronal interactions within and between networks. This could open new avenues for modeling brain diseases, testing drugs, and advancing neuroprosthetics.

Appendix A

Experimental Setup

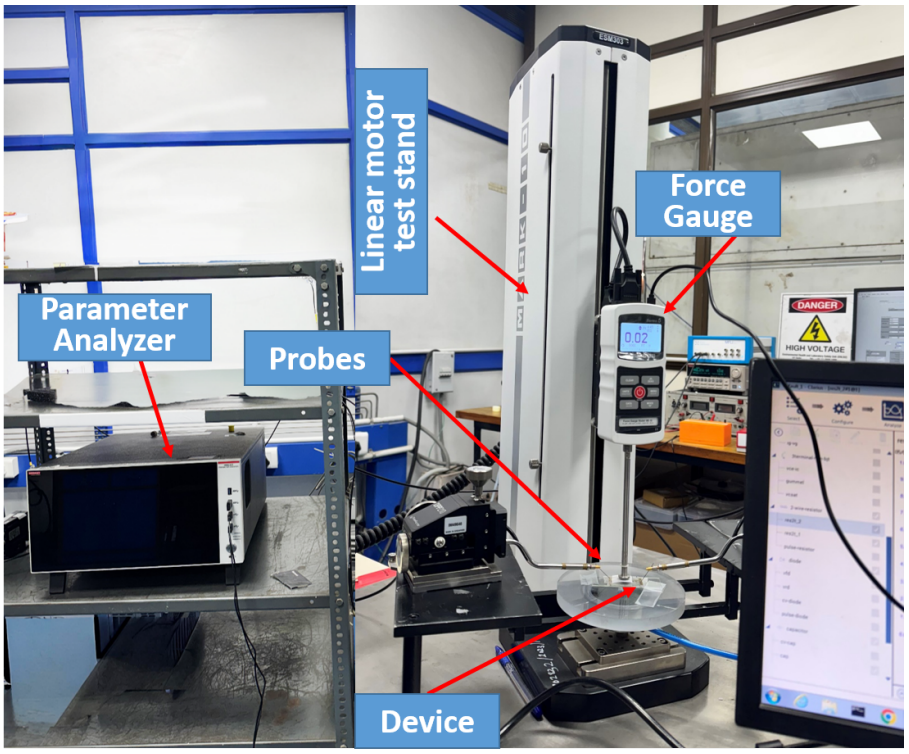


FIGURE A.1: Experimental setup for electromechanical characterization.

A schematic of the custom test station used for electromechanical characterization. The setup is designed to apply precise mechanical loads while simultaneously measuring the electrical response of a device under test (DUT). It consists of four main

components: A linear motor test stand provides controlled vertical displacement to apply a normal force. A force gauge, mounted on the motor, measures the applied load in real-time. A set of micropositioning probes establishes electrical contact with the electrodes of the DUT. A parameter analyzer, connected to the probes, performs high-resolution electrical measurements (e.g., capacitance, resistance). For a typical measurement, the DUT is placed on a stable platform beneath the force gauge. The probes are carefully aligned and lowered onto the contact pads. The linear motor is then commanded to execute a pre-defined motion profile, pressing the force gauge onto the DUT. Throughout this process, the parameter analyzer continuously records the electrical parameters, while the data acquisition system records the simultaneously measured force. This integrated approach provides a complete dataset of the device's response as a function of applied mechanical load, forming the basis for electromechanical performance metrics reported in this work.

Appendix B

Analytical Derivation of Filling Factors

To quantitatively model the pre-contact capacitive response of the suspended hybrid tactile sensor, the Partial Capacitance Method (PCT) is employed. This method determines the effective permittivity (ε_{eff}) of the multi-layer dielectrics in the vicinity of fringing fields. It requires calculation of discrete filling factors (q_i), which represent the fraction of the fringing electric field energy residing within each respective layer. The interdigitated electrodes (IDEs) in our device follow a global spiral pattern. However, their radius of curvature is larger than the spatial period λ.

$$\lambda = 2(w + g) = 400\,\mu m \tag{B.1}$$

with finger width $w = 100\,\mu m$ and gap $g = 100\,\mu m$.

As a result, the local cross-section perpendicular to the electrode fingers can be accurately approximated by a periodic array of parallel, co-planar conducting strips [104]. Because the radius of curvature of the spiral electrodes is significantly larger

than the spatial period λ, the local electric field distribution is effectively equivalent to that of a periodic coplanar strip capacitor. Under this condition, the Schwarz–Christoffel conformal mapping framework derived for linear planar IDE structures remains valid. Consequently, the Partial Capacitance Technique (PCT) can be applied to evaluate the vertical distribution of fringing-field energy [104, 179]. This local linear approximation provides the physical justification required to apply planar IDE models to our device, while the global spiral geometry is separately accounted for by the Bessel function formulation in Equation (2.1) [103].

To evaluate the penetration of the electric field into the surrounding dielectric media, a conformal transformation mapping is used. This transformation maps the physical coordinates to a complex potential plane where the electric field between the electrodes is uniform. For a single dielectric layer of finite height h above the electrode plane, this transformation yields an elliptic modulus defined as

$$k(h) = \frac{\tanh\left(\frac{\pi a}{2h}\right)}{\tanh\left(\frac{\pi(w+a)}{2h}\right)} \tag{B.2}$$

where $a = \frac{g}{2} = 50\,\mu\text{m}$ is the half gap.

In the limit of an infinitely thick homogeneous half-space ($h \to \infty$), this reduces to the free-space modulus

$$k_0 = \frac{a}{w+a} \tag{B.3}$$

By integrating the field energy in the transformed space, the cumulative filling factor $Q(h)$ which represents the fraction of the total electrostatic field energy stored between the electrode plane ($y = 0$) and height ($y = h$) relative to a homogeneous half-space, is obtained analytically as:

$$Q(h) = \frac{1}{2}\frac{K(k'(h))}{K(k(h))}\frac{K(k_0)}{K(k_0')} \tag{B.4}$$

where $K(x)$ is the complete elliptic integral of the first kind, and and $k'(x) = \sqrt{1-x^2}$ is the complementary modulus. For our specific suspended device architecture, the fringing electric field penetrates a four-layer medium composed of the air gap, the PEDOT:PSS layer, the LIG, and the PDMS substrate. Following the top-down analytical framework [180], the height boundaries the height boundaries (h_i) for these layers relative to the IDE surface are as:

$$h_1 = \infty \qquad \text{for the top of the PDMS substrate.} \tag{B.5}$$

$$h_2 = d + t_{\text{PEDOT:PSS}} + t_{\text{LIG}} \qquad \text{for boundary above LIG.} \tag{B.6}$$

$$h_3 = d + t_{\text{PEDOT:PSS}} \qquad \text{for boundary above PEDOT:PSS.} \tag{B.7}$$

$$h_4 = d \qquad \text{for boundary above the air gap.} \tag{B.8}$$

The individual layer filling factors (q_i) used in Equation (2.3) of the chapter 2 represent the cumulative integrated electric field energy from the electrode plane up to each respective layer boundary. As a result, for a semi-infinite upper half-space, this cumulative integral evaluates to $Q(\infty) = \frac{1}{2}$ [104, 179]. Therefore, the cumulative filling factors are assigned as follows:

$$q_1 = Q(h_1) \qquad \text{for the semi-infinite PDMS substrate.} \tag{B.9}$$

$$q_2 = Q(h_2) \qquad \text{for the LIG layer.} \tag{B.10}$$

$$q_3 = Q(h_3) \qquad \text{for the PEDOT:PSS layer.} \tag{B.11}$$

$$q_4 = Q(h_4) \qquad \text{for the air gap.} \tag{B.12}$$

The effective permittivity (ε_{eff}) is accurately modeled as the weighted sum of the layer permittivities.

$$\varepsilon_{\text{eff}} = \varepsilon_{\text{env}} + (\varepsilon_1 - \varepsilon_{\text{env}})q_1 + (\varepsilon_2 - \varepsilon_1)q_2 + (\varepsilon_3 - \varepsilon_2)q_3 + (\varepsilon_4 - \varepsilon_3)q_4 \tag{B.13}$$

where $\varepsilon_{\text{env}} = 1$ represents the background environment. This decomposition is illustrated schematically in Figure 2.2, which shows the multilayer dielectric structure decomposed into individual capacitive contributions weighted by the incremental permittivity differences across each layer boundary.

As applied pressure reduces the air gap d, the cumulative energy fraction in the air gap (q_4) decreases. This physically shifts a larger proportion of the fringing field energy into the higher-permittivity suspended layers, driving the pre-contact capacitive response described in the main text. To explicitly demonstrate this weighted sum, algebraic expansion of the expression yields

$$\varepsilon_{\text{eff}} = \varepsilon_{\text{env}}(1 - q_1) + \varepsilon_1(q_1 - q_2) + \varepsilon_2(q_2 - q_3) + \varepsilon_3(q_3 - q_4) + \varepsilon_4(q_4) \tag{B.14}$$

Because the PDMS is semi-infinite ($q_1 = \frac{1}{2}$), the environmental base term evaluates to $1(1 - \frac{1}{2}) = \frac{1}{2}$, which elegantly represents the fixed capacitive contribution of the lower half-space (the substrate beneath the electrodes). This expanded form clearly isolates the discrete energy weights residing within each physical layer, perfectly capturing the contribution of the lower half-space (1/2), the PDMS ($q_1 - q_2$), LIG ($q_2 - q_3$), PEDOT:PSS ($q_3 - q_4$), and air gap (q_4). The global spiral geometry is then separately accounted for by applying this (ε_{eff}) to the established Bessel function formulation for spiral interdigitated capacitors [180].

The application of this analytical Partial Capacitance Method to our device is highly reliable, as previous literature establishes a $< 5\%$ deviation from exact finite-element

simulations when the layer thickness to spatial period ratio $\frac{d}{\lambda}$ is less than 1 [103]. Under this condition, the vertical variation of the fringing field occurs over a length scale much larger than the electrode pitch, allowing the multilayer dielectric structure to be accurately treated using the Partial Capacitance Technique. Our device satisfies this validity condition comfortably with a zero-pressure ratio of

$$\frac{d}{\lambda} = \frac{48}{400} = 0.12$$

Appendix C

Schematic of Parallel Readout Circuitry

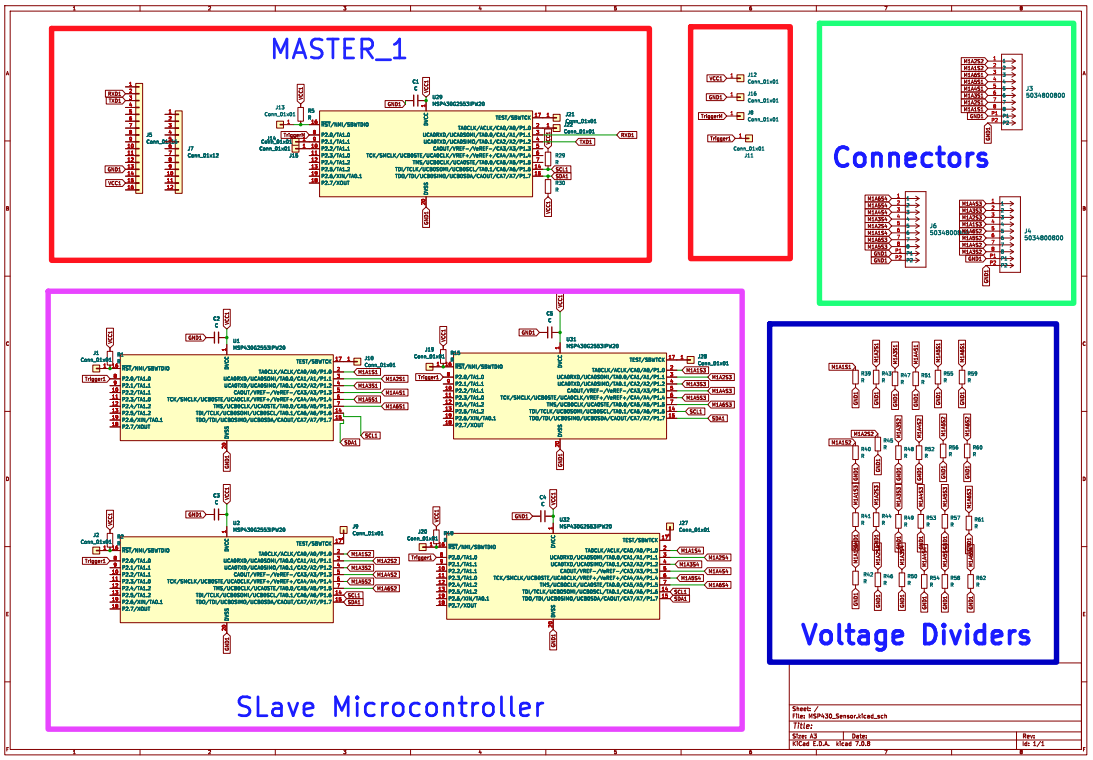


FIGURE C.1: Schematic of MSP430-ESP32 parallel readout architecture.

Bibliography

[1] Y. Luo, M. Abidian, J.-H. Ahn, D. Akinwande, A. Andrews, M. Antonietti, Z. Bao *et al.*, "Technology roadmap for flexible sensors," *ACS Nano*, vol. 17, no. 6, pp. 5211–5295, 2023.

[2] "Flexible sensor market," https://www.alliedmarketresearch.com/flexible-sensor-market-A296083, accessed: 2025-06-02.

[3] Y. Qiu, Y. Tian, S. Sun, J. Hu, Y. Wang, Z. Zhang, A. Liu *et al.*, "Bioinspired, multifunctional dual-mode pressure sensors as electronic skin for decoding complex loading processes and human motions," *Nano Energy*, vol. 78, p. 105337, Dec 2020.

[4] T. S. Vo and K. Kim, "Recent trends of functional composites and structures for electromechanical sensors: A review," *Advanced Intelligent Systems*, vol. 6, no. 5, p. 2300730, 2024.

[5] S. Luo, X. Zhou, X. Tang, J. Li, D. Wei, G. Tai, Z. Chen, T. Liao, J. Fu, D. Wei, and J. Yang, "Microconformal electrode-dielectric integration for flexible ultrasensitive robotic tactile sensing," *Nano Energy*, vol. 80, p. 105580, Feb. 2021.

[6] Q. Su, Q. Zou, Y. Li, Y. Chen, S.-Y. Teng, J. T. Kelleher, R. Nith, P. Cheng, N. Li, W. Liu, S. Dai, Y. Liu, A. Mazursky, J. Xu, L. Jin, P. Lopes, and

S. Wang, "A stretchable and strain-unperturbed pressure sensor for motion interference–free tactile monitoring on skins," *Science Advances*, vol. 7, no. 48, p. eabi4563, Nov. 2021.

[7] S. Yang, C. Zhang, J. Ji, Y. Liu, J. Wang, and Z. Shi, "Performance improvement of flexible pressure sensor based on ordered hierarchical structure array," *Advanced Materials Technologies*, vol. 7, no. 11, p. 2200309, 2022.

[8] S. Wan, H. Bi, Y. Zhou, X. Xie, S. Su, K. Yin, and L. Sun, "Graphene oxide as high-performance dielectric materials for capacitive pressure sensors," *Carbon*, vol. 114, pp. 209–216, Apr. 2017.

[9] Y. Luo, J. Shao, S. Chen, X. Chen, H. Tian, X. Li, L. Wang, D. Wang, and B. Lu, "Flexible capacitive pressure sensor enhanced by tilted micropillar arrays," *ACS Applied Materials & Interfaces*, vol. 11, no. 19, pp. 17 796–17 803, May 2019.

[10] Z. He, W. Chen, B. Liang, C. Liu, L. Yang, D. Lu, Z. Mo, H. Zhu, Z. Tang, and X. Gui, "Capacitive pressure sensor with high sensitivity and fast response to dynamic interaction based on graphene and porous nylon networks," *ACS Applied Materials & Interfaces*, vol. 10, no. 15, pp. 12 816–12 823, Apr. 2018.

[11] J.-Y. Yoo, M.-H. Seo, J.-S. Lee, K.-W. Choi, M.-S. Jo, and J.-B. Yoon, "Industrial grade, bending-insensitive, transparent nanoforce touch sensor via enhanced percolation effect in a hierarchical nanocomposite film," *Advanced Functional Materials*, vol. 28, no. 42, p. 1804721, 2018.

[12] J. Tu, J. Min, Y. Song, C. Xu, J. Li, J. Moore, J. Hanson, E. Hu, T. Parimon, T.-Y. Wang, E. Davoodi, T.-F. Chou, P. Chen, J. J. Hsu, H. B. Rossiter, and W. Gao, "A wireless patch for the monitoring of c-reactive protein in sweat," *Nature Biomedical Engineering*, vol. 7, no. 10, pp. 1293–1306, Oct. 2023.

[13] R. Yin, D. Wang, S. Zhao, Z. Lou, and G. Shen, "Wearable sensors-enabled human–machine interaction systems: From design to application," *Advanced Functional Materials*, vol. 31, no. 11, p. 2008936, Dec 2020.

[14] T. McGee, *Principles and Methods of Temperature Measurement*. New York, NY, USA: John Wiley & Sons, 1988.

[15] "Zhang heng seismoscope," https://www.atlasobscura.com/places/zhang-heng-seismoscope, accessed: 2025-06-02.

[16] A. Sabato, C. Niezrecki, and G. Fortino, "Wireless mems-based accelerometer sensor boards for structural vibration monitoring: A review," *IEEE Sensors Journal*, vol. 17, no. 2, pp. 226–235, Jan 2017.

[17] R. Dahiya, G. Metta, M. Valle, and G. Sandini, "Tactile sensing—from humans to humanoids," *IEEE Transactions on Robotics*, vol. 26, no. 1, pp. 1–20, Jan 2010.

[18] X. Hu, M. Wu, L. Che, J. Huang, H. Li, Z. Liu, M. Li *et al.*, "Nanoengineering ultrathin flexible pressure sensor with superior sensitivity and perfect conformability," *Small*, vol. 19, no. 33, p. 2208015, 2023.

[19] B. Mimoun, V. Henneken, A. van der Horst, and R. Dekker, "Flex-to-rigid (f2r): A generic platform for the fabrication and assembly of flexible sensors for minimally invasive instruments," *IEEE Sensors Journal*, vol. 13, no. 10, pp. 3873–3882, Oct 2013.

[20] Y. Rim, S.-H. Bae, H. Chen, N. De Marco, and Y. Yang, "Recent progress in materials and devices toward printable and flexible sensors," *Advanced Materials*, vol. 28, no. 22, pp. 4415–4440, 2016.

[21] L. Gao, K. Cao, X. Hu, R. Xiao, B. Gan, W. Wang, and Y. Lu, "Nano electromechanical approach for flexible piezoresistive sensor," *Applied Materials Today*, vol. 18, p. 100475, Mar 2020.

[22] Z. Feng, Q. He, X. Wang, Y. Lin, J. Qiu, Y. Wu, and J. Yang, "Capacitive sensors with hybrid dielectric structures and high sensitivity over a wide pressure range for monitoring biosignals," *ACS Applied Materials & Interfaces*, vol. 15, no. 4, pp. 6217–6227, Feb. 2023.

[23] G. Li, D. Chen, C. Li, W. Liu, and H. Liu, "Engineered microstructure derived hierarchical deformation of flexible pressure sensor induces a supersensitive piezoresistive property in broad pressure range," *Advanced Science*, vol. 7, no. 18, p. 2000154, 2020.

[24] L. Algieri, M. T. Todaro, F. Guido, V. Mastronardi, D. Desmaële, A. Qualtieri, C. Giannini, T. Sibillano, and M. De Vittorio, "Flexible piezoelectric energy-harvesting exploiting biocompatible aln thin films grown onto spin-coated polyimide layers," *ACS Applied Energy Materials*, vol. 1, no. 10, pp. 5203–5210, Oct. 2018.

[25] Y.-T. Jao, P.-K. Yang, C.-M. Chiu, Y.-J. Lin, S.-W. Chen, D. Choi, and Z.-H. Lin, "A textile-based triboelectric nanogenerator with humidity-resistant output characteristic and its applications in self-powered healthcare sensors," *Nano Energy*, vol. 50, pp. 513–520, Aug. 2018.

[26] Y. Guo, S. Gao, W. Yue, C. Zhang, and Y. Li, "Anodized aluminum oxide-assisted low-cost flexible capacitive pressure sensors based on double-sided nanopillars by a facile fabrication method," *ACS Applied Materials & Interfaces*, vol. 11, no. 51, pp. 48 594–48 603, Dec. 2019.

[27] F. Liu, F. Han, L. Ling, J. Li, S. Zhao, T. Zhao, X. Liang, D. Zhu, G. Zhang, R. Sun, D. Ho, and C.-P. Wong, "An omni-healable and highly sensitive capacitive pressure sensor with microarray structure," *Chemistry – A European Journal*, vol. 24, no. 63, pp. 16 823–16 832, 2018.

[28] R. B. Mishra, N. El-Atab, A. M. Hussain, and M. M. Hussain, "Recent progress on flexible capacitive pressure sensors: From design and materials to applications," *Advanced Materials Technologies*, vol. 6, no. 4, p. 2001023, 2021.

[29] X. Cui, Y. Jiang, L. Hu, M. Cao, H. Xie, X. Zhang, F. Huang, Z. Xu, and Y. Zhu, "Synergistically microstructured flexible pressure sensors with high sensitivity and ultrawide linear range for full-range human physiological monitoring," *Advanced Materials Technologies*, vol. 8, no. 1, p. 2200609, 2023.

[30] J. Chen, J. Zhang, Z. Luo, J. Zhang, L. Li, Y. Su, X. Gao, Y. Li, W. Tang, C. Cao, Q. Liu, L. Wang, and H. Li, "Superelastic, sensitive, and low hysteresis flexible strain sensor based on wave-patterned liquid metal for human activity monitoring," *ACS Applied Materials & Interfaces*, vol. 12, no. 19, pp. 22 200–22 211, May 2020.

[31] J. He, P. Xiao, W. Lu, J. Shi, L. Zhang, Y. Liang, C. Pan, S.-W. Kuo, and T. Chen, "A universal high accuracy wearable pulse monitoring system via high sensitivity and large linearity graphene pressure sensor," *Nano Energy*, vol. 59, pp. 422–433, May 2019.

[32] Y. Wu, Y. Ma, H. Zheng, and S. Ramakrishna, "Piezoelectric materials for flexible and wearable electronics: A review," *Materials & Design*, vol. 211, p. 110164, Dec. 2021.

[33] W. Lin, B. Wang, G. Peng, Y. Shan, H. Hu, and Z. Yang, "Skin-inspired piezoelectric tactile sensor array with crosstalk-free row+column electrodes

for spatiotemporally distinguishing diverse stimuli," *Advanced Science*, vol. 8, no. 3, p. 2002817, 2021.

[34] S. Duan, J. Wu, J. Xia, and W. Lei, "Innovation strategy selection facilitates high-performance flexible piezoelectric sensors," *Sensors*, vol. 20, no. 10, p. 2820, Jan. 2020.

[35] X. Hu, X. Yan, L. Gong, F. Wang, Y. Xu, L. Feng, D. Zhang, and Y. Jiang, "Improved piezoelectric sensing performance of p(vdf–trfe) nanofibers by utilizing bto nanoparticles and penetrated electrodes," *ACS Applied Materials & Interfaces*, vol. 11, no. 7, pp. 7379–7386, Feb. 2019.

[36] Y. Yang, H. Pan, G. Xie, Y. Jiang, C. Chen, Y. Su, Y. Wang, and H. Tai, "Flexible piezoelectric pressure sensor based on polydopamine-modified batio3/pvdf composite film for human motion monitoring," *Sensors and Actuators A: Physical*, vol. 301, p. 111789, Jan. 2020.

[37] L. Sun, S. Chen, Y. Guo, J. Song, L. Zhang, L. Xiao, Q. Guan, and Z. You, "Ionogel-based, highly stretchable, transparent, durable triboelectric nanogenerators for energy harvesting and motion sensing over a wide temperature range," *Nano Energy*, vol. 63, p. 103847, Sep. 2019.

[38] W. Choi, I. Yun, J. Jeung, Y. S. Park, S. Cho, D. W. Kim, I. S. Kang, Y. Chung, and U. Jeong, "Stretchable triboelectric multimodal tactile interface simultaneously recognizing various dynamic body motions," *Nano Energy*, vol. 56, pp. 347–356, Feb. 2019.

[39] D. Doganay, M. B. Durukan, M. Cugunlular, O. Cakir, M. O. Cicek, O. Demircioglu, D. Wei, and H. E. Unalan, "Triboelectric nanogenerators from fundamentals to applications," *Nano Energy*, vol. 138, p. 110825, 2025.

[40] G. Wu, X. Li, R. Bao, and C. Pan, "Innovations in tactile sensing: Microstructural designs for superior flexible sensor performance," *Advanced Functional Materials*, vol. 34, no. 44, p. 2405722, 2024.

[41] X. Huang, Z. Yin, and H. Wu, "Structural engineering for high-performance flexible and stretchable strain sensors," *ADVANCED INTELLIGENT SYSTEMS*, vol. 3, no. 5, p. 2000194, May 2021.

[42] Y. Jeong, J. Park, J. Lee, K. Kim, and I. Park, "Ultrathin, biocompatible, and flexible pressure sensor with a wide pressure range and its biomedical application," *ACS Sensors*, vol. 5, no. 2, pp. 481–489, Feb. 2020.

[43] C. Ma, D. Xu, Y.-C. Huang, P. Wang, J. Huang, J. Zhou, W. Liu, S.-T. Li, Y. Huang, and X. Duan, "Robust flexible pressure sensors made from conductive micropyramids for manipulation tasks," *ACS Nano*, vol. 14, no. 10, pp. 12 866–12 876, Oct. 2020.

[44] X. Zhao, S. Zhao, X. Zhang, and Z. Su, "Recent progress in flexible pressure sensors based on multiple microstructures: from design to application," *Nanoscale*, vol. 15, no. 11, pp. 5111–5138, Mar. 2023.

[45] Z. Zhang, X. Gui, Q. Hu, L. Yang, R. Yang, B. Huang, B.-R. Yang, and Z. Tang, "Highly sensitive capacitive pressure sensor based on a micropyramid array for health and motion monitoring," *Advanced Electronic Materials*, vol. 7, no. 7, p. 2100174, 2021.

[46] T. Zhu, W. Xu, C. Peng, L. Sh, and L. Wu, "Mesoporous carbon sphere-enhanced flexible pressure sensor with superior linearity and wide range for wearable health monitoring," *Advanced Electronic Materials*, vol. 11, no. 10, p. 2400985, 2025.

[47] X. Wang, Y. Lu, J. Jiang, C. Lv, H. Fu, and M. Xie, "A flexible piezoelectric pvdf/mxene pressure sensor for roughness discrimination," *IEEE Sensors Journal*, vol. 24, no. 5, pp. 7176–7184, Mar. 2024.

[48] A. Saxena and K. Patra, "Recent developments in stretchable and flexible tactile sensors towards piezoresistive systems: A review," *Polymers for Advanced Technologies*, vol. 35, no. 1, p. e6251, 2024.

[49] M. Jung, S. K. Vishwanath, J. Kim, D.-K. Ko, M.-J. Park, S.-C. Lim, and S. Jeon, "Transparent and flexible mayan-pyramid-based pressure sensor using facile-transferred indium tin oxide for bimodal sensor applications," *Scientific Reports*, vol. 9, no. 1, p. 14040, Oct. 2019.

[50] H.-I. Yeom, J. Kim, G.-J. Jeon, J. Kim, and S.-H. K. Park, "Active-matrix driven flexible pressure sensor array using oxide thin-film diode," *IEEE Electron Device Letters*, vol. 44, no. 5, pp. 801–804, May 2023.

[51] Z. Zhan, R. Lin, V.-T. Tran, J. An, Y. Wei, H. Du, T. Tran, and W. Lu, "Paper/carbon nanotube-based wearable pressure sensor for physiological signal acquisition and soft robotic skin," *ACS Applied Materials & Interfaces*, vol. 9, no. 43, pp. 37 921–37 928, Nov. 2017.

[52] H. Yuan, Q. Zhang, Y. Li, X. Zhang, D. Li, Z. Qian, L. Ren, and L. Ren, "Porous bone structure inspired biomimetic flexible piezoresistive sensor with high sensitivity for motion monitoring," *Journal of Bionic Engineering*, vol. 22, no. 3, pp. 1322–1337, May 2025.

[53] S. C. B. Mannsfeld, B. C.-K. Tee, R. M. Stoltenberg, C. V. H.-H. Chen, S. Barman, B. V. O. Muir, A. N. Sokolov, C. Reese, and Z. Bao, "Highly sensitive flexible pressure sensors with microstructured rubber dielectric layers," *Nature Materials*, vol. 9, no. 10, pp. 859–864, Oct. 2010.

[54] C. Pang, J. H. Koo, A. Nguyen, J. M. Caves, M.-G. Kim, A. Chortos, K. Kim, P. J. Wang, J. B.-H. Tok, and Z. Bao, "Highly skin-conformal microhairy sensor for pulse signal amplification," *Advanced Materials*, vol. 27, no. 4, pp. 634–640, 2015.

[55] Y. Cao, T. Li, Y. Gu, H. Luo, S. Wang, and T. Zhang, "Fingerprint-inspired flexible tactile sensor for accurately discerning surface texture," *Small*, vol. 14, no. 16, p. 1703902, 2018.

[56] C. Liu, S. Li, Q. Sun, F. Ma, Y. Sun, Y. Zhang, L. Xie, Y. Huang, X. Yang, and X. Hao, "High-sensitivity capacitive flexible tactile sensor based on hemispherical shell microstructure and zno/rtv composite dielectric layer," *ACS Applied Electronic Materials*, vol. 6, no. 5, pp. 3440–3453, May 2024.

[57] L. Liao, S. Zhou, J. Yang, Z. Wang, J. Li, Z. Qiu, Z. Yu, C. Yang, H. Wang, and L. Wen, "A flexible pressure sensor based on an interlocked micropillars array with secondary nanoprotrusions for health monitoring," *IEEE Transactions on Instrumentation and Measurement*, vol. 73, pp. 1–9, 2024.

[58] R. Chen, T. Luo, J. Wang, R. Wang, C. Zhang, Y. Xie, L. Qin, H. Yao, and W. Zhou, "Nonlinearity synergy: An elegant strategy for realizing high-sensitivity and wide-linear-range pressure sensing," *Nature Communications*, vol. 14, no. 1, p. 6641, Oct. 2023.

[59] J. He, Y. Zhang, R. Zhou, L. Meng, T. Chen, W. Mai, and C. Pan, "Recent advances of wearable and flexible piezoresistivity pressure sensor devices and its future prospects," *Journal of Materiomics*, vol. 6, no. 1, pp. 86–101, Mar. 2020.

[60] J. Weichart, C. Roman, and C. Hierold, "Tactile sensing with scalable capacitive sensor arrays on flexible substrates," *Journal of Microelectromechanical Systems*, vol. 30, no. 6, pp. 915–929, Dec. 2021.

[61] Y. Wan, Y. Wang, and C. F. Guo, "Recent progresses on flexible tactile sensors," *Materials Today Physics*, vol. 1, pp. 61–73, Jun. 2017.

[62] T. Çaykara, M. G. Sande, N. Azoia, L. R. Rodrigues, and C. J. Silva, "Exploring the potential of polyethylene terephthalate in the design of antibacterial surfaces," *Medical Microbiology and Immunology*, vol. 209, no. 3, pp. 363–372, Jun. 2020.

[63] Z. Dong, Q. He, D. Shen, Z. Gong, D. Zhang, W. Zhang, T. Ono, and Y. Jiang, "Microfabrication of functional polyimide films and microstructures for flexible mems applications," *Microsystems & Nanoengineering*, vol. 9, no. 1, p. 31, Mar. 2023.

[64] Y. Zhu, S. Murali, W. Cai, X. Li, J. W. Suk, J. R. Potts, and R. S. Ruoff, "Graphene and graphene oxide: Synthesis, properties, and applications," *Advanced Materials*, vol. 22, no. 35, pp. 3906–3924, 2010.

[65] M. Luo, M. Li, Y. Li, K. Chang, K. Liu, Q. Liu, Y. Wang, Z. Lu, X. Liu, and D. Wang, "In-situ polymerization of ppy/cellulose composite sponge with high elasticity and conductivity for the application of pressure sensor," *Composites Communications*, vol. 6, pp. 68–72, Dec. 2017.

[66] J.-S. Yang, M.-H. Seo, M.-S. Jo, K.-W. Choi, J.-S. Lee, M.-K. Chung, B.-J. Koo, J.-Y. Yoo, and J.-B. Yoon, "Enhanced percolation effect in sub-100 nm nanograting structure for high-performance bending insensitive flexible pressure sensor," *Advanced Electronic Materials*, vol. 11, no. 10, p. 2400980, 2025.

[67] Y. Guo, Z. Guo, M. Zhong, P. Wan, W. Zhang, and L. Zhang, "A flexible wearable pressure sensor with bioinspired microcrack and interlocking for full-range human–machine interfacing," *Small*, vol. 14, no. 44, p. 1803018, 2018.

[68] R. Rahimi, M. Ochoa, W. Yu, and B. Ziaie, "Highly stretchable and sensitive unidirectional strain sensor via laser carbonization," *ACS Applied Materials & Interfaces*, vol. 7, no. 8, pp. 4463–4470, Mar. 2015.

[69] L. Yang, X. Chen, A. Dutta, H. Zhang, Z. Wang, M. Xin, S. Du, G. Xu, and H. Cheng, "Thermoelectric porous laser-induced graphene-based strain-temperature decoupling and self-powered sensing," *Nature Communications*, vol. 16, no. 1, p. 792, Jan. 2025.

[70] M. A. Zahed, S. C. Barman, P. S. Das, M. Sharifuzzaman, H. S. Yoon, S. H. Yoon, and J. Y. Park, "Highly flexible and conductive poly (3, 4-ethylene dioxythiophene)-poly (styrene sulfonate) anchored 3-dimensional porous graphene network-based electrochemical biosensor for glucose and ph detection in human perspiration," *Biosensors and Bioelectronics*, vol. 160, p. 112220, Jul. 2020.

[71] Y. Wang, C. Zhu, R. Pfattner, H. Yan, L. Jin, S. Chen, F. Molina-Lopez, F. Lissel, J. Liu, N. I. Rabiah, Z. Chen, J. W. Chung, C. Linder, M. F. Toney, B. Murmann, and Z. Bao, "A highly stretchable, transparent, and conductive polymer," *Science Advances*, vol. 3, no. 3, p. e1602076, Mar. 2017.

[72] A. Bouhamed, N. Jöhrmann, S. Naifar, B. Böhm, O. Hellwig, B. Wunderle, and O. Kanoun, "Collaborative filler network for enhancing the performance of batio3/pdms flexible piezoelectric polymer composite nanogenerators," *Sensors*, vol. 22, no. 11, p. 4181, Jan. 2022.

[73] M. Nasui, R. B. Sonher, T. Petrisor, E. Ware, E. G. Tuns, R. Pacurar, and M. S. Gabor, "New approach for oriented batio3 thin films with piezoelectric properties through chemical synthesis," *Journal of Alloys and Compounds*, vol. 1036, p. 182008, Jul. 2025.

[74] P. N. Vakil, F. Muhammed, D. Hardy, T. J. Dickens, S. Ramakrishnan, and G. F. Strouse, "Dielectric properties for nanocomposites comparing commercial and synthetic ni- and fe3o4-loaded polystyrene," *ACS Omega*, vol. 3, no. 10, pp. 12 813–12 823, Oct. 2018.

[75] S. K. Subudhi, B. Zhao, X. Wang, J. Ting, I. Takeuchi, A. Dasgupta, and S. Das, "Flexible and twistable free-standing pdms-magnetic-nanoparticle-based soft magnetic films with robust magnetic properties," *Flexible and Printed Electronics*, vol. 9, no. 1, p. 015013, Mar. 2024.

[76] G. Schwartz, B. C.-K. Tee, J. Mei, A. L. Appleton, D. H. Kim, H. Wang, and Z. Bao, "Flexible polymer transistors with high pressure sensitivity for application in electronic skin and health monitoring," *Nature Communications*, vol. 4, no. 1, p. 1859, May 2013.

[77] P. Ramanathan Nagarajan, B. George, and V. J. Kumar, "An improved direct digital converter for bridge-connected resistive sensors," *IEEE Sensors Journal*, vol. 16, no. 10, pp. 3679–3688, May 2016.

[78] V. Sreenath, K. Semeerali, and B. George, "A resistive sensor readout circuit with intrinsic insensitivity to circuit parameters and its evaluation," *IEEE Transactions on Instrumentation and Measurement*, vol. 66, no. 7, pp. 1719–1727, Jul. 2017.

[79] P. R. Nagarajan, B. George, and V. J. Kumar, "Improved single-element resistive sensor-to-microcontroller interface," *IEEE Transactions on Instrumentation and Measurement*, vol. 66, no. 10, pp. 2736–2744, Oct. 2017.

[80] "Ad7746 | datasheet and product info 24-bit, 2 channel capacitance to digital converter | analog devices," https://www.analog.com/en/products/ad7746.html.

[81] K. Kwon, J. U. Kim, S. M. Won, J. Zhao, R. Avila, H. Wang, K. S. Chun, H. Jang, K. H. Lee, J.-H. Kim, S. Yoo, Y. J. Kang, J. Kim, J. Lim, Y. Park, W. Lu, T.-i. Kim, A. Banks, Y. Huang, and J. A. Rogers, "A battery-less wireless implant for the continuous monitoring of vascular pressure, flow rate and temperature," *Nature Biomedical Engineering*, vol. 7, no. 10, pp. 1215–1228, Oct. 2023.

[82] Y. Yu, J. Li, S. A. Solomon, J. Min, J. Tu, W. Guo, C. Xu, Y. Song, and W. Gao, "All-printed soft human-machine interface for robotic physicochemical sensing," *Science Robotics*, vol. 7, no. 67, p. eabn0495, Jun. 2022.

[83] Y. H. Jung, J.-Y. Yoo, A. Vázquez-Guardado, J.-H. Kim, J.-T. Kim, H. Luan, M. Park, J. Lim, H.-S. Shin, C.-J. Su, R. Schloen, J. Trueb, R. Avila, J.-K. Chang, D. S. Yang, Y. Park, H. Ryu, H.-J. Yoon, G. Lee, H. Jeong, J. U. Kim, A. Akhtar, J. Cornman, T.-i. Kim, Y. Huang, and J. A. Rogers, "A wireless haptic interface for programmable patterns of touch across large areas of the skin," *Nature Electronics*, vol. 5, no. 6, pp. 374–385, Jun. 2022.

[84] J.-Y. Yoo, S. Oh, W. Shalish, W.-Y. Maeng, E. Cerier, E. Jeanne, M.-K. Chung, S. Lv, Y. Wu, S. Yoo, A. Tzavelis, J. Trueb, M. Park, H. Jeong, E. Okunzuwa, S. Smilkova, G. Kim, J. Kim, G. Chung, Y. Park, A. Banks, S. Xu, G. M. Sant'Anna, D. E. Weese-Mayer, A. Bharat, and J. A. Rogers,

"Wireless broadband acousto-mechanical sensing system for continuous physiological monitoring," *Nature Medicine*, vol. 29, no. 12, pp. 3137–3148, Dec. 2023.

[85] H. Zhang, H. Zhao, X. Zhao, C. Xu, D. Franklin, A. Vázquez-Guardado, W. Bai, J. Zhao, K. Li, G. Monti, W. Lu, A. Kobeissi, L. Tian, X. Ning, X. Yu, S. Mehta, D. Chanda, Y. Huang, S. Xu, B. E. Perez White, and J. A. Rogers, "Biocompatible light guide-assisted wearable devices for enhanced uv light delivery in deep skin," *Advanced Functional Materials*, vol. 31, no. 23, p. 2100576, 2021.

[86] E. Shirzaei Sani, C. Xu, C. Wang, Y. Song, J. Min, J. Tu, S. A. Solomon, J. Li, J. L. Banks, D. G. Armstrong, and W. Gao, "A stretchable wireless wearable bioelectronic system for multiplexed monitoring and combination treatment of infected chronic wounds," *Science Advances*, vol. 9, no. 12, p. eadf7388, Mar. 2023.

[87] W. Ouyang, W. Lu, Y. Zhang, Y. Liu, J. U. Kim, H. Shen, Y. Wu, H. Luan, K. Kilner, S. P. Lee, Y. Lu, Y. Yang, J. Wang, Y. Yu, A. J. Wegener, J. A. Moreno, Z. Xie, Y. Wu, S. M. Won, K. Kwon, C. Wu, W. Bai, H. Guo, T.-l. Liu, H. Bai, G. Monti, J. Zhu, S. R. Madhvapathy, J. Trueb, M. Stanslaski, E. M. Higbee-Dempsey, I. Stepien, N. Ghoreishi-Haack, C. R. Haney, T.-i. Kim, Y. Huang, R. Ghaffari, A. R. Banks, T. C. Jhou, C. H. Good, and J. A. Rogers, "A wireless and battery-less implant for multimodal closed-loop neuromodulation in small animals," *Nature Biomedical Engineering*, vol. 7, no. 10, pp. 1252–1269, Oct. 2023.

[88] C. Y. Han, W. M. Tang, and P.-T. Lai, "High-mobility pentacene organic thin-film transistors achieved by reducing remote phonon scattering and surface-roughness scattering," *Applied Surface Science*, vol. 544, p. 148656, Apr. 2021.

[89] Y. Wang, T. Hasegawa, H. Matsumoto, and T. Michinobu, "Significant improvement of unipolar n-type transistor performances by manipulating the coplanar backbone conformation of electron-deficient polymers via hydrogen bonding," *Journal of the American Chemical Society*, vol. 141, no. 8, pp. 3566–3575, Feb. 2019.

[90] Y. Wang, H. Guo, A. Harbuzaru, M. A. Uddin, I. Arrechea-Marcos, S. Ling, J. Yu, Y. Tang, H. Sun, J. T. López Navarrete, R. P. Ortiz, H. Y. Woo, and X. Guo, "(semi)ladder-type bithiophene imide-based all-acceptor semiconductors: Synthesis, structure–property correlations, and unipolar n-type transistor performance," *Journal of the American Chemical Society*, vol. 140, no. 19, pp. 6095–6108, May 2018.

[91] U. K. Das and M. M. Hussain, "Benchmarking silicon finfet with the carbon nanotube and 2d-fets for advanced node cmos logic application," *IEEE Transactions on Electron Devices*, vol. 68, no. 7, pp. 3643–3648, Jul. 2021.

[92] "Polyimide films | dupont," https://www.dupont.com/electronics-industrial/polyimide-films.html/general/H-38479-4.pdf#headingacc1.

[93] S. Lee, S. Franklin, F. A. Hassani, T. Yokota, M. O. G. Nayeem, Y. Wang, R. Leib, G. Cheng, D. W. Franklin, and T. Someya, "Nanomesh pressure sensor for monitoring finger manipulation without sensory interference," *Science*, vol. 370, no. 6519, pp. 966–970, Nov. 2020.

[94] J.-S. Yang, M.-K. Chung, J.-Y. Yoo, M.-U. Kim, B.-J. Kim, M.-S. Jo, S.-H. Kim, and J.-B. Yoon, "Interference-free nanogap pressure sensor array with

high spatial resolution for wireless human-machine interfaces applications," *Nature Communications*, vol. 16, no. 1, p. 2024, Feb. 2025.

[95] S. Pyo, J. Lee, K. Bae, S. Sim, and J. Kim, "Recent progress in flexible tactile sensors for human-interactive systems: From sensors to advanced applications," *Advanced Materials*, vol. 33, no. 47, p. 2005902, 2021.

[96] J. Shi, Y. Dai, Y. Cheng, S. Xie, G. Li, Y. Liu, J. Wang, R. Zhang, N. Bai, M. Cai, Y. Zhang, Y. Zhan, Z. Zhang, C. Yu, and C. F. Guo, "Embedment of sensing elements for robust, highly sensitive, and cross-talk–free iontronic skins for robotics applications," *Science Advances*, vol. 9, no. 9, p. eadf8831, Mar. 2023.

[97] S. Yu, L. Li, J. Wang, E. Liu, J. Zhao, F. Xu, Y. Cao, and C. Lu, "Light-boosting highly sensitive pressure sensors based on bioinspired multiscale surface structures," *Advanced Functional Materials*, vol. 30, no. 16, p. 1907091, 2020.

[98] M. Chang, L. Li, F. Fan, K. Guo, and E. Tang, "Effect of electrode/polymer interface properties on electromechanical responses of polymer sensing units," *Tribology International*, vol. 209, p. 110670, Sep. 2025.

[99] F. Zhang, K. Yang, Z. Pei, Y. Wu, S. Sang, Q. Zhang, and H. Jiao, "A highly accurate flexible sensor system for human blood pressure and heart rate monitoring based on graphene/sponge," Jan. 2022.

[100] D. Ge, A. A. Babangida, Z. Hu, L. Zhang, and M. Wang, "Flexible pressure sensor based on a thermally induced wrinkled graphene sandwich structure," *IEEE Sensors Journal*, vol. 22, no. 4, pp. 3040–3051, Feb. 2022.

[101] J. Wang, J. Jiu, M. Nogi, T. Sugahara, S. Nagao, H. Koga, P. He, and K. Suganuma, "A highly sensitive and flexible pressure sensor with electrodes and elastomeric interlayer containing silver nanowires," Feb. 2015.

[102] Y. Li, J. Long, Y. Chen, Y. Huang, and N. Zhao, "Crosstalk-free, high-resolution pressure sensor arrays enabled by high-throughput laser manufacturing," *Advanced Materials*, vol. 34, no. 21, p. 2200517, 2022.

[103] Z. Chen and R. Luo, "Design and implementation of capacitive proximity sensor using microelectromechanical systems technology," *IEEE Transactions on Industrial Electronics*, vol. 45, no. 6, pp. 886–894, Dec. 1998.

[104] R. Igreja and C. J. Dias, "Analytical evaluation of the interdigital electrodes capacitance for a multi-layered structure," *Sensors and Actuators A: Physical*, vol. 112, no. 2, pp. 291–301, May 2004.

[105] J. N. Patel, B. L. Gray, B. Kaminska, N.-C. Wu, and B. D. Gates, "Su-8- and pdms-based hybrid fabrication technology for combination of permanently bonded flexible and rigid features on a single device," *Journal of Micromechanics and Microengineering*, vol. 23, no. 6, p. 065029, May 2013.

[106] Y. Wang, W. Luo, Y. Wen, J. Zhao, C. Chen, Z. Chen, and X.-S. Zhang, "Wearable, washable piezoresistive pressure sensor based on polyurethane sponge coated with composite CNT/CB/TPU," *Materials Today Physics*, vol. 52, p. 101681, 2025.

[107] L.-Q. Tao, K.-N. Zhang, H. Tian, Y. Liu, D.-Y. Wang, Y.-Q. Chen, Y. Yang, and T.-L. Ren, "Graphene-paper pressure sensor for detecting human motions," *ACS Nano*, vol. 11, no. 9, pp. 8790–8795, 2017.

[108] Y. Song, H. Chen, Z. Su, X. Chen, L. Miao, J. Zhang, X. Cheng, and H. Zhang, "Highly compressible integrated supercapacitor–piezoresistance-sensor system with CNT–PDMS sponge for health monitoring," *Small*, vol. 13, no. 39, p. 1702091, 2017.

[109] Y. Zhu, M. C. Hartel, N. Yu, P. R. Garrido, S. Kim, J. Lee, P. Bandaru, S. Guan, H. Lin, S. Emaminejad, N. R. deBarros, S. Ahadian, H.-J. Kim, W. Sun, V. Jucaud, M. R. Dokmeci, P. S. Weiss, R. Yan, and A. Khademhosseini, "Epidermis-inspired wearable piezoresistive pressure sensors using reduced graphene oxide self-wrapped copper nanowire networks," *Small Methods*, vol. 6, no. 1, p. 2100900, 2022.

[110] S. Pyo, J. Choi, and J. Kim, "Flexible, transparent, sensitive, and crosstalk-free capacitive tactile sensor array based on graphene electrodes and air dielectric," *Advanced Electronic Materials*, vol. 4, no. 1, p. 1700427, 2018.

[111] S. C. Mukhopadhyay, "Wearable sensors for human activity monitoring: A review," *IEEE Sensors Journal*, vol. 15, no. 3, pp. 1321–1330, 2015.

[112] P. Maiolino, M. Maggiali, G. Cannata, G. Metta, and L. Natale, "A flexible and robust large scale capacitive tactile system for robots," *IEEE Sensors Journal*, vol. 13, no. 10, pp. 3910–3917, 2013.

[113] J. Platkiewicz, H. Lipson, and V. Hayward, "Haptic edge detection through shear," *Scientific reports*, vol. 6, no. 1, p. 23551, 2016.

[114] M. Mimura, T. Ohura, M. Takahashi, R. Kajiwara, and N. Ohura Jr, "Mechanism leading to the development of pressure ulcers based on shear force and pressures during a bed operation: influence of body types, body positions, and knee positions," *Wound repair and regeneration*, vol. 17, no. 6, pp. 789–796, 2009.

[115] S. Del Din, A. Godfrey, C. Mazzà, S. Lord, and L. Rochester, "Free-living monitoring of parkinson's disease: Lessons from the field," *Movement Disorders*, vol. 31, no. 9, pp. 1293–1313, 2016.

[116] A. J. Espay, P. Bonato, F. B. Nahab, W. Maetzler, J. M. Dean, J. Klucken, B. M. Eskofier, A. Merola, F. Horak, A. E. Lang, R. Reilmann, J. Giuffrida, A. Nieuwboer, M. Horne, M. A. Little, I. Litvan, T. Simuni, E. R. Dorsey, M. A. Burack, K. Kubota, A. Kamondi, C. Godinho, J.-F. Daneault, G. Mitsi, L. Krinke, J. M. Hausdorff, B. R. Bloem, S. Papapetropoulos, and o. b. o. t. M. D. S. T. F. on Technology, "Technology in parkinson's disease: Challenges and opportunities," *Movement Disorders*, vol. 31, no. 9, pp. 1272–1282, 2016.

[117] D. Benfield, E. Lou, and W. A. Moussa, "Parametric evaluation of shear sensitivity in piezoresistive interfacial force sensors," *Journal of Micromechanics and Microengineering*, vol. 21, no. 4, p. 045005, Mar. 2011.

[118] B. Kane, M. Cutkosky, and G. Kovacs, "A traction stress sensor array for use in high-resolution robotic tactile imaging," *Journal of Microelectromechanical Systems*, vol. 9, no. 4, pp. 425–434, 2000.

[119] V. Amoli, S. Young Kim, J. Sung Kim, H. Choi, J. Koo, and D. Hwan Kim, "Biomimetics for high-performance flexible tactile sensors and advanced artificial sensory systems," *Journal of Materials Chemistry C*, vol. 7, no. 47, pp. 14 816–14 844, 2019.

[120] A. Charalambides and S. Bergbreiter, "A novel all-elastomer mems tactile sensor for high dynamic range shear and normal force sensing," *Journal of Micromechanics and Microengineering*, vol. 25, no. 9, p. 095009, Aug. 2015.

[121] S. Pyo, J.-I. Lee, M.-O. Kim, T. Chung, Y. Oh, S.-C. Lim, J. Park, and J. Kim, "Development of a flexible three-axis tactile sensor based on screen-printed carbon nanotube-polymer composite," *Journal of Micromechanics and Microengineering*, vol. 24, no. 7, p. 075012, Jun. 2014.

[122] J. Dargahi and S. Najarian, "Human tactile perception as a standard for artificial tactile sensing—a review," *The International Journal of Medical Robotics and Computer Assisted Surgery*, vol. 1, no. 1, pp. 23–35, Jun. 2004.

[123] M. Chandra, S.-Y. Ke, R. Chen, and C.-Y. Lo, "Doubling the spatial resolution in capacitive tactile sensors," *Journal of Micro/Nanolithography, MEMS, and MOEMS*, vol. 16, no. 3, p. 035001, Jul. 2017.

[124] S. R. A. Ruth, V. R. Feig, H. Tran, and Z. Bao, "Microengineering pressure sensor active layers for improved performance," *Advanced Functional Materials*, vol. 30, no. 39, p. 2003491, 2020.

[125] J. Fernandes, J. Chen, and H. Jiang, "Three-axis capacitive sensor arrays for local and global shear force detection," *Journal of Microelectromechanical Systems*, vol. 30, no. 5, pp. 799–813, Oct. 2021.

[126] J. Wu and N. Yoon Lee, "One-step surface modification for irreversible bonding of various plastics with a poly(dimethylsiloxane) elastomer at room temperature," *Lab on a Chip*, vol. 14, no. 9, pp. 1564–1571, 2014.

[127] Z. H. Zargar and T. Islam, "A novel cross-capacitive sensor for noncontact microdroplet detection," *IEEE Transactions on Industrial Electronics*, vol. 66, no. 6, pp. 4759–4766, 2019.

[128] H.-K. Lee, J. Chung, S.-I. Chang, and E. Yoon, "Normal and shear force measurement using a flexible polymer tactile sensor with embedded multiple

capacitors," *Journal of Microelectromechanical Systems*, vol. 17, no. 4, pp. 934–942, 2008.

[129] A. Chortos, J. Liu, and Z. Bao, "Pursuing prosthetic electronic skin," *Nature Materials*, vol. 15, no. 9, pp. 937–950, Sep. 2016.

[130] K. Sanderson, "Electronic skin: from flexibility to a sense of touch," *Nature*, vol. 591, no. 7851, pp. 685–687, 2021.

[131] F. Liao *et al.*, "Ultrasensitive flexible temperature-mechanical dual-parameter sensor based on vanadium dioxide films," *IEEE Electron Device Letters*, vol. 38, no. 8, pp. 1128–1131, 2017.

[132] Y. Long *et al.*, "Pomegranate-inspired biomimetic pressure sensor arrays with a wide range and high linear sensitivity for human–machine interaction," *IEEE Transactions on Electron Devices*, vol. 69, no. 3, pp. 1353–1358, 2022.

[133] B. Sindhu, A. Kothuru, P. Sahatiya, S. Goel, and S. Nandi, "Laser-induced graphene printed wearable flexible antenna-based strain sensor for wireless human motion monitoring," *IEEE Transactions on Electron Devices*, vol. 68, no. 7, pp. 3189–3194, 2021.

[134] Z. Ma, J. Zhang, J. Li, Y. Shi, and L. Pan, "Frequency-enabled decouplable dual-modal flexible pressure and temperature sensor," *IEEE Transactions on Electron Devices*, vol. 41, no. 10, pp. 1568–1571, 2020.

[135] C. Yang, A. Abodurexiti, and X. Maimaitiyiming, "Flexible humidity and pressure sensors realized by molding and inkjet printing processes with sandwich structure," *Macromolecular Materials and Engineering*, vol. 305, no. 8, p. 2000287, 2020.

[136] S. Mahadeva, S. Yun, and J. Kim, "Flexible humidity and temperature sensor based on cellulose–polypyrrole nanocomposite," *Sensors and Actuators A: Physical*, vol. 165, no. 2, pp. 194–199, 2011.

[137] G. Li, Z. Tian, G. Gao, L. Zhang, M. Fu, and Y. Chen, "A shoelace antenna for the application of collision avoidance for the blind person," *IEEE Transactions on Antennas and Propagation*, vol. 65, no. 9, pp. 4941–4946, 2017.

[138] D. Anaya, K. Zhan, L. Tao, C. Lee, M. Yuce, and T. Alan, "Contactless tracking of humans using non-contact triboelectric sensing technology: Enabling new assistive applications for the elderly and the visually impaired," *Nano Energy*, vol. 90, p. 106486, 2021.

[139] P. Chanana, R. Paul, M. Balakrishnan, and P. V. M. Rao, "Assistive technology solutions for aiding travel of pedestrians with visual impairment," *Journal of rehabilitation and assistive technologies engineering*, vol. 4, p. 2055668317725993, 2017.

[140] Q. Hua *et al.*, "Skin-inspired highly stretchable and conformable matrix networks for multifunctional sensing," *Nature Communications*, vol. 68, no. 7, pp. 3189–3194, 2021.

[141] S. Ruth, V. Feig, M. Kim, Y. Khan, J. Phong, and Z. Bao, "Flexible fringe effect capacitive sensors with simultaneous high-performance contact and non-contact sensing capabilities," *Small Structures*, vol. 2, no. 2, p. 2000079, 2020.

[142] J. Qin *et al.*, "Flexible and stretchable capacitive sensors with different microstructures," *Advanced Materials*, vol. 33, no. 34, p. 2008267, 2018.

[143] S. C. Mukhopadhyay, "Wearable sensors for human activity monitoring: A review," *IEEE Sensors Journal*, vol. 15, no. 3, pp. 1321–1330, Mar. 2015.

[144] X. Wang, "Piezoelectric nanogenerators—harvesting ambient mechanical energy at the nanometer scale," *Nano Energy*, vol. 1, no. 1, pp. 13–24, Jan. 2012.

[145] A. Ghadami, H. R. Mirdamadi, and H. Khanbareh, "Dynamic modeling and analysis of flexible micro-porous piezoelectric sensors applicable in soft robotics," *Frontiers in Electronic Materials*, vol. 2, Nov. 2022.

[146] M. Zhu, S. Siang Chng, W. Cai, C. Liu, and Z. Du, "Piezoelectric polymer nanofibers for pressure sensors and their applications in human activity monitoring," Jun. 2020.

[147] S. Masihi, M. Panahi, D. Maddipatla, A. J. Hanson, A. K. Bose, S. Hajian, V. Palaniappan, B. B. Narakathu, B. J. Bazuin, and M. Z. Atashbar, "Highly sensitive porous pdms-based capacitive pressure sensors fabricated on fabric platform for wearable applications," *ACS Sensors*, vol. 6, no. 3, pp. 938–949, Mar. 2021.

[148] S. Peng, S. Chen, Y. Huang, S. Pei, and X. Guo, "High sensitivity capacitive pressure sensor with bi-layer porous structure elastomeric dielectric formed by a facile solution based process," *IEEE Sensors Letters*, vol. 3, no. 2, pp. 1–4, Feb. 2019.

[149] Y. Tian, D.-Y. Wang, Y.-T. Li, H. Tian, Y. Yang, and T.-L. Ren, "Highly sensitive, wide-range, and flexible pressure sensor based on honeycomb-like graphene network," *IEEE Transactions on Electron Devices*, vol. 67, no. 5, pp. 2153–2156, May 2020.

[150] N. T. Beigh and D. Mallick, "Low-cost, high-performance piezoelectric nanocomposite for mechanical energy harvesting," *IEEE Sensors Journal*, vol. 21, no. 19, pp. 21 268–21 276, Oct. 2021.

[151] B. Krishna, A. Chaturvedi, N. Mishra, and K. Das, "Nanomechanical characterization of su8/zno nanocomposite films for applications in energy-harvesting microsystems," *Journal of Micromechanics and Microengineering*, vol. 28, no. 11, p. 115013, Oct. 2018.

[152] Z. Li, T. J. A. Slater, X. Ma, Y. Yu, R. J. Young, and T. L. Burnett, "The taxonomy of graphite nanoplatelets and the influence of nanocomposite processing," *Carbon*, vol. 142, pp. 99–106, Feb. 2019.

[153] J. Yu, X. Hou, M. Cui, S. Zhang, J. He, W. Geng, J. Mu, and X. Chou, "Highly skin-conformal wearable tactile sensor based on piezoelectric-enhanced triboelectric nanogenerator," *Nano Energy*, vol. 64, p. 103923, Oct. 2019.

[154] Y. Khan, A. E. Ostfeld, C. M. Lochner, A. Pierre, and A. C. Arias, "Monitoring of vital signs with flexible and wearable medical devices," *Advanced Materials*, vol. 28, no. 22, pp. 4373–4395, 2016.

[155] S. Maksimovic, M. Nakatani, Y. Baba, A. M. Nelson, K. L. Marshall, S. A. Wellnitz, P. Firozi, S.-H. Woo, S. Ranade, A. Patapoutian, and E. A. Lumpkin, "Epidermal merkel cells are mechanosensory cells that tune mammalian touch receptors," *Nature*, vol. 509, no. 7502, pp. 617–621, May 2014.

[156] G. Li, S. Liu, Q. Mao, and R. Zhu, "Multifunctional electronic skins enable robots to safely and dexterously interact with human," *Advanced Science*, vol. 9, no. 11, p. 2104969, 2022.

[157] P. Fang, X. Ma, X. Li, X. Qiu, R. Gerhard, X. Zhang, and G. Li, "Fabrication, structure characterization, and performance testing of piezoelectret-film sensors for recording body motion," *IEEE Sensors Journal*, vol. 18, no. 1, pp. 401–412, Jan. 2018.

[158] S. Sharma, A. Chhetry, D. Kim, and J. Y. Park, "Polyaniline-nanospikes modified hybrid nanofibrous membrane based flexible piezoresistive sensor for physiological signal monitoring," in *2022 IEEE 35th International Conference on Micro Electro Mechanical Systems Conference (MEMS)*, Jan. 2022, pp. 9–12.

[159] Y. Pang, X. Xu, S. Chen, Y. Fang, X. Shi, Y. Deng, Z.-L. Wang, and C. Cao, "Skin-inspired textile-based tactile sensors enable multifunctional sensing of wearables and soft robots," *Nano Energy*, vol. 96, p. 107137, Jun. 2022.

[160] S. R. A. Ruth and Z. Bao, "Designing tunable capacitive pressure sensors based on material properties and microstructure geometry," *ACS Applied Materials & Interfaces*, vol. 12, no. 52, pp. 58 301–58 316, Dec. 2020.

[161] G. Liu, X. Chen, X. Li, C. Wang, H. Tian, X. Chen, B. Nie, and J. Shao, "Flexible, equipment-wearable piezoelectric sensor with piezoelectricity calibration enabled by in-situ temperature self-sensing," *IEEE Transactions on Industrial Electronics*, vol. 69, no. 6, pp. 6381–6390, Jun. 2022.

[162] S. R. A. Ruth, L. Beker, H. Tran, V. R. Feig, N. Matsuhisa, and Z. Bao, "Rational design of capacitive pressure sensors based on pyramidal microstructures for specialized monitoring of biosignals," *Advanced Functional Materials*, vol. 30, no. 29, p. 1903100, 2020.

[163] S. Chun, J.-S. Kim, Y. Yoo, Y. Choi, S. J. Jung, D. Jang, G. Lee, K.-I. Song, K. S. Nam, I. Youn *et al.*, "An artificial neural tactile sensing system," *Nature Electronics*, vol. 4, no. 6, pp. 429–438, 2021.

[164] D. Gromnicka and B. Wałecki, "Usefulness of the analysis of the average ridge width of fingerprints in archaeological research," *Anthropological Review*, vol. 85, no. 1, pp. 31–49, 2022.

[165] E. Sotgiu, D. E. Aguiam, C. Calaza, J. Rodrigues, J. Fernandes, B. Pires, E. E. Moreira, F. Alves, H. Fonseca, R. Dias *et al.*, "Surface texture detection with a new sub-mm resolution flexible tactile capacitive sensor array for multimodal artificial finger," *Journal of Microelectromechanical Systems*, vol. 29, no. 5, pp. 629–636, 2020.

[166] J.-S. Yang, M.-K. Chung, J.-Y. Yoo, M.-U. Kim, B.-J. Kim, M.-S. Jo, S.-H. Kim, and J.-B. Yoon, "Interference-free nanogap pressure sensor array with high spatial resolution for wireless human-machine interfaces applications," *Nature Communications*, vol. 16, no. 1, p. 2024, 2025.

[167] X. Chen, Y. Luo, Y. Chen, S. Li, S. Deng, B. Wang, Q. Zhang, X. Li, X. Li, C. Wang *et al.*, "Biomimetic contact behavior inspired tactile sensing array with programmable microdomes pattern by scalable and consistent fabrication," *Advanced Science*, vol. 11, no. 43, p. 2408082, 2024.

[168] K. Park, S. Kim, H. Lee, I. Park, and J. Kim, "Low-hysteresis and low-interference soft tactile sensor using a conductive coated porous elastomer and a structure for interference reduction," *Sensors and Actuators A: Physical*, vol. 295, pp. 541–550, 2019.

[169] L. Nela, J. Tang, Q. Cao, G. Tulevski, and S.-J. Han, "Large-area high-performance flexible pressure sensor with carbon nanotube active matrix for electronic skin," *Nano letters*, vol. 18, no. 3, pp. 2054–2059, 2018.

[170] V. Lumelsky, M. Shur, and S. Wagner, "Sensitive skin," *IEEE Sensors Journal*, vol. 1, no. 1, pp. 41–51, 2001.

[171] W. Lin, B. Wang, G. Peng, Y. Shan, H. Hu, and Z. Yang, "Skin-inspired piezoelectric tactile sensor array with crosstalk-free row+ column electrodes for spatiotemporally distinguishing diverse stimuli," *Advanced Science*, vol. 8, no. 3, p. 2002817, 2021.

[172] K. Bae, M. Kim, S. Sim, Y. Kang, and J. Kim, "Dome-structure array from pre-strained extendable mesh for tactile sensing without crosstalk and lateral strain interference," *Small Methods*, p. 2401730, 2025.

[173] G. Liang, Y. Wang, D. Mei, K. Xi, and Z. Chen, "Flexible capacitive tactile sensor array with truncated pyramids as dielectric layer for three-axis force measurement," *Journal of Microelectromechanical systems*, vol. 24, no. 5, pp. 1510–1519, 2015.

[174] J. Weichart, C. Roman, and C. Hierold, "Tactile sensing with scalable capacitive sensor arrays on flexible substrates," *Journal of Microelectromechanical Systems*, vol. 30, no. 6, pp. 915–929, 2021.

[175] Y. Zang, F. Zhang, D. Huang, X. Gao, C.-a. Di, and D. Zhu, "Flexible suspended gate organic thin-film transistors for ultra-sensitive pressure detection," *Nature communications*, vol. 6, no. 1, p. 6269, 2015.

[176] H.-J. Kwon, J.-H. Kim, and W.-C. Choi, "Development of a flexible three-axial tactile sensor array for a robotic finger," *Microsystem technologies*, vol. 17, no. 12, pp. 1721–1726, 2011.

[177] S. Chun, W. Son, H. Kim, S. K. Lim, C. Pang, and C. Choi, "Self-powered pressure-and vibration-sensitive tactile sensors for learning technique-based neural finger skin," *Nano letters*, vol. 19, no. 5, pp. 3305–3312, 2019.

[178] T. Someya, T. Sekitani, S. Iba, Y. Kato, H. Kawaguchi, and T. Sakurai, "A large-area, flexible pressure sensor matrix with organic field-effect transistors for artificial skin applications," *Proceedings of the National Academy of Sciences*, vol. 101, no. 27, pp. 9966–9970, 2004.

[179] Z. Zhou, R. Wang, Z. Yang, X.-F. Shen, Y. Xiong, and Y. Feng, "The semi-analytical model of electric field and capacitance in a multilayer-structured interdigital electrode capacitor," *Applied Mathematical Modelling*, vol. 136, p. 115632, 2024.

[180] C. Ge, Z. Wang, Z. Liu, T. Wu, S. Wang, X. Ren, D. Chen, J. Zhao, P. Hu, and J. Zhang, "A capacitive and piezoresistive hybrid sensor for long-distance proximity and wide-range force detection in human–robot collaboration," *Advanced Intelligent Systems*, vol. 4, no. 3, p. 2100213, 2022.

List of Publications

Journal

Out of Thesis Work

1. **M. Yousuf**, P. Singh, M.M. Hussain. Pressure-Induced Mode Transition and Physical Model for a Suspended Hybrid Tactile Sensor. *Applied Physics Letters* (Under Review).

2. **M. Yousuf**, P. Singh, M.M. Hussain. Sub-mm Resolution, High Density (4096 sensors) Fully Integrated Flexible Capacitive Tactile Sensor Array for Next-Generation Human-Machine Interfaces. *ACS Sensors* (Under Review).

3. **M. Yousuf**, P. Singh, M.M. Hussain. A Microstructure-Engineered PEDOT:PSS-LIG Tactile Skin for Biometric User Authentication. *Small* (To be Submitted).

4. **M. Yousuf**, P. Singh, M.M. Hussain. Dual-Isolation Hybrid Tactile Array with Fully Parallel Readout and Sub-0.3% Crosstalk Mode Transition and Physical Model for a Suspended Hybrid Tactile Sensor. *IEEE Transactions on Electron Devices* (Accepted). 10.1109/TED.2026.3671232.

5. **M. Yousuf**, J.C. Rochet, P. Singh, M.M. Hussain. Advancing Brain Organoid Electrophysiology: Minimally Invasive Technologies for Comprehensive Characterization. *Advanced Material Technologies*, vol. 10, no. 7, p. 2401585, 2025. 10.1002/admt.202401585.

6. **M. Yousuf**, N.T. Beigh, D.S. Arya, M. Garg, D. Mallick, P. Singh. A Sensitive and Flexible Poroelastic Barium Titanate Matrix for Pressure Sensing Applications. *IEEE Sensor Letters*, vol. 7, no. 2, pp. 1–4, 2023. 10.1109/LSENS.2023.3240424.

7. **M. Yousuf**, M. Garg, D.S. Arya, P. Singh. Skin-Inspired Bimodal Magneto-Dielectric-Based Flexible and Sensitive Capacitive Sensor for Limb Motion Tracking. *IEEE Transactions Electron Devices*, vol. 70, no. 3, pp. 1338–1343, 2023. 10.1109/TED.2022.3232585.

8. **M. Yousuf**, D.S. Arya, M. Garg, D. Varshney, P. Singh. Asymmetric Capacitive Pixel Array (E-CaP) for Mapping of Epidermal Vectored Movement. *IEEE Journal of Flexible Electronics*, vol. 1, no. 2, pp. 134–140, 2022. 10.1109/JFLEX.2022.3170528.

<u>With Peer Researchers</u>

1. J. Shen, **M. Yousuf**, D. Belkadi, M.S. Kim, M.M. Hussain. Autonomous Reconfigurable Multidimensional System for Movement and Collaboration. *Advanced Robotics Research* (Under Review).

2. Y. Adebakin, **M. Yousuf**, M.M. Hussain. Transforming Public Health: Wearable Temperature Sensors on Robotic Platforms for Contactless Data Collection. *Advanced Intelligent Systems* (Under Review).

3. K. Joshi, M. Garg, **M. Yousuf**, S. Kumar, P. Singh. Capacitorless MEMS-Based Temporary Memory (CMTM) with Extended Refresh Interval. *IEEE Transactions Electron Devices*, vol. 71, no. 11, pp. 6659–6664, 2024. 10.1109/TED.2024.3453782.

4. M. Garg, D.S. Arya, S. Kumar, **M. Yousuf**, Y. Chiu, P. Singh. Electrostatically Actuated All-Metal MEMS Pirani Gauge with Tunable Dynamic Range. *Journal of Micromechanics and Microengineering*, vol. 34, no. 2, p. 025003, 2024. 10.1088/1361-6439/ad1b1a.

5. M. Srivastava, S. Kumar, **M. Yousuf**, B. Kumar, P. Singh, W.S. Ali. Reaching High Piezoelectric Performance with Rotating Directional-Field-Aligned PVDF–MoS_2 Piezo-Polymer Applicable for Large-Area Flexible Electronics. *Macromolecular Rapid Communications*, vol. 44, no. 24, p. 2300315, 2023. 10.1002/marc.202300315.

6. M. Garg, D.S. Arya, S. Kumar, **M. Yousuf**, Y. Chiu, P. Singh. Stress Engineered SU-8 Dielectric-Microbridge Based Polymer MEMS Pirani Gauge for Broad Range Hermetic Characterization. *Journal of Micromechanics and Microengineering*, vol. 32, no. 7, p. 075004, 2022. 10.1088/1361-6439/ac6aa4.

Conferences

Out of Thesis Work

1. **M. Yousuf**, S. Ali, K. Joshi, P. Singh. Eco-Friendly Fabrication Process of Flexible Piezoelectric Pressure Sensors: A Path to Sustainable Electronics. *Proc. 38th IEEE Int. Conf. Micro Electro Mechanical Systems (MEMS)*, pp. 395–398, 2025. 10.1109/MEMS61431.2025.10917328.

2. **M. Yousuf**, P. Singh. A Fully Integrated, Flexible and Tunable Capacitive Strain Sensor Based on Magneto-Dielectric for Human Motion Monitoring. *Proc. 38th IEEE Int. Conf. Micro Electro Mechanical Systems (MEMS)*, pp. 367–370, 2025. 10.1109/MEMS61431.2025.10917399.

3. **M. Yousuf**, S. Kumar, D.S. Arya, M. Garg, K. Joshi, P. Singh. Multi-Mode E-Skin Integrating Capacitive-Piezoelectric Sensors for Static-Dynamic Mechanoresponse with Wide Sensing Range. *Proc. 36th IEEE Int. Conf. Micro Electro Mechanical Systems (MEMS)*, pp. 347–350, 2023. 10.1109/MEMS49605.2023.10052349.

4. **M. Yousuf**, N.T. Beigh, P. Singh, D. Mallick. µ-Patterned Flexible MEMS-Compatible Piezoelectric Nanocomposite-Based Pressure Sensor. *IWPSD*, 2021.

With Peer Researchers

1. K. Joshi, M. Garg, **M. Yousuf**, P. Singh. Reducing Dynamic Memory Refresh Overhead Via Read-Less Refresh Operation Using MEMS-Based Memory Cell. *Proc. 38th IEEE Int. Conf. Micro Electro Mechanical Systems (MEMS)*, pp. 554–557, 2025. 10.1109/MEMS61431.2025.10918225.

2. S. Ali, **M. Yousuf**, P. Singh. A Finite Element Analysis of MEMS-Based Magnetoelectric Micro Antenna for On-Chip RF Energy Harvesting. *Proc. 2024 IEEE Region 10 Symp. (TENSYMP)*, pp. 1–4, 2024. 10.1109/TENSYMP61132.2024.10751820.

3. S. Ali, **M. Yousuf**, P. Singh. A Finite Element Analysis of MEMS-Based Magnetoelectric Micro Antenna for On-Chip RF Energy Harvesting. *Proc.*

2023 IEEE Microwaves, Antennas, and Propagation Conf. (MAPCON), pp. 1–5, 2023. 10.1109/MAPCON58678.2023.10464178.

4. F.T. Beigh, N.T. Beigh, **M. Yousuf**, D. Mallick, P. Singh. Localized Biomechanical Strain Sensing with Graphene/SU-8 Nanocomposite-Based Highly Flexible Piezoresistive Sensor. *Proc. 22nd Int. Conf. Solid-State Sensors, Actuators and Microsystems (Transducers)*, pp. 784–787, 2023.

5. K. Joshi, R. Aryan, **M. Yousuf**, M. Garg, P. Singh. Simulation Study on Adhesion Force (Fadh) for MEMS-Based Non-Volatile Memory (NVM) Applications. *Proc. 2023 Int. Conf. Computer, Electronics, and Electrical Engineering and their Applications (IC2E3)*, pp. 1–4, 2023. 10.1109/IC2E357697.2023.10262629.

6. K. Joshi, M. Garg, D.S. Arya, S. Kumar, **M. Yousuf**, P. Singh. Energy-Efficient Adhesion Controlled MEMS Volatile Memory (MVM). *Proc. IEEE Sensors*, pp. 1–4, 2022. 10.1109/SENSORS52175.2022.9967289.

7. M. Garg, D.S. Arya, S. Kumar, K. Joshi, **M. Yousuf**, P. Singh. Modelling the Anchor Effect for Estimating Performance Metrics of a MEMS Pirani Gauge. *Proc. IEEE Sensors*, pp. 1–4, 2022. 10.1109/SENSORS52175.2022.9967077.

8. M. Garg, D.S. Arya, S. Kumar, K. Joshi, **M. Yousuf**, A. Goswami, P. Singh. Ultrasensitive Reduced Vanadium Dioxide-Based MEMS Pirani Gauge with Extended Dynamic Range. *IWPSD*, 2022.

9. M. Garg, K. Joshi, D.S. Arya, **M. Yousuf**, A. Goswami, P. Singh, D. Mallick. Ultrasensitive Reduced Vanadium Dioxide-Based MEMS Pirani Gauge with Extended Dynamic Range. *Proc. Int. Workshop Phys. Semicond. Devices (IWPSD)*, pp. 311–318, 2021. 10.1007/978-981-97-1571-$8_3$7.

Curriculum Vitae

Personal Information

- **Name:** Mujeeb Yousuf
- **Email:** mujeeb.yousuf@care.iitd.ac.in
- **Phone:** +91-7006341905
- **Address:** IIT Delhi, Hauz Khas, New Delhi - 110016, India

Education

- **Ph.D., Electrical Engineering**, IIT Delhi (Jul 2019-2026)
  Thesis Submitted. Supervisor: Prof. Pushpapraj Singh.
- **M.Tech., Control & Instrumentation**, Jamia Millia Islamia (2017-2019)
  Grade: 9.27/10
- **B.Tech., Electrical Engineering**, Islamic University of Science & Technology (2012-2016)
  Grade: 7.6/10

PhD Thesis

Title: Design and Development of Flexible Electromechanical Sensors for Human Motion Monitoring and Human–Machine Interfaces.

Supervisor: Prof. Pushpapraj Singh, IIT Delhi

This research focuses on the design and development of flexible electromechanical sensing systems for wearable electronics and human-machine interfaces. The

work integrates soft functional materials, microfabrication techniques, and embedded electronics to realize scalable and high-density tactile sensing platforms. The developed sensors demonstrate multimodal sensing capabilities, including pressure, strain, and proximity detection, and are validated through applications in human motion monitoring, wearable HMI systems, and high-resolution tactile sensing.

Research Experience

- **Overseas Visiting Doctoral Fellow**, Purdue University (Aug 2023-Jan 2025)
- **Senior Research Scholar**, IIT Delhi

Skills

- **Programming:** Python, MATLAB, Embedded C
- **Research:** Flexible electronics, MEMS fabrication, sensor modeling, COMSOL simulation
- **Tools:** KiCad PCB design, COMSOL Multiphysics, MSP430

Scholastic Achievements

- SERB Overseas Visiting Doctoral Fellowship
- Research Excellence Travel Award (RETA)
- UGC-NET Qualified (2018, 2019)
- GATE Qualified (2017, 2018)
- Second Rank, M.Tech (Control & Instrumentation)

Teaching Assistantship

- Teaching Assistant, Fabrication and IC Design Lab, CARE, IIT Delhi
- Training support for Mask Aligner systems at NRF, IIT Delhi

Additional Information

- **Languages:** English, Urdu, Hindi, Kashmiri
- **Interests:** Cricket, Badminton, Gardening